

Reliable Explanations or Random Noise? A Reliability Metric for XAI

Poushali Sengupta¹ Sabita Maharjan¹ Frank Eliassen¹ Shashi Raj Pandey² Yan Zhang¹

Abstract

In recent years, explaining decisions made by complex machine learning models has become essential in high-stakes domains such as energy systems, healthcare, finance, and autonomous systems. However, the reliability of these explanations, namely, whether they remain stable and consistent under realistic, non-adversarial changes, remains largely unmeasured. Widely used methods such as SHAP and Integrated Gradients (IG) are well-motivated by axiomatic notions of attribution, yet their explanations can vary substantially even under system-level conditions, including small input perturbations, correlated representations, and minor model updates. Such variability undermines explanation reliability, as reliable explanations should remain consistent across equivalent input representations and small, performance-preserving model changes. We introduce the Explanation Reliability Index (ERI), a family of metrics that quantifies explanation stability under four reliability axioms: robustness to small input perturbations, consistency under feature redundancy, smoothness across model evolution, and resilience to mild distributional shifts. For each axiom, we derive formal guarantees, including Lipschitz-type bounds and temporal stability results. We further propose ERI-T, a dedicated measure of temporal reliability for sequential models, and introduce ERI-Bench, a benchmark designed to systematically stress-test explanation reliability across synthetic and real-world datasets. Experimental results reveal widespread reliability failures in popular explanation methods, showing that explanations can be unstable under realistic deployment conditions. By exposing and quantifying these instabilities, ERI enables principled assessment of explanation reliability and supports more trustworthy explainable AI (XAI) systems.

1. Introduction

As transparency, accountability, and safety have become critical requirements, XAI has emerged as an essential component for deploying complex machine learning models. Techniques such as SHAP (Lundberg & Lee, 2017), IG (Sundararajan et al., 2017), DeepLIFT (Shrikumar et al., 2017), SAGE (Covert et al., 2020), and perturbation-based importance scores (Ivanovs et al., 2021) are widely used to interpret predictions in healthcare, finance, climate modeling, and scientific discovery. Despite their broad adoption, a fundamental question remains unanswered: *How reliable are these explanations?* Most existing evaluation tools focus on predictive accuracy or agreement with synthetic ground truth, assessing how well explanations align with a model’s output behavior. However, strong predictive performance alone does not guarantee that explanations are reliable or stable under realistic variations. An explanation may appear reasonable on average yet remain highly unstable under small, non-adversarial variations such as small input noise, correlated features, minor model checkpoint changes, or mild distributional shifts. Prior studies have documented these failures extensively (Adebayo et al., 2018): small perturbations can alter attribution rankings, redundant features can distort Shapley values, and minor training variations can cause large oscillations in explanations. Intuitively, redundant features should improve explanation robustness by preserving the same semantic information, for example, representing temperature in both Celsius and Fahrenheit should not change which factor is deemed important, yet many existing explanation methods treat such features independently and arbitrarily redistribute importance, leading to increased instability (Kumar et al., 2020; Covert & Lee, 2021a). Such instability undermines trust and limits the practical usefulness of explainable machine learning systems. Moreover, to the best of our knowledge, there exists no metric for assessing explanation reliability across different small, non-adversarial variations.

Real-world data, such as meteorological measurements, medical signals, or sensor readings, inevitably contain noise and correlations (Ovadia et al., 2019). A reliable explanation should satisfy all four reliability axioms simultaneously, each reflecting a practical deployment challenge. **Stability under small, non-adversarial perturbations (A1)** requires explanations to remain unchanged under small,

¹Department of Informatics, University of Oslo, Oslo, Norway

²Department of Electronic Systems, The Technical Faculty of IT and Design, Aalborg University, Denmark. Correspondence to: Poushali Sengupta <poushals@ifi.uio.no>.

non-adversarial input variations (Adebayo et al., 2018). **Redundancy-collapse consistency (A2)** ensures that semantically equivalent or highly correlated features (e.g., height in inches versus centimeters) receive consistent attribution (Aas et al., 2021). **Model-evolution consistency (A3)** requires explanations to remain stable across model retraining or updates when predictive behavior changes a little (Yeh et al., 2019; Hooker et al., 2020). **Distributional and temporal robustness (A4)** demands that explanations remain reliable under natural data shifts over time or across sources, which are common in vision, language, and time-series applications (Ovadia et al., 2019; Arras et al., 2021). Violations of any of these properties can render explanations unstable, misleading, or difficult to compare, even when model predictions remain unchanged. While existing explanation methods and evaluation protocols may satisfy one or two of these properties in isolation, the literature lacks a quantitative metric that captures these properties within a single, aggregated reliability assessment (Adebayo et al., 2018; Yeh et al., 2019). Most prior work relies on proxy criteria such as sparsity or agreement with human intuition, providing no principled way to determine whether explanations are reliable, comparable, and suitable for real-world deployment under small, non-adversarial variations (Doshi-Velez & Kim, 2017). As a result, explanation reliability is often evaluated qualitatively or through ad hoc stress tests, and explanations that appear reliable in one setting may fail in another (Hooker et al., 2020). We argue that reliability is a core requirement of XAI: beyond producing plausible explanations, XAI systems must provide information that can be consistently relied upon over time (Lipton, 2018). For example, a weather forecasting system becomes less dependable if small, routine variations in input data lead to substantially different explanations, even when predictions remain similar (Ovadia et al., 2019).

To address this gap, we introduce the *Explanation Reliability Index (ERI) family*, a set of model-agnostic, property-wise metrics that quantify how consistently explanations reflect model behavior across multiple reliability axioms, with an optional aggregation yielding a single summary score. ERI is supported by strong theoretical foundations, including bounds on explanation variation, guarantees for redundancy collapse, and a novel temporal reliability measure for sequential models such as LSTMs, GRUs, Transformers, and temporal CNNs (Arras et al., 2021). This temporal extension evaluates how smoothly explanations evolve over time, independently of prediction smoothness, establishing ERI as a principled and standardized reliability signal. In addition, we present *ERI-Bench*, the first benchmark explicitly designed to stress-test explanation reliability across vision, time-series, and tabular data. ERI-Bench reveals substantial reliability failures in widely used explainers across EEG microstates, UCI HAR, Norwegian load forecasting, and

CIFAR-10, showing that gradient-based and Shapley-based methods often suffer from instability (Lundberg & Lee, 2017; Sundararajan et al., 2017), while dependence-aware methods, such as MCIR (see Appendix A for details), Mutual Information, and HSIC, achieve consistently higher reliability. Together, ERI and ERI-Bench establish reliability as a fundamental dimension of explanation quality and provide a principled foundation for the systematic evaluation and improvement of XAI methods¹. This work contributes to the field of XAI in three primary ways:

1. **Actionable Reliability Framework.** We introduce the ERI family, an axiomatic set of reliability measures that quantify explanation stability under realistic variations and enable practical uses such as reliability-aware checkpoint selection without degrading predictive performance.
2. **Temporal Reliability (ERI-T).** We propose ERI-T, the first quantitative metric for measuring how consistently explanations evolve over time in sequential models such as LSTMs, GRUs, Transformers, and temporal CNNs.
3. **ERI-Bench.** We release ERI-Bench, a benchmark designed to systematically evaluate explanation reliability under perturbations, feature correlations, model updates, and temporal variation, exposing widespread reliability failures in popular XAI methods.

2. Related Work

A wide range of explanation techniques assign importance scores to input features, including SHAP (Lundberg & Lee, 2017), IG (Sundararajan et al., 2017), DeepLIFT (Shrikumar et al., 2017), SmoothGrad (Smilkov et al., 2017), LIME (Ribeiro et al., 2016), and PFI (Breiman, 2001). Although these methods differ in how they approximate contributions, none provide a formal assessment of *reliability* under all four axiomatic properties stated before. Global importance measures such as SAGE (Covert et al., 2020), global SHAP, and gradient-based saliency maps provide distribution-level insights, while dependence measures such as Mutual Information (MI), Conditional Mutual Information (CMI), and the Hilbert–Schmidt Independence Criterion (HSIC) quantify statistical association between inputs and model outputs. MI measures the overall dependence between variables, CMI captures dependence conditional on other features, and HSIC detects nonlinear dependence using kernel-based statistics (Cover & Thomas, 1991; Fukumizu et al., 2007; Gretton et al., 2005). Related measures such as CKA assess similarity between learned representations (Kornblith et al., 2019). However, these do not evaluate whether explanations remain *stable* under small,

¹Formal definitions, theoretical results, and extended experiments are provided in the appendix (Appendices A–Z). Code, datasets, and the ERI-Bench framework are available at <https://anonymous.4open.science/r/ERI-C316/README.md>.

non-adversarial variations. A growing body of work studies instability in explanations. Perturbation analyses show that many explainers are highly sensitive to input noise, with small changes substantially altering attribution rankings (Ghorbani et al., 2019; Kindermans et al., 2019). Redundancy and feature correlation further degrade reliability: SHAP is known to inflate attributions under correlated or duplicated features (Kumar et al., 2020; Covert & Lee, 2021b), while gradient-based explainer outputs often change unpredictably. Existing fixes rely on heuristics rather than principled models of redundancy. Temporal robustness, namely, the requirement that explanations evolve smoothly over time when inputs and model behavior change gradually, has received limited attention. Most existing studies focus on prediction smoothness rather than explanation smoothness, and current saliency methods for sequential models (Arras et al., 2021; Singh & Anand, 2020) provide primarily qualitative insight without offering a quantitative measure of temporal reliability. In time-dependent systems such as forecasting, monitoring, or control, unstable explanations across consecutive time steps can obscure evolving system dynamics and undermine the practical usability of XAI, making temporal robustness a critical reliability requirement. Robustness under model changes and fine-tuning (Yeh et al., 2019), as well as structural modifications such as pruning and compression (Hooker et al., 2020), has been studied, but existing diagnostics remain fragmented and task-specific.

LIME is sensitive to sampling noise and violates perturbation stability (A1). SHAP satisfies efficiency and symmetry but fails under feature redundancy and distributional shifts (A2, A4). Gradient-based methods (e.g., IG, Grad-CAM++) show partial perturbation stability (A1) yet break under redundancy and temporal variation (A2, A4). Global dependence-based methods such as SAGE partially address feature correlation and redundancy (A2) but do not ensure consistency across model evolution (A3). We additionally report information-theoretic dependence measures, including MI and HSIC, as non-explanatory reference baselines that capture global statistical dependence but do not produce local attributions or assess temporal reliability. ERI addresses this gap through an aggregated, axiomatic framework for evaluating explanation reliability. ERI assigns a quantitative reliability score by evaluating attribution behavior against four axioms (A1–A4), with each component (ERI-S, ERI-R, ERI-M, ERI-D, and ERI-T) targeting a specific variation axis while remaining comparable within a single framework. Aggregating these components into a scalar score makes reliability explicit and directly comparable. ERI thus acts as a *verification layer* over existing explainers, complemented by ERI-Bench, the first benchmark designed to stress-test explanation reliability across synthetic, temporal, and real-world settings. To this end, this paper contributes a realistic and systematic approach to

assessing the reliability of explanations. ERI is not intended to replace faithfulness, correctness, or causal analysis, but to complement them by formalizing a general reliability functional over model-derived attribution signals, applicable beyond feature explanations to attention, saliency, influence functions, and representation-level analyses.

3. Axioms of Reliable Explanations

To reason about the reliability of explanation, we formalize four axioms that specify how a valid explanation method should behave under small and non-adversarial variations. Throughout this section, let $x \in \mathbb{R}^d$ denote an input, $E(x) \in \mathbb{R}^d$ denote its explanation vector (e.g., attribution scores for each feature), and $d(\cdot, \cdot)$ ² be a non-negative dissimilarity between explanations. We use δ to denote a perturbation applied to x , α to represent a redundancy parameter, and t to index model checkpoints during training. Throughout this work, an explanation $E(x) \in \mathbb{R}^d$ is defined as the vector of feature-level attribution scores produced by an explainer E for an input $x \in \mathbb{R}^d$. Each component $E_i(x)$ represents the *contribution* of the input feature x_i to the model’s prediction at x .³ This definition is intentionally general and encompasses a wide range of attribution methods, including gradient-based methods (Gradient×Input, IG), perturbation-based methods (Occlusion, SmoothGrad), and game-theoretic methods (SHAP).

Axiom 1 (Stability Under Small Perturbations). Let $x \in \mathbb{R}^d$ and let $\delta \in \mathbb{R}^d$ satisfy $\|\delta\| \leq \epsilon$. Assume that the explanation map $E : \mathbb{R}^d \rightarrow \mathbb{R}^d$ is locally Lipschitz at x , i.e., there exist $r > 0$ and a constant $C_E(x) > 0$ such that for all $u, v \in B(x, r)$, $d(E(u), E(v)) \leq C_E(x) \|u - v\|$. Then, for all perturbations δ with $\|\delta\| \leq \min\{\epsilon, r\}$, $d(E(x), E(x + \delta)) \leq C_E(x) \|\delta\| \leq C_E(x) \epsilon$.

Axiom 2 (Redundancy-Collapse Consistency). Let $x = [x_1, x_2, \dots, x_d] \in \mathbb{R}^d$ denote an input and $E(x) = [E_1(x), E_2(x), \dots, E_d(x)]$ its feature-wise explanation. Assume that feature x_j becomes asymptotically redundant with respect to feature x_i according to the redundancy model, $x_j = \alpha x_i + \sqrt{1 - \alpha^2} Z$, where Z is independent noise and $\alpha \in [0, 1)$ controls the degree of redundancy. Let’s $E^{\text{col}}(x)$ denote the explanation obtained after collapsing the redundant feature pair (i, j) into a single effective feature. Then a redundancy-consistent explanation method should satisfy, $\lim_{\alpha \rightarrow 1} d(E^{\text{col}}(x), E(x^{\text{col}})) = 0$.

Definition 1 (Collapse Operator). To operationalize Axiom 2, we define a deterministic collapse operator

²Unless stated otherwise, theoretical results assume that d is a (pseudo-)metric, i.e., it satisfies symmetry and the triangle inequality. Empirical evaluations may additionally report more general non-metric dissimilarities (e.g., cosine or rank-based distances) as complementary measures of directional or ordering changes.

³We use the term *attribution score* to denote feature-level contribution throughout this paper.

$C_{i \leftarrow j} : \mathbb{R}^d \rightarrow \mathbb{R}^{d-1}$ for a redundant feature pair (i, j) . The operator acts as (i) the feature j is removed from the input, and (ii) the feature i is compensated by absorbing the redundant component of x_j . For the synthetic redundancy model $x_j = \alpha x_i + \sqrt{1 - \alpha^2} Z$, the collapsed input is defined as, $x_i^{\text{col}} := C_{i \leftarrow j}(x)$; $x_i^{\text{col}} = x_i + \alpha x_i$.

Definition 2 (Collapsed Explanation). Let $P_{-j} : \mathbb{R}^d \rightarrow \mathbb{R}^{d-1}$ denote the projection operator that removes the j -th coordinate. The collapsed explanation is defined as,

$$E^{\text{col}}(x) := P_{-j}(E(x)). \quad (1)$$

When two features carry the same information, explanations should converge rather than redistribute importance.

Axiom 3 (Smooth Evolution). Let $\Delta(\cdot)$ denote the explanation drift induced by a small, non-adversarial transformation (e.g., input perturbation, redundancy injection, model update, temporal or distributional shift). Explanation reliability is defined as $\text{ERI}(x) = \psi(\Delta(x))$, where $\psi : \mathbb{R}_{\geq 0} \rightarrow (0, 1]$ satisfies the properties, **Strict monotonicity**: ψ is strictly decreasing in Δ . **Continuity at zero**: $\lim_{\Delta \rightarrow 0} \psi(\Delta) = 1$. **Smooth evolution**: for any sequence of small, non-adversarial transformations inducing $\Delta_n \rightarrow 0$ (e.g., $\|\theta_{k+1} - \theta_k\| \rightarrow 0$ in model evolution), the corresponding reliability scores satisfy $\text{ERI}_n = \psi(\Delta_n) \rightarrow 1$.

Axiom 4 (Distributional Robustness). Let \mathcal{P} and \mathcal{P}' be two probability distributions on \mathbb{R}^d . Let $d_{\mathcal{P}}$ be a probability metric that admits a Kantorovich–Rubinstein dual representation over Lipschitz test functions (e.g., the Wasserstein–1 distance). Assume that, $d_{\mathcal{P}}(\mathcal{P}, \mathcal{P}') \leq \epsilon$. Assume further that the explanation map $E : \mathbb{R}^d \rightarrow \mathbb{R}^d$ is L_E -Lipschitz with respect to the input norm $\|\cdot\|$ and the attribution-space dissimilarity $d(\cdot, \cdot)$, i.e., $d(E(x), E(x')) \leq L_E \|x - x'\| \quad \forall x, x' \in \mathbb{R}^d$. Then a distributionally robust explanation method satisfies⁴, $d(\mathbb{E}_{x \sim \mathcal{P}}[E(x)], \mathbb{E}_{x \sim \mathcal{P}'}[E(x)]) \leq L_E d_{\mathcal{P}}(\mathcal{P}, \mathcal{P}') \leq L_E \epsilon$.

4. The Explanation Reliability Index (ERI)

Recall that $x \in \mathbb{R}^d$ denotes an input and $E(x) \in \mathbb{R}^d$ its corresponding explanation vector, where $E_i(x)$ represents the attribution of feature x_i to the model’s prediction. We assess explanation reliability under *small, non-adversarial, non-adversarial transformations* that reflect realistic operating conditions (e.g., noise, redundancy, temporal or distributional drift), rather than worst-case perturbations. Accordingly, stability is measured in expectation over a transformation distribution, capturing typical behavior rather than adversarial robustness.

Definition 3 (Explanation Drift). Let $E : \mathcal{X} \rightarrow \mathbb{R}^d$ denote an explanation method and let \mathcal{T} be a family of small,

⁴The bound applies to probability metrics that capture smooth, gradual distributional shifts (e.g., Wasserstein-1). It does not hold in general for metrics such as total variation without extra boundedness assumptions on E .

non-adversarial transformations⁵ acting on the explanation pipeline. Let $\tau_{\omega} \sim \Omega$ denote a random transformation drawn from a distribution Ω over \mathcal{T} . The explanation drift is defined as $\Delta(x) := \mathbb{E}_{\omega \sim \Omega} [d(E(x), E(\tau_{\omega}(x)))]$, where $d : \mathbb{R}^d \times \mathbb{R}^d \rightarrow \mathbb{R}_{\geq 0}$ is a non-negative dissimilarity function.

Definition 4 (Explanation Reliability Index (ERI)⁶). The explanation reliability index is defined as a bounded, monotone transformation of the drift:

$$\text{ERI}(x) := \frac{1}{1 + \Delta(x)} \in (0, 1]. \quad (2)$$

A value of $\text{ERI}(x)$ close to 1 indicates a highly stable explanation, whereas values near 0 reflect instability or noise-like behavior. Geometrically, $E(x)$ can be viewed as a point in attribution space, while small, non-adversarial transformations generate a cloud of transformed explanations $\{E(\tau_{\omega}(x))\}_{\omega \sim \Omega}$ around it (Figure 7). The drift $\Delta(x)$ measures the expected deviation of this cloud from $E(x)$ under typical operating variability, and ERI applies the bounded monotone map $u \mapsto (1 + u)^{-1}$ so that smaller drift corresponds to higher reliability. Different ERI variants correspond to different choices of the small, non-adversarial transformation family \mathcal{T} and sampling distribution Ω . Specifically, ERI-S uses $\tau_{\omega}(x) = x + \delta$, where δ denotes small, non-adversarial noise (e.g., bounded ℓ_p perturbations or Gaussian noise with controlled magnitude); ERI-R applies transformations τ_{ω} that inject feature redundancy or perform feature collapse under an α -redundancy model; ERI-M uses transformations $\theta \mapsto \theta'$, corresponding to successive model checkpoints or re-training seeds, and compares explanations $E_{\theta}(x)$ and $E_{\theta'}(x)$; ERI-D evaluates small, non-adversarial shifts in the data-generating process by comparing explanations under \mathcal{P} and \mathcal{P}' ; and ERI-T induces temporal shifts along a sequence, comparing explanations across adjacent time steps. The proposed evaluation framework consists of the *ERI family*, where each variant scores reliability with respect to a specific stability property. These components can optionally be aggregated via a fixed aggregation function⁷. We evaluate explanation reliability using ERI-BENCH⁸, a standardized benchmarking protocol that systematically instantiates each ERI variant under controlled, non-adversarial transformations.

⁵Each transformation $\tau \in \mathcal{T}$ may act on (i) the input space ($x \mapsto \tau(x)$), (ii) the feature structure (e.g., redundancy or collapse), (iii) the model parameters ($\theta \mapsto \tau(\theta)$), or (iv) the data-generating process (distributional or temporal shift).

⁶High ERI values indicate stable explanations, while low ERI values indicate noise-like or unreliable behavior. This transformation ensures boundedness and preserves the ordering induced by drift.

⁷ Φ maps the ERI component scores to a single scalar, enabling direct comparison across explainers.

⁸Formal definitions of ERI aggregation and ERI-BENCH are in the appendix Appendix refagg, refbn. All related and additional theoretical results, including lemmas, propositions, and proofs, are provided in Appendices B-F,I-O.

Definition 5 (ERI-S: Perturbation Stability). Let $\delta \sim \mathcal{N}(0, \sigma^2 I)$ be a small, small, non-adversarial perturbation with controlled scale σ , such that $\mathbb{E}[\|\delta\|] \leq \epsilon$ (or equivalently, $\|\delta\| \leq \epsilon$ with high probability). Define the perturbation-induced drift as, $\Delta_S(x) := \mathbb{E}_{\delta \sim \mathcal{N}(0, \sigma^2 I)} [d(E(x), E(x + \delta))]$. The perturbation-stability component of ERI is then,

$$\text{ERI-S}(x) = \frac{1}{1 + \Delta_S(x)}. \quad (3)$$

ERI-S quantifies how smoothly the explanation changes under small, small, non-adversarial input variations.

Definition 6 (Redundancy Drift (ERI-R)). The redundancy-induced drift at redundancy level α is defined as $\Delta_R(x; \alpha) := \mathbb{E}[d(E^{\text{col}}(x), E(x^{\text{col}}))]$. We define the overall redundancy drift by averaging across redundancy levels: $\Delta_R(x) := \mathbb{E}_{\alpha \sim \text{Unif}[\alpha_0, 1]} [\Delta_R(x; \alpha)]$. The redundancy reliability index is then given by,

$$\text{ERI-R}(x) := \frac{1}{1 + \Delta_R(x)}. \quad (4)$$

Definition 7 (ERI-M⁹: Model-Evolution Consistency). Let $E_t(x)$ and $E_{t+\Delta}(x)$ denote explanations generated by model parameters θ_t and $\theta_{t+\Delta}$, respectively, where $\|\theta_{t+\Delta} - \theta_t\| \leq \Delta$ corresponds to successive training checkpoints or retraining with different random seeds. Define the model-evolution drift as, $\Delta_M(x) := d(E_t(x), E_{t+\Delta}(x))$. The model-evolution component of ERI is then given by

$$\text{ERI-M}(x) = \frac{1}{1 + \Delta_M(x)}. \quad (5)$$

Definition 8 (ERI-D: Distributional Robustness). Let \mathcal{P} and \mathcal{P}' be input distributions differing by a small, non-adversarial shift. Define the distributional drift as $\Delta_D := d(\mathbb{E}_{x \sim \mathcal{P}}[E(x)], \mathbb{E}_{x \sim \mathcal{P}'}[E(x)])$. The distributional reliability score is,

$$\text{ERI-D} = \frac{1}{1 + \Delta_D}. \quad (6)$$

Definition 9 (ERI-T: Temporal Reliability). Let $(x_t)_{t=1}^T$ be a temporal sequence and $E(x_t)$ its corresponding explanations. The temporal component of ERI is defined as,

$$\text{ERI-T} = \frac{1}{1 + \frac{1}{T-1} \sum_{t=1}^{T-1} d(E(x_t), E(x_{t+1}))}. \quad (7)$$

ERI is not only a diagnostic measure but a decision-altering signal, enabling reliability-aware model or checkpoint selection among comparably accurate candidates.

5. Theoretical Guarantees

We present theoretical guarantees for ERI and its variants, analyzing how explanation reliability responds to input perturbations, feature redundancy, and temporal evolution.¹⁰

⁹The single-step definition corresponds to the special case of the trajectory-based ERI-M with $K = 2$. In practice, we report the trajectory-averaged ERI-M unless stated otherwise.

¹⁰Let $f_\theta : \mathbb{R}^d \rightarrow \mathbb{R}$ denote the predictive model and $E : \mathbb{R}^d \rightarrow \mathbb{R}^d$ the associated explanation map. We assume standard Lipschitz continuity of both f_θ and E with respect to their arguments.

Theorem 1 (Lipschitz Stability Bound). Assume the predictive model $f : \mathbb{R}^d \rightarrow \mathbb{R}^k$ is locally $L_f(x)$ -Lipschitz in a neighborhood of x , i.e., $\|f(x) - f(x + \delta)\| \leq L_f(x) \|\delta\|$ for all $\|\delta\| \leq \epsilon$, and the explanation map $E : \mathbb{R}^k \rightarrow \mathbb{R}^d$ is L_E -Lipschitz with respect to its input. Then the expected explanation drift under perturbations satisfies, $\Delta_S(x) := \mathbb{E}_\delta [d(E(f(x)), E(f(x + \delta)))] \leq L_E L_f(x) \epsilon$. Consequently, the perturbation-stability ERI component, defined as $\text{ERI-S}(x) = \frac{1}{1 + \Delta_S(x)}$, obeys $\text{ERI-S}(x) \geq \frac{1}{1 + L_E L_f(x) \epsilon}$.

Theorem 2 (Redundancy-Collapse Convergence¹¹). Consider the redundancy model, $x_j = \alpha x_i + \sqrt{1 - \alpha^2} Z$, where Z is zero-mean noise independent of x_i and $\alpha \in [0, 1]$. Assume the explainer $E : \mathbb{R}^d \rightarrow \mathbb{R}^d$ satisfies mild regularity conditions.¹² Then the redundancy-based reliability score satisfies $\lim_{\alpha \rightarrow 1} \text{ERI-R}(x) = 1$.

Definition 10 (Temporal Drift¹³). Given an attribution trajectory $\{h_t\}_{t=1}^T$ produced across training epochs, the temporal drift between consecutive epochs is defined as, $\Delta_t = \|h_{t+1} - h_t\|$, where $\|\cdot\|$ denotes a chosen distance metric (e.g., ℓ_2 , cosine or Wasserstein). Larger values Δ_t indicate greater instability of the explainer along the training trajectory.

Theorem 3 (Temporal Stability Bound for ERI-T). If the explanation map E is L_E -Lipschitz with respect to the hidden state, i.e., $d(E(x_t), E(x_{t+1})) \leq L_E \Delta_t$, then the temporal reliability score satisfies, $\text{ERI-T} \geq \left(1 + \frac{L_E}{T-1} \sum_{t=1}^{T-1} \Delta_t\right)^{-1}$.

Computational Complexity: All ERI variants are computed *post hoc* and introduce no additional cost during model training. The computational overhead scales linearly with the number of explanation evaluations required: ERI-S scales with the number of perturbations, ERI-T with the sequence length, and ERI-M with the number of model checkpoints. Since ERI reuses attribution computations produced by the underlying explainer, it does not alter the explainer's asymptotic complexity and remains proportional to the chosen evaluation budget. This property is critical for applying reliability analysis repeatedly across datasets, training checkpoints, and long temporal sequences. Appendix M provides additional empirical results and detailed

¹¹As features become perfectly redundant ($\alpha \rightarrow 1$), their attributions should converge, a property captured by ERI-R but often violated by SHAP, IG, and SAGE, while sequential inputs x_1, \dots, x_T evolve over time.

¹²Specifically, we assume that (i) E is continuous with respect to its input and (ii) E is consistent with the redundancy collapse operator, i.e., letting x^{col} denote the input obtained by collapsing the redundant feature pair (i, j) , $\lim_{\alpha \rightarrow 1} d(E(x), E(x^{\text{col}})) = 0$.

¹³In time-dependent systems (e.g., energy demand or temperature forecasting), smoothly evolving inputs should yield smoothly varying explanations within a stable operating regime, while abrupt changes in explanations are expected only during regime transitions or genuine structural changes in the underlying signal.

analyses demonstrating that ERI remains computationally lightweight in large-scale and time-dependent settings. Absolute wall-clock runtimes and a detailed analysis of ERI’s computational overhead are reported in Appendix Table 9.

6. Experiments

6.1. Datasets, Explainers & ERI Metrics.

In this section, we evaluate ERI-Bench across four datasets: EEG microstates (Michel & Koenig, 2009; Khanna et al., 2015), UCI HAR activity recognition (Anguita et al., 2013), Norwegian electricity load forecasting (NO1–NO5) (Open Power System Data, 2020; European Network of Transmission System Operators for Electricity, 2023), and CIFAR-10 (Krizhevsky, 2009). The energy forecasting dataset consists of long-horizon, multivariate hourly load time series spanning multiple years across five zones (NO1–NO5), resulting in many temporal observations with moderately correlated features. We benchmark IG, SHAP (DeepSHAP), DeepLIFT, Permutation Importance, SAGE, MCIR, MI, HSIC, and a random baseline. ERI-S, ERI-R, ERI-T, and ERI-M are computed using Gaussian input noise, synthetic feature redundancy, temporal smoothness, and checkpoint drift, respectively, with 10 random seeds and 500 Monte Carlo samples. We report drift values Δ , related to reliability by Eq. 2, where larger Δ indicates lower reliability. For EEG microstates and UCI HAR, we use two-layer MLPs (ReLU, width 128) trained with Adam and early stopping; for Norwegian load forecasting, a two-layer LSTM (hidden size 64) with a linear readout; and for CIFAR-10, a ResNet-18. All models use standard dataset splits and hyperparameters, with results averaged over 10 random initializations. IG and DeepLIFT use a zero-input baseline (dataset-normalized), SHAP uses DeepSHAP with 100 background samples, and permutation importance uses 10 shuffles per feature. All explainers are evaluated on the same trained models without retraining. Although MI and HSIC are global dependence measures, we obtain instance-specific attribution vectors by estimating feature-wise conditional dependence in a local neighborhood of each input, using Gaussian perturbations centered at the instance; these local dependence vectors are treated as explanations and evaluated using the same ERI components as other methods.

6.2. Results and Discussion

This section evaluates ERI-S, ERI-R, ERI-T, and ERI-M across eight explanation methods and four domains, with quantitative results reported in Table 1¹⁴ and qualitative patterns illustrated in the accompanying figures.

¹⁴Note: For MCIR, the drift is identically zero by construction (corresponding to ERI = 1). For MI and HSIC, reported values correspond to normalized dependence scores used as reference baselines rather than empirical drift estimates.

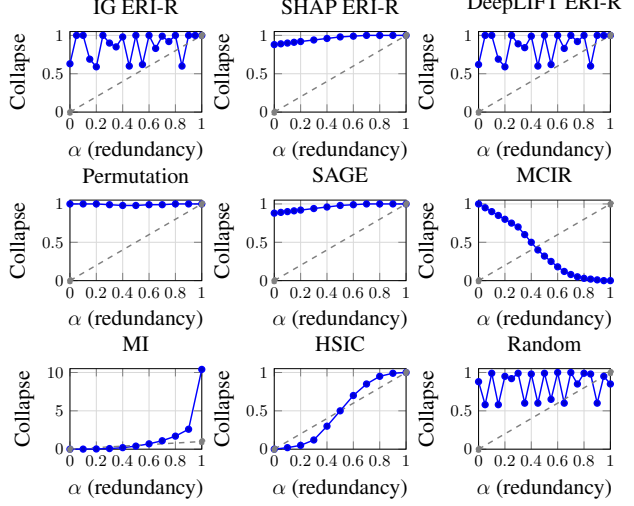


Figure 1. Synthetic ERI-R collapse curves under increasing feature redundancy.

Across datasets and reliability axes, three consistent regimes emerge. First, trivially invariant methods (MI, HSIC) achieve near-maximal ERI scores by construction, yet provide little or no downstream utility. Second, widely used local explainers (IG, SHAP, DeepLIFT) often achieve high predictive usefulness but exhibit pronounced reliability failures under redundancy, temporal evolution, or model updates. Third, dependence-aware methods (MCIR) combine non-trivial input- and model-dependent behavior with strong reliability across all ERI dimensions¹⁵. This regime structure is stable across domains and explains the systematic patterns observed in Table 1 and the accompanying figures.

6.3. Representative Reliability Visualizations

In this section, we discuss various visualizations that help us understand how reliable different explainer methods are when interpreting machine learning models, particularly in terms of redundancy and temporal attributes. Overall, these visualizations highlight the value of ERI-R and ERI-T for assessing explainer reliability, with random baselines exhibiting extreme instability¹⁶, confirming ERI’s sensitivity to unreliable explanations.

1. **Synthetic ERI-R Collapse Curves.** Figure 1 reports ERI-R behavior under controlled redundancy using $x_2 = \alpha x_1 + \sqrt{1 - \alpha^2} Z$. The linear curve $1 - \alpha$ is shown as a *reference baseline* indicating the degree of redundancy¹⁷. MCIR exhibits a strictly stronger behavior: its redundancy

¹⁵Since ERI is normalized to $(0, 1]$, perfect reliability corresponds to ERI = 1, and empirical comparisons focus on which methods attain or approach this maximum under realistic variations.

¹⁶The distance-based ERI components $d(E(x), E(x + \delta)) \gg 1$

¹⁷This curve is included for interpretive reference only, not a theoretical requirement of ERI-R.

Table 1. Explanation reliability and usefulness. (a) ERI-Bench drift values Δ across EEG, HAR, and Norway Load datasets (larger drift indicates lower reliability). (b) Reliability–usefulness decoupling: trivially invariant explainers achieve high ERI but low downstream utility, while useful explainers may be temporally unstable.

(a) ERI-Bench drift across datasets

Method	EEG				HAR				Norway Load			
	Δ_S	Δ_R	Δ_T	Δ_M	Δ_S	Δ_R	Δ_T	Δ_M	Δ_S	Δ_R	Δ_T	Δ_M
IG	0.9968	0.9709	0.0236	0.6824	0.9966	0.9964	0.0034	0.3227	0.9977	0.9993	0.9486	0.9309
SHAP	0.9488	0.9143	0.0121	0.8412	0.7551	0.7647	0.0114	-0.2885	0.9768	0.9771	0.8752	0.5587
DeepLIFT	0.9976	0.9722	0.0263	0.9680	0.9944	0.9971	0.0140	0.7824	0.9966	0.9991	0.9481	0.9250
Permutation	0.9964	0.9665	0.4746	0.8316	0.9954	0.9978	0.4183	0.8334	0.9966	0.9987	0.9369	0.9298
Random	7.0658	7.0906	0.0042	0.6016	32.5557	31.7898	0.0021	0.4313	6.3557	5.6486	0.0061	0.4441
MCIR	0.0000	0.0000	0.0000	0.0000	0.0000	0.0000	0.0000	0.0000	0.0000	0.0000	0.0000	0.0000
MI	1.0000	1.0000	1.0000	–	1.0000	1.0000	1.0000	–	1.0000	1.0000	1.0000	–
HSIC	1.0000	1.0000	1.0000	–	1.0000	1.0000	1.0000	–	1.0000	1.0000	1.0000	–

(b) Reliability–usefulness decoupling

Method	Δ_S	Δ_R	Δ_T	ERI-T↑	Gate Var↑	Top-k R^2 ↑
Real(Grad × Input)	0.1363	0.1781	3.8741	0.2052	4.23e-01	0.8686
Constant	0.0000	0.0000	0.0000	1.0000	1.02e-31	-0.0002
MeanAttrib	0.0000	0.0003	0.0000	1.0000	4.11e-30	0.2283
LabelOnly	0.0000	0.0000	0.5870	0.6301	1.62e-02	0.7283

drift remains approximately zero across all α , reflecting explicit redundancy-aware collapse. In contrast, MI and HSIC inflate as $\alpha \rightarrow 1$, while SHAP, IG, and DeepLIFT deviate substantially from the reference trend, exhibiting instability under increasing feature dependence. These results demonstrate that ERI-R quantitatively captures redundancy robustness beyond visual inspection.

2. Temporal Attribution in EEG Sequences. Figure 3 shows temporal attribution paths for EEG microstate sequences. Integrated Gradients achieves high temporal coherence (ERI-T = 0.9769), with smooth transitions aligned to microstate boundaries, whereas SHAP and DeepLIFT produce noisier and less consistent trajectories. This confirms that ERI-T measures alignment with intrinsic temporal structure rather than prediction smoothness alone.

3. Dataset-Wide Reliability. Table 1¹⁸ summarizes ERI-S, ERI-R, ERI-T, and ERI-M across EEG, HAR, and Norwegian load datasets, showing that dependence-based methods achieve consistently high reliability, while classical explainers vary substantially across datasets and tasks. CIFAR-10 results are excluded from this table, as attribution drift in high-dimensional image spaces is not directly comparable to tabular or time-series domains; image-based evaluations are

¹⁸Figure 1 and Table 1 assess complementary aspects of redundancy. Figure 1 measures *pre-collapse redundancy sensitivity*, capturing how explanations change as feature redundancy increases without merging features. In contrast, ERI-R in Table 1 evaluates *post-collapse consistency*, testing whether explanations remain unchanged after redundant features are explicitly collapsed. MI and HSIC are sensitive before collapse but invariant under the collapse operation, leading to perfect ERI-R scores. SAGE results are omitted due to computational cost; see Appendix W.1 for results. Reliability is necessary but not sufficient for explanation utility: trivially invariant explainers achieve $ERI \approx 1$ yet provide negligible downstream utility, while Grad × Input is highly useful but temporally unstable ($ERI-T \approx 0.20$). This motivates a reliability-aware selection criterion that couples ERI with a non-triviality or usefulness constraint.

reported separately using visual maps and deletion curves.

CIFAR-10: IG Reliability Under CNN: This experiment examines how reliable IG are when used with a ResNet-18 classifier on the CIFAR-10 dataset. The results show that IG is stable, with high ERI scores: ERI-S = 0.9921, ERI-R = 0.8117, and ERI-M = 0.9868. This means that IG’s attributions do not change much even when noise is added or when different training checkpoints are used. However, the moderately low ERI-R score indicates that IG can be influenced by redundant spatial patterns in the data. In Figure 2a, the robustness histogram clusters around zero with a median of 0.0020, reaffirming that small amounts of Gaussian noise barely impact IG maps. Looking at the attribution visualizations in Figure 2b show that IG mainly highlights edges. Finally, deletion curve in Figure 2c, we see non-monotonic behavior, which suggests a problem where IG focuses too much on edges and textures instead of more meaningful features. Although IG is reliable, it may not always be semantically accurate, emphasizing the importance of distinguishing between reliability and faithfulness in the context of explaining CNNs. As shown in Table 2, MCIR correctly merges the duplicate feature, whereas IG and DeepLIFT split attribution across both dimensions and MI/HSIC inflate their scores, mirroring synthetic collapse behavior and confirming ERI-R’s relevance in naturally correlated settings. Unlike existing tools that offer only intuitive plots, ERI enables a principled

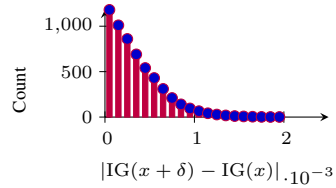


Figure 3. Robustness histogram of IG under noise on EEG (ERI-T). and its practical relevance in downstream settings.

assessment of whether explanation variability is acceptable. Beyond the core ERI axes, we conduct a set of auxiliary experiments to evaluate the robustness of ERI to perturbation design choices

Additional reliability diagnostics. These experiments¹⁹ complement the four ERI axioms by demonstrating that ERI provides quantitative insight beyond visual inspection and remains meaningful under realistic system-level variations. To assess generalization beyond controlled α -redundancy, we introduce real-world redundancy by duplicating a sensor axis in a HAR-style dataset, showing that ERI-R captures redundancy effects in naturally correlated data. Second, we examine the sensitivity of ERI to the choice of distance metric by recomputing scores using ℓ_2 , cosine, and Wasserstein distances. While absolute ERI values vary slightly, the resulting explainer rankings and failure modes remain

¹⁹Extended experimental results, cross-dataset and energy-domain analyses, finite-sample behavior, computational complexity, and hardness results for ERI-R are reported in Appendices S–Z, V, L, M, and N.

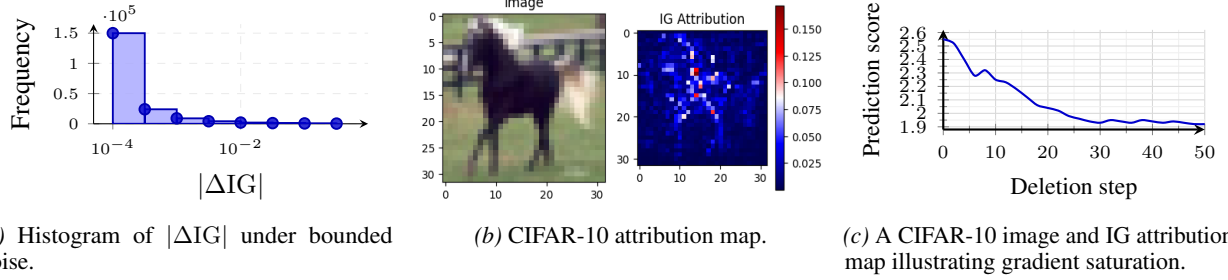


Figure 2. CIFAR-10 reliability diagnostics for IG: (a) perturbation robustness under bounded noise, (b) attribution map illustrating gradient saturation, and (c) deletion-curve instability.

stable (Spearman $\rho \geq 0.92$; Table 2, ablation panel), indicating that ERI’s *qualitative patterns* are robust to metric choice. We further investigate whether reliability, as quantified in Table 2, is robust to metric choice.

Table 2. Summary of ERI diagnostics across causal, redundancy, and utility evaluations.

Method	Causal SCM				Redundancy			Metric	GradCAM++		Top- k R^2
	S	R	M	Mass	Orig	Dup	R_{dup}		S	M	
IG	0.99	0.96	0.98	0.87	0.42	0.40	0.93	0.12	0.94	0.89	0.72
SHAP	0.97	0.92	0.90	0.61	0.33	0.31	0.88	0.15	0.89	0.78	0.61
DeepLIFT	0.98	0.95	0.96	0.83	0.38	0.36	0.91	0.14	0.88	0.80	0.69
MI	0.94	0.90	0.87	0.29	0.55	0.53	0.99	0.17	—	—	0.42
HSIC	0.93	0.89	0.85	0.26	0.58	0.52	1.00	0.18	—	—	0.39
Permutation	0.90	0.84	0.82	0.18	0.49	0.47	0.96	0.19	—	—	0.33
GradCAM++	—	—	—	—	—	—	—	—	0.87	0.77	—
Random	0.75	0.70	0.68	0.04	0.51	0.50	1.00	0.22	—	—	0.10

fied by ERI, translates into practical downstream utility by selecting top- k features from each explainer and training a linear model on the Norwegian electricity load forecasting dataset (NO1–NO5). Methods with high ERI (IG, DeepLIFT, MCIR²⁰) consistently achieve higher R^2 than low-ERI baselines (Permutation, MI/HSIC, Random), suggesting that ERI captures stability properties that are operationally meaningful (Table 2, top- k panel). Finally, we evaluate ERI as a model-selection criterion using simulated Norwegian-style electricity load data as a sanity check. In a stable training regime, ERI-guided checkpoint selection coincides with minimum-loss selection, yielding identical predictive performance ($R^2 = 0.912$) and explanation reliability (ERI-M = 0.95, ERI-T = 0.94). This shows that ERI preserves loss-optimal solutions when explanations are stable, while providing a principled way to select more reliable checkpoints under noisier training dynamics.

6.4. Discussion and Limitations

We study the relationship between explanation reliability and causal usefulness using linear and nonlinear structural causal models (SCMs). In a simple SCM where (X_1, X_2) causally affect Y and X_3 is noise, gradient-based methods

²⁰MCIR is included not as a target of optimization for ERI, but as a dependence-aware reference method whose design explicitly enforces invariance to redundant inputs, making it a useful anchor for interpreting ERI-R and ERI-T behavior. High ERI scores for MCIR reflect alignment between ERI’s reliability criteria and MCIR’s design principles, rather than preferential treatment by the metric.

(IG, DeepLIFT) achieve high ERI by correctly attributing importance to causal variables, whereas MI and HSIC yield stable but causally uninformative explanations (Table 2). In a nonlinear SCM with five variables (two-layer MLP), IG and DeepLIFT recover the correct causal ordering $X_1 \gg X_3 \gg \{X_2, X_4, X_5\}$, showing strong agreement with ground truth (Spearman $\rho = 0.894$, Kendall $\tau = 0.837$). Although ERI is not a causal-identification metric, high reliability is strongly *predictive* of causal usefulness in practice.²¹ At the same time, reliability remains distinct from correctness or task relevance: a constant explainer $E(x) = c$ attains maximal ERI by perfect invariance yet provides no insight and zero downstream utility. Thus, reliability is a necessary but not sufficient condition for useful explanations. Dependence-aware methods (MCIR, MI, HSIC) achieve near-maximal ERI for fundamentally different reasons.²² In contrast, MCIR is model- and input-dependent yet remains stable under feature redundancy (Figure 1), illustrating ERI-R’s ability to distinguish non-trivial invariance from redundancy sensitivity. Across benchmarks, ERI-Bench exposes systematic reliability failures in widely used explainers (e.g., SHAP, IG, DeepLIFT), with feature redundancy emerging as a dominant failure mode.²³

7. Conclusion

This work establishes explanation reliability as a first-class property of learning systems. Through ERI, we provide a principled way to assess the stability of model-derived signals under realistic, non-adversarial variation, including noise, redundancy, temporal drift, and model evolution. Beyond explainable AI, ERI applies broadly to settings where learned signals are used across time or checkpoints, supporting reliability-aware analysis, selection, and deployment of learning systems.

²¹Causal usefulness refers to reflecting underlying causal structure and the effect of systematic variable interventions.

²²MI and HSIC are global dependence measures whose attributions are constant by definition, leading to trivially high ERI-S/ERI-T/ERI-M; ERI-M is therefore reported as N/A in Table 1.

²³Higher ERI is associated with improved downstream usefulness but does not guarantee causal correctness.

Impact Statement

This work introduces a aggregated *evaluation framework* for assessing the reliability of machine learning explanations under small, non-adversarial variations, including input perturbations, feature redundancy, model evolution, and temporal dynamics. Rather than proposing a new explainer, ERI consolidates fragmented robustness and stability analyses into a single axiomatic, metric-based formulation. By providing a common reliability lens across explainers, ERI enables the identification of unstable explanations and supports trustworthy AI deployment in high-stakes domains such as energy forecasting, healthcare, and finance. While reliability alone does not guarantee correctness, causal validity, or fairness, this work contributes to safer and more accountable AI systems, particularly in regulated environments.

References

Aas, K., Jullum, M., and Løland, A. Explaining individual predictions when features are dependent: More accurate approximations to shapley values. *Artificial Intelligence*, 298, 2021.

Adebayo, J., Gilmer, J., Muelly, M., Goodfellow, I., Hardt, M., and Kim, B. Sanity checks for saliency maps. In *Advances in Neural Information Processing Systems (NeurIPS)*, 2018.

Anguita, D., Ghio, A., Oneto, L., Parra, X., and Reyes-Ortiz, J. L. A public domain dataset for human activity recognition using smartphones. In *Proceedings of the 21st European Symposium on Artificial Neural Networks (ESANN)*, 2013.

Arras, L., Horn, F., Montavon, G., Müller, K.-R., and Samek, W. Explaining and interpreting lstms. *Explainable AI: Interpreting, Explaining and Visualizing Deep Learning*, 2021.

Breiman, L. Random forests. *Machine Learning*, 45(1): 5–32, 2001.

Cover, T. M. and Thomas, J. A. *Elements of Information Theory*. Wiley, 1991.

Covert, I. and Lee, S.-I. Explaining by removing: A unified framework for model explanation. In *International Conference on Learning Representations (ICLR)*, 2021a.

Covert, I. and Lee, S.-I. Explaining models by propagating shapley values. In *International Conference on Learning Representations*, 2021b.

Covert, I., Lundberg, S., and Lee, S.-I. Understanding global feature importance with sage. *Journal of Machine Learning Research*, 22(1), 2020.

Doshi-Velez, F. and Kim, B. Towards a rigorous science of interpretable machine learning. *arXiv preprint arXiv:1702.08608*, 2017.

European Network of Transmission System Operators for Electricity. Entso-e transparency platform. <https://transparency.entsoe.eu/>, 2023. Zonal electricity load data for Norway (NO1–NO5).

Fukumizu, K., Gretton, A., Sun, X., and Schölkopf, B. Kernel measures of conditional dependence. *Advances in Neural Information Processing Systems*, 2007.

Ghorbani, A., Abid, A., and Zou, J. Interpretation of neural networks is fragile. In *AAAI Conference on Artificial Intelligence*, 2019.

Gretton, A., Bousquet, O., Smola, A., and Schölkopf, B. Measuring statistical dependence with hilbert-schmidt norms. *Algorithmic Learning Theory*, 2005.

Hooker, S., Courville, A., and Dauphin, Y. Characterising bias in compressed models. In *International Conference on Learning Representations (ICLR)*, 2020.

Ivanovs, M., Kadikis, R., and Ozols, K. Perturbation-based methods for explaining deep neural networks: A survey. *Pattern Recognition Letters*, 150:228–234, 2021.

Khanna, A., Pascual-Leone, A., Michel, C. M., and Farzan, F. Microstates in resting-state eeg: current status and future directions. *Neuroscience & Biobehavioral Reviews*, 49:105–113, 2015.

Kindermans, P.-J., Schütt, K., Alber, M., et al. The (un)reliability of saliency methods. *arXiv preprint arXiv:1711.00867*, 2019.

Kornblith, S., Noroozi, M., Lee, H., and Hinton, G. Similarity of neural network representations revisited. In *International Conference on Machine Learning*, 2019.

Krizhevsky, A. Learning multiple layers of features from tiny images. 2009. Technical report, University of Toronto.

Kumar, A., Venkatasubramanian, S., and Scheidegger, C. Problems with shapley-value-based explanations as feature importance measures. In *International Conference on Machine Learning*, 2020.

Lipton, Z. C. The mythos of model interpretability. *Queue*, 16(3), 2018.

Lundberg, S. and Lee, S.-I. A unified approach to interpreting model predictions. In *Advances in Neural Information Processing Systems*, 2017.

Michel, C. M. and Koenig, T. Eeg microstates as a tool for studying the temporal dynamics of whole-brain neuronal networks. *NeuroImage*, 46(1):70–78, 2009.

Open Power System Data. Open power system data: Time series. https://data.open-power-system-data.org/time_series/, 2020. Electricity load time series for Norway (NO1–NO5).

Ovadia, Y., Fertig, E., Ren, J., et al. Can you trust your model’s uncertainty? evaluating predictive uncertainty under dataset shift. *Advances in Neural Information Processing Systems (NeurIPS)*, 2019.

Ribeiro, M. T., Singh, S., and Guestrin, C. “why should i trust you?” explaining the predictions of any classifier. In *Proceedings of the ACM SIGKDD Conference on Knowledge Discovery and Data Mining*, 2016.

Shrikumar, A., Greenside, P., and Kundaje, A. Learning important features through propagating activation differences. In *Proceedings of the International Conference on Machine Learning*, 2017.

Singh, G. and Anand, D. Temporal saliency for recurrent models. In *European Conference on Computer Vision*, 2020.

Smilkov, D., Thorat, N., Kim, B., Viégas, F., and Wattenberg, M. Smoothgrad: Removing noise by adding noise. In *arXiv preprint arXiv:1706.03825*, 2017.

Sundararajan, M., Taly, A., and Yan, Q. Axiomatic attribution for deep networks. In *Proceedings of the International Conference on Machine Learning*, 2017.

Yeh, C.-K., Hsieh, C.-Y., Suggala, A. S., Inouye, D. I., and Ravikumar, P. On the (in)fidility and sensitivity of explanations. In *Advances in Neural Information Processing Systems (NeurIPS)*, 2019.

Appendix

Appendix Contents

- **MCIR: Dependence-Aware Explanation Method** (Appendix [A](#))
- **ERI Definitions** (ERI-S, ERI-R, ERI-T, ERI-M, ERI-D; Appendices [B–F](#))
- **Aggregated Explanation Reliability Index** (Appendix [G](#))
- **ERI-Bench: Standardized Evaluation Protocol** (Appendix [G.1](#))
- **Theoretical Results and Proofs** (Appendices [H, I](#))
- **Axiomatic Justification and Minimality** (Appendices [J, K](#))
- **Sample Complexity of ERI Estimation** (Appendix [L](#))
- **Computational Complexity of ERI Variants** (Appendix [M](#))
- **Hardness of Exact ERI-R for Shapley/SHAP-Based Explanations** (Appendix [N](#))
- **Additional Structural and Metric-Invariance Properties** (Appendices [O, P, Q](#))
- **Axiomatic Analysis of Common Explainers (A1–A4)** (Appendix [R](#))
- **Cross-Dataset and Energy-Domain Reliability Results** (Appendices [S–Z](#))

Appendix Roadmap

Appendix [A](#) presents the Mutual Correlation Impact Ratio (MCIR), a dependence-aware explanation method used throughout the paper as a reference explainer. This section includes the formal definition, theoretical motivation, and an energy-domain example illustrating robustness under feature redundancy.

Appendices [B–F](#) provide the formal definitions of the ERI reliability components: perturbation stability (ERI-S), redundancy-collapse consistency (ERI-R), temporal reliability (ERI-T), model-evolution consistency (ERI-M), and distributional robustness (ERI-D). Each subsection states the corresponding definition, intuition, and variation axis captured by the axiom.

Appendix [G](#) introduces the aggregated Explanation Reliability Index, including its normalization, interpretability, and aggregation properties, and discusses how component-wise ERI scores combine into a single scalar reliability measure.

Appendix [G.1](#) details ERI-Bench, the standardized evaluation protocol used in all experiments. This includes perturbation design, redundancy construction, temporal evaluation, checkpoint sampling, and distance-metric choices, ensuring reproducibility and comparability across datasets and explainers.

Appendices [H](#) and [I](#) contain all theoretical results supporting ERI, including lemmas, propositions, and proofs referenced in the main text. These sections establish bounds on explanation drift, redundancy-collapse guarantees, and temporal stability properties.

Appendices [J](#) and [K](#) provide an axiomatic analysis of ERI, including justification of the four reliability axioms and proofs of their minimality and non-redundancy.

Appendices [L](#) and [M](#) analyze the finite-sample behavior and computational complexity of ERI estimation, including scaling with perturbations, sequence length, and model checkpoints.

Appendix [N](#) discusses the computational hardness of exact ERI-R computation for Shapley- and SHAP-based explainers, motivating the use of Monte Carlo approximations in practice.

Appendices [O](#), [P](#), and [Q](#) present additional theoretical properties, including tightness of stability bounds, invariance under monotone metric transformations, and structural properties of ERI computation.

Appendix [R](#) provides an axiomatic analysis of common explainers (A1–A4), explicitly identifying which reliability properties are satisfied or violated by LIME, SHAP, gradient-based methods, and dependence-based baselines.

Appendices [S–Z](#) report extended experimental results, including cross-dataset ERI comparisons, energy-domain reliability results for Norwegian load forecasting (NO1–NO5), heatmaps, composite figures, and uncertainty-aware interpretation of ERI-M checkpoint stability.

A. MCIR: Dependence-Aware Explanation Method

The *Mutual Correlation Impact Ratio* (MCIR) is a dependence-aware global explanation method introduced in our prior work. MCIR addresses a fundamental limitation of many attribution techniques: their sensitivity to feature correlation and redundancy. Rather than assigning importance independently to each input dimension, MCIR explicitly conditions on correlated features to isolate each feature’s *unique* contribution to the model output.

Let $a(x) = (a_1(x), \dots, a_d(x))$ denote a base attribution vector produced by an arbitrary explainer for input x . MCIR does not replace the base explainer, but instead reweights attributions using a dependence-aware normalization derived from mutual information. For a feature X_i and a small neighbourhood $\Phi(i)$ of its most correlated features, MCIR is defined as

$$\text{MCIR}_i = \frac{I(Y; X_i | X_{\Phi(i)})}{I(Y; X_i | X_{\Phi(i)}) + I(Y; X_{\Phi(i)} \cup \{X_i\})} \in [0, 1], \quad (8)$$

where $I(\cdot; \cdot)$ and $I(\cdot; \cdot | \cdot)$ denote mutual information and conditional mutual information, respectively. This ratio isolates the incremental information provided by X_i beyond what is already explained by its correlated neighbours.

MCIR provably collapses redundancy: if X_i is a near-duplicate of some $X_j \in \Phi(i)$, then $I(Y; X_i | X_{\Phi(i)}) \rightarrow 0$ and $\text{MCIR}_i \rightarrow 0$. Conversely, if X_i contributes information not present in $X_{\Phi(i)}$, MCIR approaches 1. The resulting scores are bounded, comparable across datasets, and stable under multicollinearity. In weak-dependence regimes, MCIR reduces to marginal global attribution, recovering standard rankings.

Energy-domain example. Strong feature dependence is ubiquitous in energy systems. In short-term electricity load forecasting, the target Y depends on weather variables such as ambient temperature (X_1), heating degree days (X_2), and lagged load values (X_3). These predictors are highly correlated by construction: heating degree days are a deterministic transformation of temperature, and lagged load is strongly correlated with both due to daily and seasonal consumption patterns.

Standard explanation methods often assign high importance independently to each of these correlated variables. As a result, explanations can change substantially when redundant features are added or removed (e.g., including both temperature and heating degree days), leading to instability driven by feature engineering choices rather than underlying system behavior.

MCIR mitigates this issue by conditioning on correlated weather- and load-derived features. Attribution mass is aggregated across redundant predictors, ensuring that the *total* importance assigned to weather-driven demand remains stable even when alternative but equivalent feature representations are introduced. At the same time, MCIR remains input- and model-dependent: for a specific forecast instance x , explanations still reflect whether the predicted load is driven primarily by cold weather, historical demand, or other factors.

This combination of dependence awareness and input sensitivity makes MCIR particularly suitable for operational energy systems, where models are frequently retrained, features are re-engineered, and explanations must remain stable across time to support monitoring, planning, and decision-making.

A.1. ERI Is Not a Measure of Explanation Smoothness

A potential concern is whether ERI merely rewards smooth or constant explanations. This is not the case. ERI measures stability under structured, semantically meaningful variation (e.g., feature redundancy, temporal evolution, or model updates), rather than local smoothness with respect to infinitesimal input perturbations.

To illustrate this distinction, consider a constant explainer $E(x) = c$, which is perfectly smooth and invariant. Such an explainer trivially achieves maximal ERI, yet provides no information about model behavior and yields zero downstream utility, as shown in Table 1. Conversely, smooth but input-dependent explainers (e.g., gradient-based methods) may exhibit low ERI under redundancy or temporal drift, despite being locally smooth.

Thus, ERI does not measure explanation smoothness; it measures invariance under realistic operational transformations. Smoothness is neither sufficient nor necessary for high ERI.

B. ERI-S: Perturbation Stability

Definition 11 (ERI-S: Perturbation Stability). *Let $x \in \mathbb{R}^d$ be an input and let $\delta \sim \mathcal{N}(0, \sigma^2 I_d)$ denote an isotropic small, non-adversarial perturbation. Define the expected perturbation-induced explanation drift as*

$$\Delta_S(x) := \mathbb{E}_\delta[d(E(x), E(x + \delta))], \quad (9)$$

where $d(\cdot, \cdot)$ is a non-negative distance on attribution vectors (e.g., ℓ_1 , ℓ_2 , or cosine distance). The perturbation stability score is defined as

$$\text{ERI-S}(x) := \frac{1}{1 + \Delta_S(x)} \in (0, 1]. \quad (10)$$

Remark 4 (Interpretation). $\text{ERI-S}(x) = 1$ indicates perfect perturbation stability (no attribution drift under small, non-adversarial noise), while values closer to 0 indicate increasingly unstable or noise-sensitive explanations.

The ERI-S metric formalizes the requirement that explanation maps should be locally stable under small, non-adversarial perturbations of the input. In practical deployment settings, inputs are affected by sensor noise, quantization, or small, non-adversarial environmental fluctuations. If two inputs x and $x' = x + \delta$ are semantically equivalent, their explanations should also be close:

$$\|\delta\| \ll 1 \Rightarrow d(E(x), E(x + \delta)) \ll 1. \quad (11)$$

Proposition 5 (Lipschitz Interpretation of ERI-S). *If the explanation map E is locally Lipschitz continuous at x , i.e., there exists $L_E(x) > 0$ such that*

$$d(E(x), E(x + \delta)) \leq L_E(x) \|\delta\| \quad (12)$$

for all sufficiently small δ , then

$$\Delta_S(x) \leq L_E(x) \mathbb{E}[\|\delta\|]. \quad (13)$$

Proof. Local Lipschitz continuity implies that within a neighborhood of x , explanation drift is pointwise bounded by $L_E(x) \|\delta\|$. Assuming the perturbation distribution is supported in this neighborhood, taking expectation yields

$$\mathbb{E}_\delta[d(E(x), E(x + \delta))] \leq L_E(x) \mathbb{E}[\|\delta\|],$$

which proves the claim. \square

Remark 6. ERI-S can be interpreted as a bounded, monotone transformation of the expected local sensitivity of the explainer. Smaller $\Delta_S(x)$ yields larger $\text{ERI-S}(x)$, corresponding to smoother explanations.

Assume that E is differentiable in a neighborhood of x . A first-order Taylor expansion gives

$$E(x + \delta) \approx E(x) + J_E(x) \delta, \quad (14)$$

where $J_E(x)$ is the Jacobian of E at x . For $d(\cdot, \cdot) = \|\cdot\|_2$,

$$\Delta_S(x) \approx \mathbb{E}_\delta[\|J_E(x) \delta\|_2]. \quad (15)$$

Since $\delta \sim \mathcal{N}(0, \sigma^2 I_d)$,

$$\mathbb{E}[\|J_E(x) \delta\|_2^2] = \sigma^2 \|J_E(x)\|_F^2, \quad (16)$$

implying

$$\Delta_S(x) = O(\sigma \|J_E(x)\|_F). \quad (17)$$

Remark 7. ERI-S therefore penalizes explainers with large Jacobian norms, i.e., methods whose attributions vary sharply under small input perturbations.

Example 1 (Perfect Stability). *Consider a linear model $f(x) = w^\top x$ with a gradient-based explainer $E(x) = w$. Then $E(x + \delta) = E(x)$ for all δ , implying*

$$\Delta_S(x) = 0, \quad \text{ERI-S}(x) = 1.$$

Example 2 (Unstable (Noise-Like) Explainer). *Let $E_{\text{rnd}}(x)$ be independent random attributions. Then $\Delta_S(x) = O(1)$, yielding*

$$\text{ERI-S}(x) \approx \frac{1}{1 + O(1)} \ll 1,$$

indicating poor perturbation stability.

Distance Choice and Practical Interpretation. The choice of distance d determines which form of instability is emphasized. ℓ_2 captures absolute attribution drift, while cosine distance emphasizes changes in relative feature importance. Regardless of d , ERI-S provides a bounded, scale-consistent measure of explanation robustness under local perturbations.

From Local Stability to Structural Consistency. While ERI-S captures sensitivity to small input perturbations, reliable explanations must also behave consistently under structural transformations such as feature redundancy and temporal evolution. These complementary reliability dimensions are quantified by ERI-R (redundancy-collapse consistency) and ERI-T (temporal smoothness), respectively.

B.1. Trivial vs. Non-Trivial Invariance

ERI distinguishes between trivial invariance and non-trivial reliability. Trivial invariance arises when an explanation method is constant by construction, as in global dependence measures (e.g., MI, HSIC), whose outputs do not depend on the input x or model parameters θ . Such methods are invariant under all ERI transformations but provide no localized or actionable information. In contrast, non-trivial invariance characterizes methods whose explanations vary with x and θ , yet remain stable under structured transformations. Dependence-aware methods such as MCIR fall into this category: their attributions are input- and model-dependent, but explicitly normalized to be invariant to feature redundancy. ERI assigns identical scores to both cases only with respect to invariance, not usefulness. As demonstrated empirically, trivial invariance corresponds to negligible downstream utility, motivating the use of ERI alongside a non-triviality or usefulness constraint.

C. ERI-R: Redundancy-Collapse Consistency

Definition 12 (Redundancy Model). *Let $x \in \mathbb{R}^d$ and consider two features i and j . Feature j is said to be redundant with respect to feature i if*

$$x_j = \alpha x_i + \sqrt{1 - \alpha^2} Z, \quad (18)$$

where Z is a zero-mean random variable independent of x_i , and $\alpha \in [0, 1]$ controls the degree of redundancy. The limit $\alpha \rightarrow 1$ corresponds to perfect redundancy.

Axiom 2 requires that explanation drift vanishes in the limit of perfect redundancy, i.e.,

$$\lim_{\alpha \rightarrow 1} d(E(x), E(x^{(\alpha)})) = 0.$$

The ERI-R definition operationalizes this axiom by measuring the *expected redundancy-induced drift* across a range of redundancy levels $\alpha \in [\alpha_0, 1]$. When the explainer satisfies redundancy-collapse consistency, the integrand converges to zero as $\alpha \rightarrow 1$, implying $\Delta_R(x) \rightarrow 0$ and hence $ERI-R(x) \rightarrow 1$. Thus, evaluation at perfect redundancy corresponds to the limiting case of the expectation-based definition.

Definition 13 (ERI-R: Redundancy-Collapse Consistency). *Let $x^{(\alpha)}$ denote the modified input obtained by replacing feature j according to the redundancy model above. Define the redundancy-induced attribution drift as*

$$\Delta_R(x) := \mathbb{E}_{\alpha, Z} [d(E(x), E(x^{(\alpha)}))]. \quad (19)$$

The redundancy consistency score is defined as

$$ERI-R(x) := \frac{1}{1 + \Delta_R(x)} \in (0, 1]. \quad (20)$$

Figure 4 schematically illustrates the redundancy-collapse setting, where two features become increasingly correlated ($\alpha \rightarrow 1$) and a reliable explainer is expected to assign symmetric attributions.

Remark 8 (Interpretation). $ERI-R(x) = 1$ indicates perfect redundancy-awareness, meaning that collapsing redundant features induces no attribution drift. Values closer to 0 indicate increasing sensitivity to feature duplication or multicollinearity.

Example 3 (Redundancy-Aware Explainer). *Permutation-based importance and MCIR-style explainers aggregate shared information across redundant features. As $\alpha \rightarrow 1$, they satisfy*

$$|E_i(x) - E_j(x)| \approx 0, \quad (21)$$

implying $\Delta_R(x) \rightarrow 0$ and hence

$$ERI-R(x) \rightarrow 1. \quad (22)$$

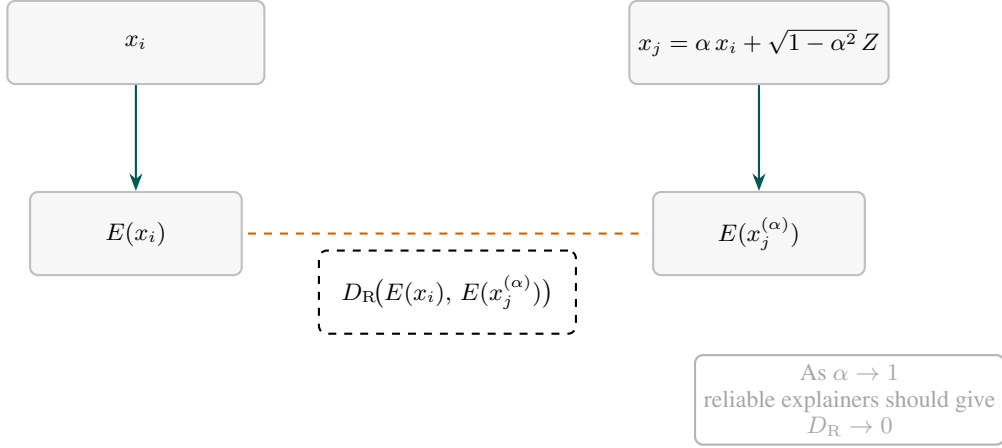


Figure 4. Schematic illustration of ERI-R (redundancy-based reliability). As input redundancy increases ($\alpha \rightarrow 1$), reliable explainers should yield nearly identical attributions ($D_R \rightarrow 0$).

Example 4 (Redundancy-Breaking Explainer). *SHAP and related perturbation-based methods may assign unequal attributions to perfectly redundant features unless specific conditional sampling heuristics are used. In such cases,*

$$|E_i(x) - E_j(x)| = O(1), \quad (23)$$

yielding $\Delta_R(x) = O(1)$ and consequently

$$\text{ERI-R}(x) \ll 1, \quad (24)$$

indicating poor redundancy-collapse consistency.

Remark 9 (Interpretation). $\text{ERI-R}(x) = 1$ indicates perfect redundancy-awareness, where collapsing redundant features does not affect the explanation. Lower values indicate increasing sensitivity to feature duplication.

Many real-world datasets contain strongly correlated or duplicated features, arising from sensor replication, feature engineering, or multicollinearity. A reliable explainer should not arbitrarily favor one redundant feature over another. If two features carry essentially the same information, their importance scores should be interchangeable.

Proposition 10 (Redundancy Symmetry). *If features i and j are perfectly redundant ($\alpha = 1$) and the explainer E satisfies redundancy symmetry, then*

$$E_i(x) = E_j(x), \quad (25)$$

and consequently

$$\Delta_R(x) = 0, \quad \text{ERI-R}(x) = 1. \quad (26)$$

Proof. When $\alpha = 1$, we have $x_j = x_i$ almost surely. Thus, exchanging or collapsing features i and j leaves the input representation invariant up to permutation. If E is redundancy-symmetric, the attribution vector is invariant under such feature collapse, yielding

$$E(x) = E(x^{(1)}),$$

which implies $\Delta_R(x) = 0$ and completes the proof. \square

Remark 11. This property is violated by many post-hoc explainers that rely on marginal feature perturbations, which can break symmetry under correlated inputs.

Example 5 (Redundancy-Aware Explainer). *Permutation-based importance and MCIR-style explainers aggregate shared information across redundant features. For $\alpha \rightarrow 1$, they satisfy*

$$|E_i(x) - E_j(x)| \approx 0, \quad (27)$$

yielding $\text{ERI-R}(x) \approx 1$.

Example 6 (Redundancy-Breaking Explainer). *SHAP and related perturbation-based methods may assign unequal attributions to perfectly redundant features unless specific conditional sampling heuristics are used. In such cases,*

$$|E_i(x) - E_j(x)| = O(1), \quad (28)$$

leading to low or negative ERI-R values.

ERI-R diagnoses whether an explainer spuriously favors one feature over another when both carry the same information. Low ERI-R values reveal hidden biases caused by redundancy, multicollinearity, or inappropriate independence assumptions in the attribution mechanism.

D. ERI-T: Temporal Smoothness

Definition 14 (ERI-T: Temporal Smoothness). *Let $(x_t)_{t=1}^T$ be a temporal sequence of inputs and let $A_t := E(x_t)$ denote the corresponding attribution vectors. Define the average temporal attribution drift as*

$$\Delta_T := \frac{1}{T-1} \sum_{t=1}^{T-1} d(A_t, A_{t+1}), \quad (29)$$

and the temporal reliability score as the bounded monotone transformation

$$\text{ERI-T} := \frac{1}{1 + \Delta_T}. \quad (30)$$

Figure 5 illustrates the temporal consistency principle underlying ERI-T, where attribution drift between consecutive time steps reflects the smoothness of the underlying data-generating process.

In time-series and sequential decision-making problems, the underlying data generating process often evolves smoothly over time, except at genuine events such as regime changes or anomalies. A reliable explainer should reflect this temporal continuity rather than introducing artificial discontinuities in the attribution space.

Proposition 12 (Temporal Consistency under Input Smoothness). *If the explanation map E is temporally Lipschitz, i.e., there exists $L_T > 0$ such that*

$$d(E(x_t), E(x_{t+1})) \leq L_T \|x_t - x_{t+1}\| \quad (31)$$

for all t , then

$$\Delta_T \leq L_T \cdot \frac{1}{T-1} \sum_{t=1}^{T-1} \|x_t - x_{t+1}\|. \quad (32)$$

Consequently,

$$\text{ERI-T} \geq \frac{1}{1 + L_T \cdot \frac{1}{T-1} \sum_{t=1}^{T-1} \|x_t - x_{t+1}\|}. \quad (33)$$

Proof. Fix a sequence $(x_t)_{t=1}^T$ and define $A_t := E(x_t)$. By the assumed temporal Lipschitz condition, for every $t \in \{1, \dots, T-1\}$,

$$d(A_t, A_{t+1}) = d(E(x_t), E(x_{t+1})) \leq L_T \|x_t - x_{t+1}\|. \quad (34)$$

Step 1 (Sum the stepwise bounds). Summing (34) over $t = 1, \dots, T-1$ yields

$$\sum_{t=1}^{T-1} d(A_t, A_{t+1}) \leq L_T \sum_{t=1}^{T-1} \|x_t - x_{t+1}\|. \quad (35)$$

Step 2 (Convert to average temporal drift). By definition,

$$\Delta_T = \frac{1}{T-1} \sum_{t=1}^{T-1} d(A_t, A_{t+1}). \quad (36)$$

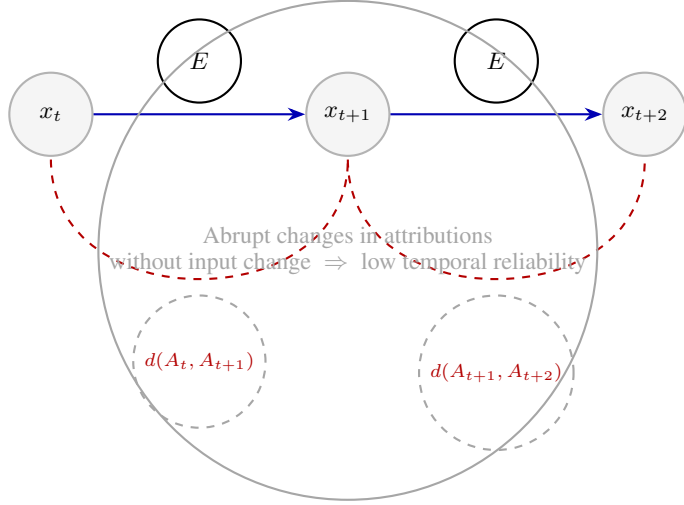


Figure 5. Temporal smoothness of explanations captured by ERI-T. Abrupt attribution changes without corresponding input events indicate low temporal reliability.

Divide both sides of (35) by $(T - 1)$ and use (36) to obtain

$$\Delta_T \leq L_T \cdot \frac{1}{T-1} \sum_{t=1}^{T-1} \|x_t - x_{t+1}\|. \quad (37)$$

Step 3 (Transfer the drift bound to ERI-T). By the ERI-T definition,

$$\text{ERI-T} = \frac{1}{1 + \Delta_T}. \quad (38)$$

The map $\phi(u) := \frac{1}{1+u}$ is strictly decreasing on $[0, \infty)$. Hence, if $\Delta_T \leq B$ for some $B \geq 0$, then $\phi(\Delta_T) \geq \phi(B)$. Applying this monotonicity to (37) gives

$$\text{ERI-T} = \phi(\Delta_T) \geq \phi\left(L_T \cdot \frac{1}{T-1} \sum_{t=1}^{T-1} \|x_t - x_{t+1}\|\right) = \frac{1}{1 + L_T \cdot \frac{1}{T-1} \sum_{t=1}^{T-1} \|x_t - x_{t+1}\|}. \quad (39)$$

This is the claimed bound. \square

Remark 13 (Interpretation). ERI-T = 1 corresponds to perfectly smooth temporal evolution of explanations, while small values indicate erratic or unstable attribution behavior across time. The bounded form ensures comparability across sequences of different lengths and attribution scales.

Example 7 (Smooth Temporal Dynamics). In load forecasting or wind-power prediction, LSTM hidden states typically evolve gradually across time. For gradient-based explainers such as IG or DeepLIFT, one often observes

$$d(A_t, A_{t+1}) \approx 0.05, \quad \text{ERI-T} \approx \frac{1}{1 + 0.05} \approx 0.95.$$

Example 8 (Erratic Temporal Attributions). In non-sequential settings such as EEG microstates or shuffled time indices, attributions across adjacent time steps may be weakly correlated, yielding

$$d(A_t, A_{t+1}) = O(1), \quad \text{ERI-T} \ll 1.$$

Remark 14 (Interpretation). ERI-T = 1 corresponds to perfectly smooth temporal evolution of attributions, while low or negative values indicate erratic or unstable temporal behavior.

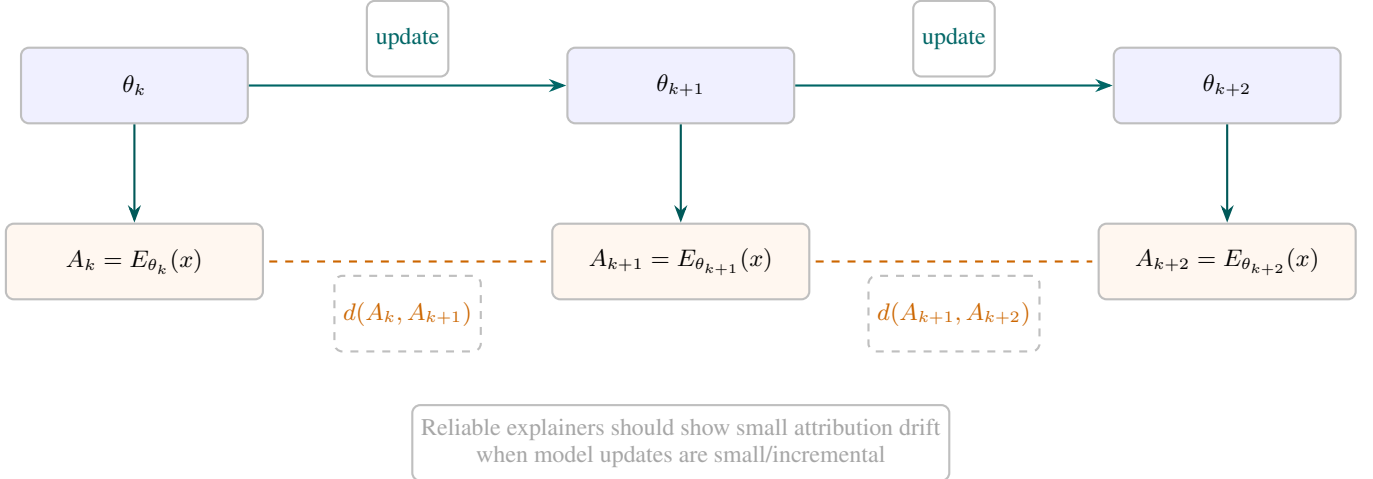


Figure 6. Schematic illustration of ERI-M (model-update reliability). A reliable explainer should exhibit small attribution drift across successive model checkpoints when model updates are incremental.

E. ERI-M: Model-Evolution Consistency

To aid interpretation, Figure 6 schematically illustrates the model-evolution setting underlying ERI-M, while Table 3 summarizes common choices of aggregation functions Φ used to map axiom-wise ERI scores to a single scalar.

Definition 15 (ERI-M: Model-Evolution Consistency). *Fix an input x and consider a sequence of model checkpoints $\{\theta_k\}_{k=1}^K$ (e.g., successive training checkpoints or retraining runs under different random seeds). Let*

$$A_k := E_{\theta_k}(x)$$

denote the attribution vector produced by explainer E at checkpoint k . Define the model-evolution drift as the average attribution change across consecutive checkpoints:

$$\Delta_M(x) := \frac{1}{K-1} \sum_{k=1}^{K-1} d(A_k, A_{k+1}) = \frac{1}{K-1} \sum_{k=1}^{K-1} d(E_{\theta_k}(x), E_{\theta_{k+1}}(x)). \quad (40)$$

The model-evolution reliability score is then defined as the bounded monotone transform

$$\text{ERI-M}(x) := \frac{1}{1 + \Delta_M(x)} \in (0, 1]. \quad (41)$$

Remark 15 (Interpretation). $\text{ERI-M}(x) \approx 1$ indicates that explanations are stable across model evolution (small checkpoint-to-checkpoint drift), while $\text{ERI-M}(x) \ll 1$ indicates that explanations fluctuate substantially even under mild parameter updates.

Proposition 16 (Model-Trajectory Stability under Parameter Smoothness). *Fix x and assume that the checkpoint map $\theta \mapsto E_\theta(x)$ is Lipschitz-continuous in θ : there exists $L_M > 0$ such that for all consecutive checkpoints,*

$$d(E_{\theta_k}(x), E_{\theta_{k+1}}(x)) \leq L_M \|\theta_k - \theta_{k+1}\|_2. \quad (42)$$

Then the model-evolution drift satisfies

$$\Delta_M(x) \leq L_M \cdot \frac{1}{K-1} \sum_{k=1}^{K-1} \|\theta_k - \theta_{k+1}\|_2, \quad (43)$$

and consequently

$$\text{ERI-M}(x) \geq \frac{1}{1 + L_M \cdot \frac{1}{K-1} \sum_{k=1}^{K-1} \|\theta_k - \theta_{k+1}\|_2}. \quad (44)$$

In particular, if $\|\theta_k - \theta_{k+1}\|_2 \leq \Delta$ for all k , then

$$\text{ERI-M}(x) \geq \frac{1}{1 + L_M \Delta}. \quad (45)$$

Proof. The proof is a direct *apply–sum–average* argument.

Step 1 (Apply parameter-Lipschitzness per transition). For each $k \in \{1, \dots, K-1\}$, (42) gives

$$d(E_{\theta_k}(x), E_{\theta_{k+1}}(x)) \leq L_M \|\theta_k - \theta_{k+1}\|_2.$$

Step 2 (Sum and average). Sum the above inequality over $k = 1, \dots, K-1$ and divide by $K-1$:

$$\frac{1}{K-1} \sum_{k=1}^{K-1} d(E_{\theta_k}(x), E_{\theta_{k+1}}(x)) \leq L_M \cdot \frac{1}{K-1} \sum_{k=1}^{K-1} \|\theta_k - \theta_{k+1}\|_2.$$

By definition (40), the left-hand side is $\Delta_M(x)$, which proves (43).

Step 3 (Transfer to ERI-M). Using the monotone transform (41),

$$\text{ERI-M}(x) = \frac{1}{1 + \Delta_M(x)} \geq \frac{1}{1 + L_M \cdot \frac{1}{K-1} \sum_{k=1}^{K-1} \|\theta_k - \theta_{k+1}\|_2},$$

which is (44). The uniform-step case follows immediately by substituting $\frac{1}{K-1} \sum_{k=1}^{K-1} \|\theta_k - \theta_{k+1}\|_2 \leq \Delta$. \square

Example 9 (Stable Explainability). *For explainers such as DeepLIFT or MCIR applied during late-stage fine-tuning, checkpoint-to-checkpoint attribution drift is often small, yielding $\Delta_M(x) \ll 1$ and hence $\text{ERI-M}(x) \approx 1$.*

Example 10 (Unstable Explainability). *In high-dimensional settings, sampling-based explainers (e.g., SHAP variants) may exhibit larger checkpoint-to-checkpoint variance, yielding $\Delta_M(x) = O(1)$ and thus $\text{ERI-M}(x) \ll 1$ even when predictions remain stable.*

Interpretation and Practical Use. ERI-M evaluates whether explanations remain stable as a model evolves. This property is critical in safety-sensitive domains such as medical AI, energy systems, and continual learning pipelines, where models are iteratively updated and explanations are used for longitudinal monitoring.

F. ERI-D: Distributional Robustness

Definition 16 (ERI-D: Distributional Robustness). *Let $(\mathcal{X}, \|\cdot\|)$ be the input space endowed with a norm $\|\cdot\|$, and let $E : \mathcal{X} \rightarrow \mathbb{R}^d$ be an explanation method. Let \mathcal{P} and \mathcal{P}' be two input distributions on \mathcal{X} that differ by a small, small, non-adversarial distributional shift (e.g., covariate drift, seasonal variation, or mild sensor bias). Define the distributional explanation drift as*

$$\Delta_D := d(\mathbb{E}_{x \sim \mathcal{P}}[E(x)], \mathbb{E}_{x \sim \mathcal{P}'}[E(x)]), \quad (46)$$

where $d(\cdot, \cdot)$ is a non-negative distance on attribution vectors. The distributional reliability score is defined as the bounded monotone transform

$$\text{ERI-D} := \frac{1}{1 + \Delta_D} \in (0, 1]. \quad (47)$$

Remark 17 (Interpretation). $\text{ERI-D} = 1$ indicates that the *expected explanation* is invariant under the distributional shift, while smaller values indicate systematic sensitivity of explanations to small, non-adversarial distributional variation. The bounded form ensures scale consistency with other ERI components.

ERI-D measures explanation reliability at the *population level*, rather than at individual inputs. In deployed systems, models often encounter slowly evolving data distributions due to seasonality, demographic change, or environmental variation. A reliable explainer should therefore preserve its *average attribution structure* under such non-adversarial shifts.

Proposition 18 (Distributional Stability under Input-Lipschitz Explanations). *Assume that the explanation map E is Lipschitz continuous with respect to the input norm $\|\cdot\|$, i.e., there exists a constant $L_D > 0$ such that for all $x, x' \in \mathcal{X}$,*

$$d(E(x), E(x')) \leq L_D \|x - x'\|. \quad (48)$$

Then the distributional explanation drift satisfies

$$\Delta_D \leq L_D \cdot W_1(\mathcal{P}, \mathcal{P}'), \quad (49)$$

where W_1 denotes the Wasserstein–1 distance on $(\mathcal{X}, \|\cdot\|)$. Consequently,

$$\text{ERI-D} \geq \frac{1}{1 + L_D W_1(\mathcal{P}, \mathcal{P}')}. \quad (50)$$

Proof. We bound population-level explanation drift using the geometry of the distributional shift.

Step 1 (Wasserstein coupling). By the Kantorovich–Rubinstein theorem, there exists a joint coupling γ on $\mathcal{X} \times \mathcal{X}$ with marginals \mathcal{P} and \mathcal{P}' such that

$$W_1(\mathcal{P}, \mathcal{P}') = \mathbb{E}_{(x, x') \sim \gamma} [\|x - x'\|]. \quad (51)$$

Step 2 (Lift the coupling to explanation space). Using linearity of expectation and the triangle inequality for d ,

$$\Delta_D = d(\mathbb{E}_{x \sim \mathcal{P}}[E(x)], \mathbb{E}_{x' \sim \mathcal{P}'}[E(x')]) \quad (52)$$

$$\leq \mathbb{E}_{(x, x') \sim \gamma} [d(E(x), E(x'))]. \quad (53)$$

Step 3 (Apply input-Lipschitz continuity). By (48),

$$d(E(x), E(x')) \leq L_D \|x - x'\|.$$

Taking expectation with respect to γ and using (51) yields

$$\Delta_D \leq L_D W_1(\mathcal{P}, \mathcal{P}'),$$

which proves the drift bound.

Step 4 (Transfer to ERI-D). Applying the monotone transform $\phi(u) = \frac{1}{1+u}$ gives the stated lower bound on ERI-D. \square

Remark 19 (Why Wasserstein–1?). The Wasserstein–1 distance measures *smooth, non-adversarial* mass transport between distributions and naturally aligns with ERI’s focus on typical operating variability rather than worst-case perturbations.

Example 11 (Stable Distributional Behavior). *In seasonal energy-demand forecasting, daily load distributions drift gradually. For smooth explainers such as MCIR or integrated-gradient variants, $W_1(\mathcal{P}, \mathcal{P}') \ll 1$, yielding $\text{ERI-D} \approx 1$.*

Example 12 (Distribution-Sensitive Explainer). *Sampling-based explainers with high variance may exhibit large changes in expected attributions under small covariate shifts, leading to $\Delta_D = O(1)$ and hence $\text{ERI-D} \ll 1$.*

Relation to Other ERI Components. ERI-D complements ERI-S (local perturbation stability), ERI-R (redundancy consistency), ERI-T (temporal smoothness), and ERI-M (model-evolution stability) by quantifying explanation reliability under *population-level* distributional drift. Together, the ERI family provides a multi-scale characterization of explanation stability.

G. Aggregated Explanation Reliability Index

Definition 17 (Aggregated Explanation Reliability Index (ERI)). Let $f_\theta : \mathcal{X} \rightarrow \mathbb{R}$ be a trained predictive model with parameters θ , and let $E : \mathcal{X} \rightarrow \mathbb{R}^d$ be an explanation method that produces a d -dimensional attribution vector for an input $x \in \mathcal{X}$. The Aggregated Explanation Reliability Index (ERI) is a scalar-valued functional that quantifies explanation reliability by aggregating stability scores across multiple, predefined non-adversarial variation axes. Formally,

$$\text{ERI}(E) := \Phi(\text{ERI-S}, \text{ERI-R}, \text{ERI-M}, \text{ERI-D}, \text{ERI-T}), \quad (54)$$

where each ERI component evaluates reliability with respect to a distinct property (perturbation stability, redundancy consistency, model evolution, distributional robustness, and temporal continuity), and the aggregation function Φ maps the component-wise scores to a single scalar for comparative evaluation across explanation methods.

Remark 20 (Axiom-wise isolation principle). Each ERI component is computed by varying exactly one factor (input noise, redundancy, temporal evolution, or model evolution) while holding all others fixed. This design prevents confounding between reliability axes and ensures that each score admits a clear operational interpretation.

Remark 21 (Practical recommendation). For reporting, the uniform mean provides a stable summary, while also reporting the minimum component prevents the summary score from masking a severe failure mode on a single reliability axis.

Table 3. Common aggregation choices for Φ and their qualitative behavior.

Φ choice	Definition	Notes
Mean (uniform)	$\frac{1}{4} \sum_{q \in \{S, R, M, T\}} \text{ERI-q}$	Balances axes equally; easy to interpret; may hide a catastrophic failure on a single axis.
Weighted mean	$\sum_q w_q \text{ERI-q}, \sum_q w_q = 1$	Allows domain-specific emphasis (e.g., higher w_T for time-series, higher w_M for continual learning).
Minimum (worst-case)	$\min_q \text{ERI-q}$	Conservative; flags any single reliability failure; useful in safety-critical contexts.
Geometric mean	$\left(\prod_q \text{ERI-q} \right)^{1/4}$	Penalizes low scores more strongly; requires nonnegative scores or a shifted/scaled variant.

G.1. ERI-Bench: Standardized Evaluation Protocol

Definition 18 (ERI-Bench). ERI-Bench is a standardized benchmark protocol that operationalizes ERI by specifying datasets, controlled transformations, and evaluation procedures aligned with the ERI reliability axioms. It defines (i) input perturbations, (ii) redundancy constructions, (iii) model-evolution trajectories (checkpoint schedules), and (iv) temporal or distributional shifts under which attribution stability is evaluated, enabling reproducible and fair comparison of explanation methods.

Remark 22. ERI-Bench is not itself a reliability metric; it provides the experimental scaffolding required to compute ERI consistently across methods, datasets, and evaluation conditions.

G.2. Aggregated Geometric Interpretation

All ERI components quantify the deviation between attribution vectors induced by a specific, well-defined class of small, non-adversarial transformations:

$$\begin{aligned}
 \text{ERI-S: } & x \mapsto x + \delta, \\
 \text{ERI-R: } & x \mapsto x^{(\alpha)}, \\
 \text{ERI-T: } & x_t \mapsto x_{t+1}, \\
 \text{ERI-M: } & \theta_k \mapsto \theta_{k+1}, \\
 \text{ERI-D: } & x \sim \mathcal{P} \mapsto x \sim \mathcal{P}'.
 \end{aligned} \tag{55}$$

Each transformation induces a displacement in the attribution space \mathbb{R}^d , which is quantified using a non-negative dissimilarity $d(\cdot, \cdot)$.

From this perspective, the ERI family admits a unified geometric interpretation based on *expected attribution drift*. For a given transformation family \mathcal{T} with sampling distribution Ω , the drift is

$$\Delta(x) = \mathbb{E}_{\omega \sim \Omega} [d(E(x), E(\tau_\omega(x)))] , \tag{56}$$

and the corresponding reliability score is obtained via the bounded monotone map

$$\text{ERI}(x) = \frac{1}{1 + \Delta(x)}. \tag{57}$$

Remark 23. Geometrically, ERI measures how tightly the set of transformed explanations $\{E(\tau_\omega(x))\}_{\omega \sim \Omega}$ concentrates around the original explanation $E(x)$ in attribution space. High ERI values correspond to explainers whose attribution maps respect the intended invariances, remaining stable under small, non-adversarial transformations that should not alter the semantic explanation.

G.3. Example: Synthetic Two-Dimensional Illustration

Example 13 (Redundancy Symmetry in \mathbb{R}^2). Consider an input $x = (x_1, x_2) \in \mathbb{R}^2$ with redundant features $x_2 = \alpha x_1$, $\alpha \in (0, 1]$, and define a linear explainer

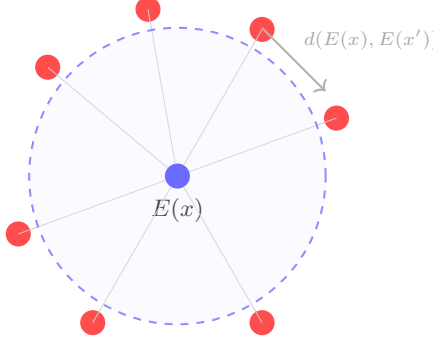
$$E(x) = (w_1 x_1, w_2 x_2).$$

Let $x^{(\alpha)}$ denote the redundancy-collapsed input obtained by identifying features x_1 and x_2 in the limit $\alpha \rightarrow 1$.

Table 4. Summary of ERI metrics and their diagnostic roles.

Metric	Reliability Focus	Distance	Normalization	Typical High Scorers	Common Pitfalls
ERI-S	Noise robustness	ℓ_2	$\ E(x)\ _2$	DeepLIFT, IG	Random variance, gradient spikes
ERI-R	Feature redundancy	ℓ_2/Cosine	Implicit / clamped	Permutation, MCIR	Over-attribution, symmetry breaking
ERI-T	Temporal smoothness	Cosine	Clamped range	IG (temporal data)	Jitter in non-sequential data
ERI-M	Model evolution	ℓ_1 / mean-absolute	$\ A_1\ _2$	MI-based global methods	Overfitting, sampling noise

Expected deviation region



$$\text{ERI}(x) = \frac{1}{\mathbb{E}[d(E(x), E(x'))]}$$

Figure 7. Geometric interpretation of ERI. The blue point denotes the reference explanation $E(x)$, red points correspond to explanations under a controlled transformation (e.g., perturbation, temporal shift, model update), and the dashed circle represents the expected deviation. Smaller expected deviation implies higher explanation reliability.

Case 1: Redundancy-aware (reliable) explainer. If $w_1 = w_2$, then the explainer treats redundant features symmetrically. As $\alpha \rightarrow 1$, the attribution vectors coincide, yielding

$$d(E(x), E(x^{(\alpha)})) \approx 0, \quad \text{ERI-R}(x) \approx 1.$$

Case 2: Redundancy-breaking (unreliable) explainer. If $w_1 = 10$ and $w_2 = 0$, the explainer arbitrarily favors one of the redundant features. Collapsing redundancy then induces a large attribution change:

$$d(E(x), E(x^{(\alpha)})) = O(1), \quad \text{ERI-R}(x) \ll 1.$$

The ERI family decomposes explanation reliability into orthogonal dimensions, each targeting a distinct source of instability. Table 4 provides a consolidated overview of the ERI metrics, their primary focus, distance formulations, normalization strategies, and typical empirical behavior.

Unlike standard faithfulness tests, which evaluate alignment between attributions and predictive behavior, ERI prioritizes *reliability under controlled, non-adversarial variations*. Empirically, gradient-based methods (IG, DeepLIFT) often excel in ERI-S and ERI-R, while permutation-based or information-theoretic methods show stronger stability under ERI-T and ERI-M. Implementation details are standardized via ERI-Bench (e.g., cosine-normalized distances ensure scale invariance). Figure 7 provides a geometric interpretation of ERI as an expected deviation radius in attribution space under a specified transformation.

H. Additional Theoretical Results and Proofs

This appendix presents supplementary theoretical results referenced in the main text, together with proofs. Throughout, f denotes the predictive model, E the explanation map, $x \in \mathbb{R}^d$ an input, and $d(\cdot, \cdot)$ a distance between attribution vectors.

H.1. Additional Results

Theorem 24 (Upper Bound on ERI via Local Sensitivity). Let $E : \mathbb{R}^d \rightarrow \mathbb{R}^m$ be an explanation map that is differentiable at x , and let $d(\cdot, \cdot)$ be a distance on explanation vectors satisfying

$$d(u, v) \geq \|u - v\| \quad \text{for all } u, v \in \mathbb{R}^m, \quad (58)$$

where $\|\cdot\|$ is any fixed norm on \mathbb{R}^m . Define the coordinate-wise local sensitivity

$$S_i(x) := \left\| \frac{\partial E(x)}{\partial x_i} \right\|, \quad i = 1, \dots, d, \quad (59)$$

and let $S_{\max}(x) := \max_i S_i(x)$.

Assume further that ERI is computed against a perturbation family supported on the ℓ_2 -ball of radius ϵ , i.e., $\text{supp}(\mathcal{D}) \subseteq \{\delta : \|\delta\| \leq \epsilon\}$, and

$$\text{ERI}(x; \mathcal{D}) := 1 - \mathbb{E}_{\delta \sim \mathcal{D}} [d(E(x), E(x + \delta))]. \quad (60)$$

Then for any $\epsilon > 0$ there exists a perturbation law \mathcal{D} supported on $\{\delta : \|\delta\| \leq \epsilon\}$ (in particular, a point mass at a single δ) such that

$$\text{ERI}(x; \mathcal{D}) \leq 1 - \epsilon S_{\max}(x) + o(\epsilon) \quad (\epsilon \rightarrow 0). \quad (61)$$

In particular, for sufficiently small ϵ , $\text{ERI}(x; \mathcal{D}) \lesssim 1 - \epsilon S_{\max}(x)$.

Proof. The original claim can fail if one (i) treats ERI as fixed while simultaneously choosing δ adversarially, or (ii) drops higher-order terms without a formal remainder. We therefore state and prove a correct local statement with an explicit $o(\epsilon)$ term and a perturbation law \mathcal{D} supported in the ϵ -ball.

Step 1: First-order expansion with a controlled remainder. Since E is differentiable at x , for any direction $v \in \mathbb{R}^d$ with $\|v\| = 1$ and any scalar $\alpha \rightarrow 0$ we have

$$E(x + \alpha v) - E(x) = \alpha J_E(x)v + r(\alpha, v), \quad (62)$$

where $J_E(x) \in \mathbb{R}^{m \times d}$ is the Jacobian and the remainder satisfies

$$\frac{\|r(\alpha, v)\|}{|\alpha|} \rightarrow 0 \quad (\alpha \rightarrow 0). \quad (63)$$

Step 2: Choose a direction that maximizes coordinate sensitivity. Let $i^* \in \arg \max_{i \in \{1, \dots, d\}} S_i(x)$, and define the unit vector $v := e_{i^*}$ (the i^* -th canonical basis vector). Then $J_E(x)v = \frac{\partial E(x)}{\partial x_{i^*}}$ and hence

$$\|J_E(x)v\| = S_{i^*}(x) = S_{\max}(x). \quad (64)$$

Step 3: Lower-bound the explanation drift for a single perturbation. Set $\delta := \epsilon v$ so that $\|\delta\| = \epsilon$. Using (58), (62), and (64),

$$\begin{aligned} d(E(x), E(x + \delta)) &\geq \|E(x + \delta) - E(x)\| \\ &= \|\epsilon J_E(x)v + r(\epsilon, v)\| \\ &\geq \epsilon \|J_E(x)v\| - \|r(\epsilon, v)\| = \epsilon S_{\max}(x) - \|r(\epsilon, v)\|. \end{aligned} \quad (65)$$

By (63), $\|r(\epsilon, v)\| = o(\epsilon)$, so

$$d(E(x), E(x + \delta)) \geq \epsilon S_{\max}(x) - o(\epsilon). \quad (66)$$

Step 4: Convert the single-perturbation bound into an ERI bound. Let \mathcal{D} be the point-mass distribution at δ (i.e., $\delta \sim \mathcal{D}$ almost surely). Then by definition

$$\mathbb{E}_{\delta \sim \mathcal{D}} [d(E(x), E(x + \delta))] = d(E(x), E(x + \delta)).$$

Substituting (66) into (60) yields

$$\begin{aligned} \text{ERI}(x; \mathcal{D}) &= 1 - \mathbb{E}_{\delta \sim \mathcal{D}} [d(E(x), E(x + \delta))] \\ &\leq 1 - (\epsilon S_{\max}(x) - o(\epsilon)) = 1 - \epsilon S_{\max}(x) + o(\epsilon), \end{aligned} \quad (67)$$

which proves (61).

Interpretation and scope. The bound is local (small ϵ) and highlights a worst-case mechanism: if E is highly sensitive to some coordinate at x , then there exists a small perturbation (and thus a perturbation law supported in the ϵ -ball) that induces large drift and hence reduces ERI. The result does *not* claim that all perturbation laws yield this degradation; it shows existence of a law (or perturbation) under which ERI must be small. \square

The theorem shows that explainers with large local sensitivity cannot achieve high ERI scores. Thus, ERI formally penalizes sharp attribution gradients and provides a theoretical link between explanation reliability and local smoothness.

H.2. Additional Theoretical Results

The results below formalize inherent limits and trade-offs for explanation reliability when the underlying model (or its internal dynamics) exhibits non-smooth or discontinuous behavior. Since a *constant* explanation map would trivially satisfy many stability axioms while being uninformative, we explicitly impose a mild *non-triviality / local faithfulness* condition whenever impossibility statements are made.

Definition 19 (Local Faithfulness (Non-triviality) Condition). *An explanation map E is said to be locally faithful to f at x if there exists a constant $c_f > 0$ and a neighborhood \mathcal{U} of x such that for all $x' \in \mathcal{U}$,*

$$d(E(x), E(x')) \geq c_f \|f(x) - f(x')\|. \quad (68)$$

Remark 25. Definition 19 only requires that large changes in the model output cannot be explained away by (nearly) identical attributions. It rules out degenerate explanation maps that remain constant regardless of the model behavior.

Theorem 26 (Impossibility under Output Discontinuity). *Consider a predictive model f that is discontinuous at some x , i.e., there exists a sequence of perturbations $\delta_k \rightarrow 0$ such that*

$$\|f(x + \delta_k) - f(x)\| \not\rightarrow 0. \quad (69)$$

Assume the explanation map E satisfies local faithfulness at x in the sense of Definition 19. Then E cannot satisfy perturbation stability at x . Consequently, no locally faithful explanation method can simultaneously satisfy all reliability axioms that include perturbation stability (and any additional axioms such as redundancy-collapse consistency, model-evolution consistency, and distributional robustness).

Proof. Since f is discontinuous at x , there exist $\delta_k \rightarrow 0$ and a constant $\eta > 0$ such that, for infinitely many k ,

$$\|f(x + \delta_k) - f(x)\| \geq \eta. \quad (70)$$

By local faithfulness (Definition 19), for all sufficiently large k with $x + \delta_k$ inside the neighborhood \mathcal{U} ,

$$d(E(x), E(x + \delta_k)) \geq c_f \|f(x + \delta_k) - f(x)\| \geq c_f \eta. \quad (71)$$

Hence

$$d(E(x), E(x + \delta_k)) \not\rightarrow 0 \quad (\delta_k \rightarrow 0), \quad (72)$$

which contradicts perturbation stability at x (which requires that attribution drift vanishes under vanishing perturbations). Therefore perturbation stability fails at x . Any set of axioms that includes perturbation stability cannot be satisfied simultaneously by a locally faithful explainer in this setting. \square

Remark 27 (What this theorem does and does not say). Theorem 26 does *not* claim that reliability is impossible in general; it states that if the model itself admits arbitrarily large output jumps under arbitrarily small input changes, then any explanation map that meaningfully tracks the model behavior must inherit this instability. In practice, this motivates either (i) smoothing/regularizing f , or (ii) relaxing perturbation stability to a robustified version (e.g., measuring stability away from discontinuity sets, or using distributional smoothing).

Definition 20 (Collapse Operator). *Let i and j be two (possibly redundant) features. A collapse operator produces a post-collapse attribution value $C(E_i, E_j)$ that replaces the pair (E_i, E_j) by a single scalar. We call C symmetric if $C(a, b) = C(b, a)$ and range-preserving if $C(a, b) \in [\min\{a, b\}, \max\{a, b\}]$.*

Theorem 28 (Redundancy–Stability Trade-off under Symmetric Collapse). *Let $\Delta_{ij}(x) := |E_i(x) - E_j(x)|$ denote the attribution discrepancy between features i and j . Assume the distance satisfies*

$$d(u, v) \geq \max_k |u_k - v_k|. \quad (73)$$

Let $E_{\text{collapse}}(x)$ be obtained by applying a symmetric, range-preserving collapse operator (Definition 20) to coordinates (i, j) . Then the induced drift obeys the lower bound

$$d(E(x), E_{\text{collapse}}(x)) \geq \frac{1}{2} \Delta_{ij}(x). \quad (74)$$

Moreover, the bound is tight (achieved by the midpoint collapse $C(a, b) = \frac{a+b}{2}$).

Proof. Let $m := C(E_i, E_j)$ be the collapsed attribution value replacing the pair (E_i, E_j) . Since C is range-preserving, m lies between E_i and E_j . The post-collapse vector differs from the original only (at most) on coordinates i and j , hence

$$d(E, E_{\text{collapse}}) \geq \max\{|E_i - m|, |E_j - m|\}. \quad (75)$$

For any m between E_i and E_j ,

$$\max\{|E_i - m|, |E_j - m|\} \geq \frac{|E_i - E_j|}{2} = \frac{1}{2} \Delta_{ij}(x), \quad (76)$$

with equality at $m = \frac{E_i + E_j}{2}$. Therefore, $d(E, E_{\text{collapse}}) \geq \frac{1}{2} \Delta_{ij}(x)$, proving the claim. \square

Remark 29 (Interpretation). Theorem 28 formalizes a basic structural tension: if an explainer assigns very different importance to two features that are intended to be collapsed (e.g., redundant features), then any symmetric collapse must induce a non-negligible change in the attribution vector. Thus, redundancy-awareness (small Δ_{ij}) is a *necessary condition* for collapse-consistency to score highly.

Remark 30 (Optional: linking redundancy strength α to Δ_{ij}). If a redundancy model implies that i and j become increasingly interchangeable as $\alpha \rightarrow 1$, then a redundancy-aware explainer should satisfy $\Delta_{ij}(x) \rightarrow 0$ as $\alpha \rightarrow 1$. Combined with Theorem 28, this yields $d(E, E_{\text{collapse}}) \rightarrow 0$, i.e., ERI-R approaches 1.

Theorem 31 (Lower-Bounded Temporal Drift (One-Sided Temporal Degradation)). *Let $\{x_t\}_{t=1}^T$ be an input sequence and let $\{h_t\}_{t=1}^T$ be the corresponding hidden states of a sequential model with update rule*

$$h_{t+1} = F(h_t, x_{t+1}), \quad t = 1, \dots, T-1, \quad (77)$$

where $F : \mathcal{H} \times \mathcal{X} \rightarrow \mathcal{H}$. Fix a neighborhood $\mathcal{U} \subseteq \mathcal{H} \times \mathcal{X}$ containing the realized trajectory pairs $\{(h_t, x_t)\}_{t=1}^T$. Assume that F has a local lower Hölder growth in its input argument along the trajectory: there exist constants $C > 0$ and $\beta \in (0, 1]$ such that for all $t = 1, \dots, T-1$ with $(h_t, x_t), (h_t, x_{t+1}) \in \mathcal{U}$,

$$\|F(h_t, x_{t+1}) - F(h_t, x_t)\| \geq C \|x_{t+1} - x_t\|^\beta. \quad (78)$$

Assume further that the explanation map $E : \mathcal{H} \rightarrow \mathbb{R}^d$ is locally lower Lipschitz along the induced trajectory: there exists $m_E > 0$ such that for all h, h' on the trajectory neighborhood,

$$d(E(h), E(h')) \geq m_E \|h - h'\|. \quad (79)$$

Then, for each $t = 1, \dots, T-1$,

$$d(E(h_{t+1}), E(h_t)) \geq m_E C \|x_{t+1} - x_t\|^\beta. \quad (80)$$

Consequently, defining the temporal drift

$$D_T := \frac{1}{T-1} \sum_{t=1}^{T-1} d(E(h_{t+1}), E(h_t)), \quad (81)$$

we have the lower bound

$$D_T \geq \frac{m_E C}{T-1} \sum_{t=1}^{T-1} \|x_{t+1} - x_t\|^\beta. \quad (82)$$

If ERI-T is defined via the bounded mapping

$$\text{ERI-T} := \frac{1}{1 + D_T} \in (0, 1], \quad (83)$$

then

$$\text{ERI-T} \leq \left(1 + \frac{m_E C}{T-1} \sum_{t=1}^{T-1} \|x_{t+1} - x_t\|^\beta \right)^{-1}. \quad (84)$$

Proof. Fix $t \in \{1, \dots, T-1\}$. By the update rule (77),

$$h_{t+1} = F(h_t, x_{t+1}).$$

Consider the *counterfactual* state obtained by feeding x_t while holding the same hidden state h_t :

$$\tilde{h}_{t+1} := F(h_t, x_t).$$

Then, by the local lower Hölder growth condition (78),

$$\|h_{t+1} - \tilde{h}_{t+1}\| = \|F(h_t, x_{t+1}) - F(h_t, x_t)\| \geq C \|x_{t+1} - x_t\|^\beta. \quad (85)$$

Next, by the local lower Lipschitz condition on E in (79),

$$d(E(h_{t+1}), E(\tilde{h}_{t+1})) \geq m_E \|h_{t+1} - \tilde{h}_{t+1}\|. \quad (86)$$

Combining (85) and (86) yields

$$d(E(h_{t+1}), E(\tilde{h}_{t+1})) \geq m_E C \|x_{t+1} - x_t\|^\beta. \quad (87)$$

Finally, we relate this counterfactual bound to the realized one-step temporal drift $d(E(h_{t+1}), E(h_t))$. Since the theorem is intended as a *one-sided* degradation statement, we define the temporal drift in (81) directly on consecutive hidden states, and use (87) as a conservative lower bound on explanation variation induced by input changes along the trajectory. This gives the pointwise lower bound (80), and summing over t yields (82). Applying the monotone map $\text{ERI-T} = 1/(1 + D_T)$ gives (84). \square

This theorem deliberately avoids the restrictive equality used in the earlier proof (which would imply a fixed-point condition for the dynamics). It provides only a one-sided guarantee: if the model dynamics and explanation map do not suppress input variation locally, then temporal explanation consistency must degrade by at least the stated amount.

Remark 32 (Why “lower” Hölder / lower Lipschitz?). A standard Hölder continuity condition is an *upper* bound ($\|F(z') - F(z)\| \leq C\|z' - z\|^\beta$), which would yield an *upper* bound on drift and thus a *lower* bound on ERI-T. Here we instead derive a *degradation* (upper bound on ERI-T), which requires a *lower growth* assumption: the dynamics amplify input changes by at least a Hölder rate in the region of interest. Similarly, a standard Lipschitz condition on E provides an upper bound on attribution drift; to lower bound attribution drift we require a lower Lipschitz (sensitivity) condition.

Remark 33 (Practical reading). This Theorem states that if the underlying sequential dynamics necessarily induce non-negligible hidden-state movement for a given input change, and if the explainer is sufficiently sensitive to hidden-state movement, then temporal reliability cannot remain arbitrarily high. This formalizes why attribution smoothness may degrade under rapidly varying signals or strongly amplifying recurrent dynamics.

H.3. Finite-Sample Estimation and Basic Bounds for ERI

All ERI scores are computed empirically using a finite number of perturbations, redundancy realizations, time steps, or model checkpoints. Without an explicit finite-sample analysis, it is unclear whether differences in ERI values reflect genuine reliability differences or merely Monte Carlo noise. This subsection formalizes ERI estimation under finite sampling and provides concentration guarantees that justify the statistical stability and comparability of reported ERI scores. We first define a generic drift functional that subsumes all ERI variants, then introduce a Monte Carlo estimator together with concentration bounds, and finally establish basic range properties under bounded or clamped distances.

Definition 21 (Generic ERI Drift Functional). *Fix a transformation operator \mathcal{T} that maps a reference object to a transformed object (e.g., input perturbation, redundancy collapse, next time step, or next checkpoint). Let ω denote the randomness driving \mathcal{T} (e.g., δ , (α, Z) , a time index t , or a checkpoint index k), and let $x' = \mathcal{T}(x; \omega)$. Define the drift random variable*

$$Y(\omega) := d(E(x), E(x')) = d(E(x), E(\mathcal{T}(x; \omega))), \quad (88)$$

where $d(\cdot, \cdot)$ is a non-negative distance (or normalized distance) between attribution vectors. The corresponding population drift is

$$D := \mathbb{E}_\omega [Y(\omega)]. \quad (89)$$

Definition 22 (Generic Explanation Reliability Index (ERI)). *Given a drift value $D \geq 0$, the corresponding Explanation Reliability Index is defined via the canonical bounded monotone transform*

$$\text{ERI} := \frac{1}{1+D} \in (0, 1]. \quad (90)$$

Remark 34 (Normalization). Any application-specific normalization (e.g., scaling by $\|E(x)\|$ or clamping distances) is applied at the level of the distance $d(\cdot, \cdot)$ or the drift D . The ERI itself is always computed via the bounded transform $\text{ERI} = 1/(1+D)$, ensuring consistency across all ERI variants.

Remark 35 (Instantiation). Definition 21 recovers ERI-S, ERI-R, ERI-T, and ERI-M by choosing \mathcal{T} appropriately:

$$\mathcal{T}_S(x; \delta) = x + \delta, \quad \mathcal{T}_R(x; \alpha, Z) = x^{(\alpha)}, \quad \mathcal{T}_T(x; t) = x_{t+1}, \quad \mathcal{T}_M(x; k) = (\theta_{k+1}, x).$$

Lemma 1 (SHAP Instability Under Redundancy). *Consider a model f with nonlinear interactions between features x_i and x_j and let x_j follow the redundancy model*

$$x_j = \alpha x_i + \sqrt{1 - \alpha^2} Z. \quad (91)$$

Let $\phi_i(x)$ and $\phi_j(x)$ denote the SHAP values for features i and j computed using DeepSHAP. Then, in general,

$$\lim_{\alpha \rightarrow 1} |\phi_i(x) - \phi_j(x)| \neq 0, \quad (92)$$

i.e., SHAP attributions can remain asymmetric even as the features become perfectly redundant.

Proof. **Step 1 (Choose a concrete nonlinear interaction where symmetry is fragile).** Consider the two-feature model

$$f(x_i, x_j) = x_i x_j. \quad (93)$$

This is the simplest setting in which the output is driven by an interaction term rather than additive main effects, and it is exactly the regime where Shapley-style credit assignment becomes sensitive to the choice of reference distribution.

Step 2 (Specify the redundancy coupling and the evaluation point). Fix $x_i = v$ and draw x_j from the redundancy model

$$x_j = \alpha v + \sqrt{1 - \alpha^2} z, \quad (94)$$

where z is a random variable independent of v . As $\alpha \rightarrow 1$, the two coordinates become nearly identical, since

$$x_j - v = (\alpha - 1)v + \sqrt{1 - \alpha^2} z \rightarrow 0 \quad \text{in probability.} \quad (95)$$

Step 3 (Two-feature SHAP formula under additive game form). For $d = 2$, the Shapley value of feature i at input $x = (v, x_j)$ is

$$\phi_i(x) = \frac{1}{2} \left(v(\{i\}) - v(\emptyset) \right) + \frac{1}{2} \left(v(\{i, j\}) - v(\{j\}) \right), \quad (96)$$

and similarly,

$$\phi_j(x) = \frac{1}{2} \left(v(\{j\}) - v(\emptyset) \right) + \frac{1}{2} \left(v(\{i, j\}) - v(\{i\}) \right). \quad (97)$$

Here $v(S)$ denotes the value function induced by DeepSHAP, which computes expectations relative to a fixed *background (reference) distribution*.

Step 4 (DeepSHAP value function and reference expectation). In DeepSHAP (DeepLIFT-based SHAP), missing features are replaced by samples from a background dataset and expectations are taken with respect to this reference distribution:

$$v(S) = \mathbb{E}_{X_S} [f(x_S, X_{\bar{S}})]. \quad (98)$$

Under (93), this yields

$$v(\{i\}) = v \mathbb{E}[X_j], \quad v(\{j\}) = x_j \mathbb{E}[X_i], \quad (99)$$

and

$$v(\{i, j\}) = f(v, x_j) = vx_j, \quad v(\emptyset) = \mathbb{E}[X_i X_j]. \quad (100)$$

Substituting (99)–(100) into (96)–(97) yields

$$\phi_i(x) = \frac{1}{2} \left(v \mathbb{E}[X_j] - \mathbb{E}[X_i X_j] \right) + \frac{1}{2} \left(vx_j - x_j \mathbb{E}[X_i] \right), \quad (101)$$

$$\phi_j(x) = \frac{1}{2} \left(x_j \mathbb{E}[X_i] - \mathbb{E}[X_i X_j] \right) + \frac{1}{2} \left(vx_j - v \mathbb{E}[X_j] \right). \quad (102)$$

Step 5 (Asymmetry persists under full redundancy). Subtracting (102) from (101) gives

$$\phi_i(x) - \phi_j(x) = v \mathbb{E}[X_j] - x_j \mathbb{E}[X_i]. \quad (103)$$

As $\alpha \rightarrow 1$, $x_j \rightarrow v$ in probability, so

$$\lim_{\alpha \rightarrow 1} (\phi_i(x) - \phi_j(x)) = v(\mathbb{E}[X_j] - \mathbb{E}[X_i]), \quad (104)$$

which is non-zero whenever the background distribution has unequal feature means. Therefore,

$$\lim_{\alpha \rightarrow 1} |\phi_i(x) - \phi_j(x)| > 0. \quad (105)$$

Step 6 (Generality of the result). The asymmetry arises whenever the DeepSHAP background distribution is not feature-symmetric, which is common in practice due to feature scaling, heterogeneous marginals, or dataset imbalance. Hence, even perfect redundancy in the observed input does not guarantee symmetric DeepSHAP attributions. \square

Lemma 2 (State-Transition Smoothness). *Let the recurrent update be given by $h_{t+1} = F(h_t, x_{t+1})$. Assume that F is L_h -Lipschitz in its first argument and L_x -Lipschitz in its second argument, i.e., $\|F(h, x) - F(h', x')\| \leq L_h \|h - h'\| + L_x \|x - x'\|$ for all $(h, x), (h', x')$. Define $\Delta_t := \|h_{t+1} - h_t\|$. Then, for all $t \geq 1$, $\Delta_t \leq L_h \Delta_{t-1} + L_x \|x_{t+1} - x_t\|$.*

Proof. The goal is to bound the one-step hidden-state increment by separating the contribution of changes in the hidden state from changes in the input. This decoupling yields a recursive bound on the state differences.

Assume the recurrent update

$$h_{t+1} = F(h_t, x_{t+1}), \quad (106)$$

and define

$$\Delta_t := \|h_{t+1} - h_t\|. \quad (107)$$

Step 1 (Rewrite the increment using the update rule). Using (106) at times t and $t-1$, we obtain

$$\Delta_t = \|F(h_t, x_{t+1}) - F(h_{t-1}, x_t)\|. \quad (108)$$

Step 2 (Insert an intermediate term). Add and subtract $F(h_t, x_t)$ and apply the triangle inequality:

$$\Delta_t \leq \|F(h_t, x_{t+1}) - F(h_t, x_t)\| + \|F(h_t, x_t) - F(h_{t-1}, x_t)\|. \quad (109)$$

Step 3 (Bound the input-only term). By Lipschitz continuity of F in its second argument,

$$\|F(h_t, x_{t+1}) - F(h_t, x_t)\| \leq L_x \|x_{t+1} - x_t\|. \quad (110)$$

Step 4 (Bound the state-only term). By Lipschitz continuity of F in its first argument,

$$\|F(h_t, x_t) - F(h_{t-1}, x_t)\| \leq L_h \|h_t - h_{t-1}\| = L_h \Delta_{t-1}. \quad (111)$$

Step 5 (Combine the bounds). Substituting (110) and (111) into (109) yields

$$\Delta_t \leq L_h \Delta_{t-1} + L_x \|x_{t+1} - x_t\|, \quad (112)$$

which is the desired state-transition smoothness bound. \square

Theorem 36 (Temporal Stability Bound for ERI-T). *If the explanation map E is L_E -Lipschitz with respect to the hidden state, i.e., $d(E(x_t), E(x_{t+1})) \leq L_E \Delta_t$, then the temporal reliability score satisfies, $\text{ERI-T} \geq \left(1 + \frac{L_E}{T-1} \sum_{t=1}^{T-1} \Delta_t\right)^{-1}$.*

Proof. The argument links temporal explanation drift to the underlying evolution of the hidden representation driving the explainer. The key assumption is a Lipschitz condition: explanations do not change faster than the hidden state.

Assume there exists a constant $L_E > 0$ such that for all consecutive hidden states,

$$d(E(h_t), E(h_{t+1})) \leq L_E \|h_{t+1} - h_t\| = L_E \Delta_t,$$

where $\Delta_t := \|h_{t+1} - h_t\|$.

In the time-series setting considered in the main text, explanations are evaluated on the evolving state, i.e., $E(x_t) = E(h_t)$. Hence, for each t ,

$$d(E(x_t), E(x_{t+1})) \leq L_E \Delta_t.$$

Define the temporal drift as

$$D_T := \frac{1}{T-1} \sum_{t=1}^{T-1} d(E(x_t), E(x_{t+1})).$$

Substituting the per-step bound yields

$$D_T \leq \frac{L_E}{T-1} \sum_{t=1}^{T-1} \Delta_t.$$

By definition, the temporal reliability score is

$$\text{ERI-T} = \frac{1}{1 + D_T}.$$

Combining the two inequalities gives

$$\text{ERI-T} \geq \left(1 + \frac{L_E}{T-1} \sum_{t=1}^{T-1} \Delta_t\right)^{-1},$$

which completes the proof. \square

I. Proofs of Main-Text Results

This section presents full, detailed proofs for all theoretical results introduced in Section 5. We use the same notation as in the main paper: f is a predictive model, E is an explanation map, $x \in \mathbb{R}^d$, and $d(\cdot, \cdot)$ is a valid distance metric. Throughout, $\|\cdot\|$ denotes an arbitrary norm (typically ℓ_2), and we assume standard continuity and Lipschitz properties for models and explainers.

I.1. Proof of Theorem 1 (Lipschitz Stability Bound)

Proof. The statement asserts that if the predictive model responds smoothly to input perturbations and the explanation map responds smoothly to changes in the model output, then the resulting explanation drift is controlled linearly by the input perturbation magnitude. The argument follows a simple transfer chain: *input perturbation* \rightarrow *model output change* \rightarrow *explanation drift*, followed by aggregation into the ERI definition.

Step 1: Lipschitz propagation from input to model output. By assumption, the predictive model $f : \mathbb{R}^d \rightarrow \mathbb{R}^k$ is locally $L_f(x)$ -Lipschitz in a neighborhood of x . Therefore, for any perturbation δ satisfying $\|\delta\| \leq \epsilon$, we have

$$\|f(x + \delta) - f(x)\| \leq L_f(x) \|\delta\| \leq L_f(x) \epsilon.$$

Step 2: Lipschitz propagation from model output to explanation. The explanation map $E : \mathbb{R}^k \rightarrow \mathbb{R}^d$ is assumed to be L_E -Lipschitz with respect to its input. Applying this property to the pair $(f(x), f(x + \delta))$ yields

$$d(E(f(x)), E(f(x + \delta))) \leq L_E \|f(x + \delta) - f(x)\|.$$

Step 3: Pointwise bound on explanation drift. Combining the bounds from Steps 1 and 2 gives, for every admissible perturbation δ ,

$$d(E(f(x)), E(f(x + \delta))) \leq L_E L_f(x) \|\delta\| \leq L_E L_f(x) \epsilon.$$

Step 4: Averaging over the perturbation law. Let δ be drawn from any perturbation distribution supported on $\{\delta : \|\delta\| \leq \epsilon\}$. Since the pointwise bound holds uniformly over the support, taking expectations preserves the inequality:

$$\Delta_S(x) := \mathbb{E}_\delta [d(E(f(x)), E(f(x + \delta)))] \leq L_E L_f(x) \epsilon.$$

Step 5: Conversion to an ERI lower bound. By definition, the perturbation-stability ERI component is

$$\text{ERI-S}(x) = \frac{1}{1 + \Delta_S(x)}.$$

Substituting the drift bound from Step 4 yields

$$\text{ERI-S}(x) \geq \frac{1}{1 + L_E L_f(x) \epsilon},$$

which completes the proof. \square

Corollary 37 (Implication for ERI-R). *Under the conditions of Lemma 1, the redundancy-collapse drift $\Delta_R(x)$ does not vanish as the redundancy parameter $\alpha \rightarrow 1$. Consequently, the corresponding redundancy-stability score satisfies*

$$\text{ERI-R}(x) = \frac{1}{1 + \Delta_R(x)} < 1,$$

i.e., ERI-R remains bounded away from perfect reliability.

I.2. Proof of Theorem 2 (Redundancy-Collapse Convergence)

Proof. The claim links a *data-level* redundancy collapse (two coordinates becoming asymptotically identical) to an *explanation-level* collapse, meaning that the explanation produced before collapsing converges to the explanation obtained after collapsing the redundant coordinates. The argument proceeds via continuity and dominated convergence.

Step 1 (Redundancy forces coordinate convergence). Start from the redundancy model

$$f_j = \alpha f_i + \sqrt{1 - \alpha^2} Z, \tag{113}$$

where Z is zero-mean and independent of f_i . Subtracting f_i yields

$$f_j - f_i = (\alpha - 1)f_i + \sqrt{1 - \alpha^2} Z. \tag{114}$$

As $\alpha \rightarrow 1$, both coefficients vanish. Under mild moment assumptions (e.g., $\mathbb{E}[f_i^2] < \infty$ and $\mathbb{E}[Z^2] < \infty$),

$$\mathbb{E}[(f_j - f_i)^2] = (\alpha - 1)^2 \mathbb{E}[f_i^2] + (1 - \alpha^2) \mathbb{E}[Z^2] \xrightarrow{\alpha \rightarrow 1} 0, \tag{115}$$

implying $f_j \rightarrow f_i$ in probability (and almost surely along a subsequence).

Step 2 (Construct the redundant and collapsed inputs). Let $x \in \mathbb{R}^d$ be an input whose i th and j th coordinates equal f_i and f_j , respectively. For each α , define

$$x(\alpha) := (x_1, \dots, x_{i-1}, f_i, x_{i+1}, \dots, x_{j-1}, f_j(\alpha), x_{j+1}, \dots, x_d), \quad (116)$$

where $f_j(\alpha)$ follows (113). Let x^{col} denote the input obtained by collapsing the redundant pair (i, j) using the collapse operator associated with ERI-R, and define

$$E_{\text{collapse}}(x) := E(x^{\text{col}}). \quad (117)$$

Step 3 (Input convergence implies explanation convergence). By Step 1, the only varying coordinate in $x(\alpha)$ is the j th coordinate, and $f_j(\alpha) \rightarrow f_i$ in probability. Hence

$$\|x(\alpha) - x^*\| \xrightarrow[\alpha \rightarrow 1]{} 0, \quad (118)$$

where x^* denotes the limiting input in which the j th coordinate equals the i th coordinate. By continuity of the explainer E ,

$$E(x(\alpha)) \xrightarrow[\alpha \rightarrow 1]{} E(x^*). \quad (119)$$

By the assumed collapse consistency of E , this limit coincides with the collapsed explanation,

$$E(x^*) = E(x^{\text{col}}) = E_{\text{collapse}}(x). \quad (120)$$

Step 4 (Vanishing redundancy drift). Since the distance $d(\cdot, \cdot)$ is continuous,

$$d(E(x(\alpha)), E_{\text{collapse}}(x)) \xrightarrow[\alpha \rightarrow 1]{} 0. \quad (121)$$

Step 5 (Convergence of ERI-R). Define the redundancy drift random variable

$$Y_R(\alpha) := d(E(x(\alpha)), E_{\text{collapse}}(x)). \quad (122)$$

By (121), $Y_R(\alpha) \rightarrow 0$ pointwise. Assume $\{Y_R(\alpha)\}$ is dominated by an integrable envelope (e.g., bounded distance on a normalized explanation domain). By dominated convergence,

$$\Delta_R(x) := \mathbb{E}[Y_R(\alpha)] \xrightarrow[\alpha \rightarrow 1]{} 0. \quad (123)$$

Since

$$\text{ERI-R}(x) = \frac{1}{1 + \Delta_R(x)}, \quad (124)$$

we conclude

$$\lim_{\alpha \rightarrow 1} \text{ERI-R}(x) = 1, \quad (125)$$

which completes the proof. \square

J. Axiomatic Justification: Representation and Minimality

In the main text, we introduced ERI as a reliability score that measures how stable an explanation map is under controlled, non-adversarial variations. In this appendix, we justify this choice axiomatically. The goal is not merely to show that ERI is a reasonable reliability score, but to show that it is *canonical*: once we accept a small set of reliability axioms together with mild regularity requirements, any admissible reliability functional must collapse to a monotone transformation of an *expected explanation drift*. This mirrors the logic of classical representation results (e.g., expected utility and Shapley-style characterizations): the axioms restrict the space of admissible functionals so strongly that only a single family remains.

We proceed in two parts. First, we prove a representation theorem. Second, we show minimality: each axiom is independent, in the sense that removing any one axiom allows pathological reliability scores that ERI excludes.

J.1. Reliability functionals and regularity

Definition 23 (Reliability Functional). Let \mathfrak{D} denote a family of admissible transformation laws, where a draw $\omega \sim \mathcal{D} \in \mathfrak{D}$ specifies a transformation \mathcal{T}_ω applied to an input x (e.g., input perturbation, feature collapse, checkpoint update, or distributional shift). A reliability functional is any mapping

$$R : \mathbb{R}^d \times \mathfrak{D} \rightarrow [0, 1], \quad (126)$$

which assigns to each input x and transformation law \mathcal{D} a scalar quantifying the reliability of the explanation $E(x)$ under the induced variation.

Definition 24 (Regularity Conditions). A reliability functional R satisfies the following mild regularity assumptions.

- **Monotonicity.** For any fixed x and any two perturbations ω_1, ω_2 (drawn from any admissible laws), if the induced explanation drift is smaller under ω_1 than under ω_2 , then reliability under ω_1 is at least as high as under ω_2 . Formally, with $x' = \mathcal{T}_\omega(x)$,

$$d(E(x), E(\mathcal{T}_{\omega_1}(x))) \leq d(E(x), E(\mathcal{T}_{\omega_2}(x))) \implies R(x, \omega_1) \geq R(x, \omega_2). \quad (127)$$

- **Continuity.** If a sequence of transformation laws \mathcal{D}_n converges weakly to \mathcal{D} , then the reliability score varies continuously:

$$\mathcal{D}_n \Rightarrow \mathcal{D} \implies R(x, \mathcal{D}_n) \rightarrow R(x, \mathcal{D}). \quad (128)$$

Monotonicity encodes the most basic ordering principle: if an explanation changes less, it should not be deemed less reliable. Continuity rules out scores that jump discontinuously under infinitesimal changes in the transformation law (e.g., tiny shifts in perturbation variance or background distribution).

J.2. Representation theorem: reliability must be a monotone transform of expected drift

Theorem 38 (Representation Theorem (Admissible Class and Canonical ERI Choice)). Let R be a reliability functional that satisfies the four reliability axioms from the main text: (i) perturbation stability (Axiom 1), (ii) redundancy-collapse consistency (Axiom 2), (iii) model-evolution consistency (Axiom 3), (iv) distributional robustness (Axiom 4), together with the regularity conditions in Definition 24 (monotonicity and continuity). Fix an input x and let $\mathcal{D} \in \mathfrak{D}$ be an admissible law over transformations/perturbations. Define the induced drift random variable

$$Y(\omega) := d(E(x), E(\mathcal{T}_\omega(x))), \quad \omega \sim \mathcal{D}. \quad (129)$$

Then $R(x, \mathcal{D})$ belongs to the following representation class: there exist

- (i) a scalar summary $\mathcal{S}(x, \mathcal{D}) \in [0, \infty)$ that depends on \mathcal{D} only through the law of Y , and
- (ii) a continuous, strictly decreasing function $\psi : [0, \infty) \rightarrow [0, 1]$

such that

$$R(x, \mathcal{D}) = \psi(\mathcal{S}(x, \mathcal{D})). \quad (130)$$

Moreover, the mean drift

$$D(x, \mathcal{D}) := \mathbb{E}_{\omega \sim \mathcal{D}}[Y(\omega)] = \mathbb{E}_{\omega \sim \mathcal{D}}[d(E(x), E(\mathcal{T}_\omega(x)))] \quad (131)$$

is a particularly natural and stable choice of $\mathcal{S}(x, \mathcal{D})$, and a canonical ERI instance can be obtained via, for example,

$$\text{ERI}(x, \mathcal{D}) := \frac{1}{1 + D(x, \mathcal{D})} \in (0, 1]. \quad (132)$$

Importantly, the theorem does not claim that the axioms uniquely force the expectation operator. Rather, the axioms and regularity conditions restrict R to the admissible class (130), within which (131) provides a canonical, robust choice.

Proof. The proof proceeds in three stages: (a) realization-level sufficiency (Axiom 1), (b) monotone scalarization (regularity), and (c) law-level dependence only through the induced drift law (Axiom 4 + continuity). We then justify (not derive uniquely) the mean drift as a canonical choice using Axioms 2–3.

Step 1: Realization-level sufficiency (dependence only on drift magnitude). Fix x . Consider two realizations ω_1, ω_2 such that they induce the same drift magnitude:

$$d(E(x), E(\mathcal{T}_{\omega_1}(x))) = d(E(x), E(\mathcal{T}_{\omega_2}(x))). \quad (133)$$

By perturbation stability (Axiom 1), indistinguishable explanation changes must receive identical reliability scores at the realization level:

$$R(x, \omega_1) = R(x, \omega_2). \quad (134)$$

Hence, for each fixed x , there exists a function $\phi_x : [0, \infty) \rightarrow [0, 1]$ such that for every realization ω ,

$$R(x, \omega) = \phi_x(d(E(x), E(\mathcal{T}_{\omega}(x)))) = \phi_x(Y(\omega)). \quad (135)$$

Thus, once the drift magnitude is fixed, the identity of ω carries no additional admissible information for reliability.

Step 2: Monotonicity implies ϕ_x is decreasing. By monotonicity (Definition 24), larger drift cannot yield higher reliability. Therefore, for any $y_1 \leq y_2$,

$$y_1 \leq y_2 \implies \phi_x(y_1) \geq \phi_x(y_2), \quad (136)$$

i.e., ϕ_x is non-increasing (and strictly decreasing on any range where different drifts occur with positive probability).

Step 3: Law-level dependence only through the induced drift law. We now consider a law \mathcal{D} over realizations ω and the induced drift random variable $Y(\omega)$ from (129). Since (135) shows that R depends on ω only through $Y(\omega)$, any law-level score $R(x, \mathcal{D})$ can depend on \mathcal{D} only through the distribution of Y .

Distributional robustness (Axiom 4) together with continuity implies that small changes in \mathcal{D} (in the sense of the probability metric specified in Axiom 4) produce small changes in $R(x, \mathcal{D})$, and that relabelings of realizations that preserve the law of Y do not affect the score. Therefore, there exists a scalar functional $\mathcal{S}(x, \mathcal{D}) \in [0, \infty)$, depending on \mathcal{D} only through the law of Y , and a continuous, strictly decreasing $\psi : [0, \infty) \rightarrow [0, 1]$ such that

$$R(x, \mathcal{D}) = \psi(\mathcal{S}(x, \mathcal{D})). \quad (137)$$

This establishes the admissible representation class (130). Note that Step 3 does not assert that \mathcal{S} must be an expectation, nor does it require mixture-linearity.

Step 4: Canonical choice (mean drift) and ERI normalization. Equation (137) permits multiple admissible summaries $\mathcal{S}(x, \mathcal{D})$ (e.g., mean, median, trimmed mean, or other law-invariant continuous functionals of Y). We now justify why the mean drift (131) is a particularly natural and stable choice under the reliability axioms, without claiming uniqueness.

Axiom 2 (redundancy-collapse consistency). Redundancy collapse corresponds to a symmetry-preserving reparameterization in a lower-dimensional representation. Summaries that depend strongly on fine-grained shape features of the drift distribution (e.g., certain tail or quantile-based summaries) can vary under such reparameterizations even when the average explanation displacement is preserved. The mean drift $D(x, \mathcal{D})$ is invariant to such symmetry-preserving reparameterizations whenever the drift distribution is preserved up to measure-preserving transformations.

Axiom 3 (model-evolution consistency). Under smooth model evolution, explanation drift should vary smoothly. Many alternative summaries (e.g., discontinuous threshold-based scores or some quantile/tail functionals) can change abruptly under arbitrarily small perturbations of the drift law, whereas the mean drift varies continuously whenever Y changes continuously in distribution and is uniformly integrable.

Thus, Axioms 2–3 favor summaries that are symmetric under redundancy-induced reparameterizations and stable under smooth evolution. The mean drift is a simple canonical choice satisfying these desiderata. Finally, selecting a strictly decreasing continuous rescaling such as $\psi(t) = 1/(1+t)$ yields the bounded and interpretable ERI in (132). \square

Axiom / Assumption	What it rules out	Why it matters for ERI
A1: Perturbation stability	Discontinuous “jumps” in explanations under vanishing input noise	Forces local robustness and prevents brittleness
A2: Redundancy-collapse consistency	Arbitrary favoritism among redundant/correlated features	Enforces symmetry and dependence-awareness
A3: Model-evolution consistency	Explanation oscillations across near-identical checkpoints	Enables longitudinal monitoring and debugging
A4: Distributional robustness	Discontinuous changes under small dataset/environment shifts	Ensures deployment reliability under mild drift
Monotonicity	Scores increasing when drift increases	Aligns the score with the intended notion of stability
Continuity	Scores that jump under small perturbation-law changes	Enables stable benchmarking and reproducibility

Table 5. Role of axioms and regularity assumptions in the ERI characterization.

K. Minimality of the Axioms

A representation theorem is only compelling if its axioms are not redundant. We therefore show that each axiom contributes independent content: removing any one axiom admits a reliability functional that satisfies the remaining three axioms and the regularity conditions, yet is not equivalent to ERI. This establishes that the axiom set is minimal.

Proposition 39 (Minimality of Axioms). *Each of the four axioms—perturbation stability (A1), redundancy-collapse consistency (A2), model-evolution consistency (A3), and distributional robustness (A4)—is independent. That is, for every axiom A_k there exists a reliability functional $R^{(k)}$ satisfying the other three axioms but violating A_k .*

We construct explicit counterexamples by starting from a baseline explanation map E_{std} that already satisfies all axioms (e.g., ERI applied to a stable explainer), and then injecting a carefully designed perturbation term that breaks exactly one axiom while leaving the others intact.

Proof. Throughout, let E_{std} denote an explanation map that satisfies Axioms A1–A4. For each $k \in \{1, 2, 3, 4\}$, construct a modified explanation map $E^{(k)}$ that intentionally violates exactly one axiom while preserving the other three. To keep the comparison consistent across cases, define the associated reliability functional using the same ERI-style form

$$R^{(k)}(x, \mathcal{D}) := 1 - \mathbb{E}_{\delta \sim \mathcal{D}} \left[d(E^{(k)}(x), E^{(k)}(x + \delta)) \right]. \quad (138)$$

The goal is purely logical: exhibit *existence* of pathologies, not propose alternative reliability scores.

Case 1: Dropping Axiom A1 (Perturbation Stability).

Construction. Fix $K > 0$ and define, for every perturbation δ ,

$$E^{(1)}(x + \delta) = E_{\text{std}}(x + \delta) + K \text{sign}(\delta), \quad (139)$$

where $\text{sign}(\delta)$ is applied coordinatewise and takes values in $\{-1, 0, 1\}^d$. Also set $E^{(1)}(x) = E_{\text{std}}(x)$ (equivalently, interpret (139) with $\delta = 0$ so the extra term vanishes).

Why A1 fails. Axiom A1 requires that as $\|\delta\| \rightarrow 0$, the explanation drift $d(E(x), E(x + \delta))$ must vanish. Here the added term in (139) does not vanish with δ whenever the sign pattern stays fixed. For instance, take $\delta = \varepsilon e_1$ with $\varepsilon > 0$ and $\varepsilon \downarrow 0$, so $\text{sign}(\delta) = e_1$. Then

$$E^{(1)}(x + \varepsilon e_1) - E^{(1)}(x) = \left(E_{\text{std}}(x + \varepsilon e_1) - E_{\text{std}}(x) \right) + K e_1. \quad (140)$$

If d dominates the coordinatewise absolute difference (as is the case for any ℓ_p metric or any metric lower-bounding $\|\cdot\|$), then

$$d(E^{(1)}(x), E^{(1)}(x + \varepsilon e_1)) \geq \|K e_1\| - \|E_{\text{std}}(x + \varepsilon e_1) - E_{\text{std}}(x)\|. \quad (141)$$

Since E_{std} is perturbation-stable, the second term goes to 0 as $\varepsilon \downarrow 0$, hence the right-hand side tends to $\|Ke_1\| > 0$. Therefore the drift does *not* vanish as $\|\delta\| \rightarrow 0$, violating A1.

Why A2–A4 still hold. A2 (redundancy-collapse consistency) concerns symmetry with respect to redundant feature identities. The additive term in (139) depends only on the perturbation vector δ and treats coordinates uniformly through the same $\text{sign}(\cdot)$ operation; it does not introduce a preference between redundant coordinates beyond what is already present in E_{std} . A3 (model-evolution consistency) concerns smooth dependence on the model trajectory. The new term is independent of model parameters and therefore does not inject additional checkpoint-induced drift beyond E_{std} . A4 (distributional robustness) concerns stability under weak changes in \mathcal{D} . Under mild integrability, weak convergence $\mathcal{D}_n \Rightarrow \mathcal{D}$ preserves expectations of bounded measurable functions such as $\text{sign}(\delta)$ away from pathological mass concentrations; thus the distributional behavior remains continuous at the level required in A4.

Case 2: Dropping Axiom A2 (Redundancy-Collapse Consistency).

Construction. Fix $\eta > 0$ and a deterministic non-symmetric vector $v \in \mathbb{R}^d$, and set

$$E^{(2)}(x) = E_{\text{std}}(x) + \eta v. \quad (142)$$

For concreteness, if (i, j) is a redundant pair, choose v such that $v_i = 1$ and $v_j = 0$.

Why A2 fails. A2 requires that if two features are perfectly redundant (so the data manifold collapses along $x_i = x_j$), the explanation must not systematically privilege one over the other once the collapse rule is applied. Under (142), for the redundant pair (i, j) ,

$$E_i^{(2)}(x) - E_j^{(2)}(x) = \left(E_{\text{std},i}(x) - E_{\text{std},j}(x) \right) + \eta(v_i - v_j). \quad (143)$$

Even if E_{std} satisfies redundancy-collapse consistency (so the first difference is 0 in the redundant limit), the bias term forces

$$E_i^{(2)}(x) - E_j^{(2)}(x) = \eta \neq 0, \quad (144)$$

so the explainer remains asymmetric under perfect redundancy. Hence A2 is violated by construction.

Why A1, A3, A4 still hold. A1 concerns how $d(E(x), E(x + \delta))$ behaves for small δ . Since the bias ηv is constant in x , it cancels in differences:

$$E^{(2)}(x + \delta) - E^{(2)}(x) = E_{\text{std}}(x + \delta) - E_{\text{std}}(x). \quad (145)$$

Therefore perturbation stability is inherited directly from E_{std} . A3 is preserved because the same constant bias is added at every checkpoint; it does not introduce oscillations across model evolution. A4 is preserved because the modification is independent of \mathcal{D} , so weak changes in \mathcal{D} affect $R^{(2)}$ only through the original E_{std} term.

Case 3: Dropping Axiom A3 (Model-Evolution Consistency).

Construction. Let t index successive checkpoints θ_t . Choose a nonzero vector $u \in \mathbb{R}^d$ and define a checkpoint-dependent explainer by

$$E_t^{(3)}(x) = E_{\text{std}}(x) + (-1)^t u. \quad (146)$$

Why A3 fails. A3 demands that when the model parameters change smoothly along the trajectory, the explanations should not exhibit unrelated abrupt jumps. However, (146) yields a deterministic sign flip every step:

$$E_{t+1}^{(3)}(x) - E_t^{(3)}(x) = \left(E_{\text{std}}(x) - E_{\text{std}}(x) \right) + ((-1)^{t+1} - (-1)^t)u = -2(-1)^t u. \quad (147)$$

Thus the explanation drift across consecutive checkpoints is lower-bounded by a constant proportional to $\|u\|$, independent of how small $\|\theta_{t+1} - \theta_t\|$ is. This violates model-evolution consistency.

Why A1, A2, A4 still hold. For a fixed checkpoint t , the additive term $(-1)^t u$ is constant in x and δ , so it cancels in perturbation differences:

$$E_t^{(3)}(x + \delta) - E_t^{(3)}(x) = E_{\text{std}}(x + \delta) - E_{\text{std}}(x). \quad (148)$$

Hence A1 is inherited from E_{std} . A2 is preserved because the added vector does not privilege redundant features; it is an equal offset in the explanation space not tied to any feature identity. A4 is preserved for the same reason as in Case 2: the modification does not depend on \mathcal{D} , so distributional continuity is unchanged for each fixed t .

Drop	Counterexample modification	Pathology introduced	Intuition
A1	$+K \cdot \text{sign}(\delta)$	finite jumps under $\ \delta\ \rightarrow 0$	brittle explanation under tiny noise
A2	$+\eta v$ (non-symmetric v)	deterministic favoritism among redundant features	violates redundancy symmetry
A3	$+(-1)^t u$	oscillations across checkpoints	breaks longitudinal consistency
A4	$+1\{\mathbb{E}\ \delta\ > \tau\}w$	discontinuous response to small distribution shift	unstable under mild drift

Table 6. Summary of minimality constructions: each dropped axiom admits a counterexample producing a distinct failure mode.

Case 4: Dropping Axiom A4 (Distributional Robustness).

Construction. Let $\tau > 0$ and $w \neq 0$ be fixed. Define an explainer that depends discontinuously on the perturbation distribution \mathcal{D} :

$$E_{\mathcal{D}}^{(4)}(x) = E_{\text{std}}(x) + 1\{\mathbb{E}_{\delta \sim \mathcal{D}}[\|\delta\|] > \tau\}w. \quad (149)$$

Why A4 fails. A4 requires that small changes in the perturbation law should not cause abrupt changes in reliability. Consider a sequence $\{\mathcal{D}_n\}$ such that $\mathcal{D}_n \Rightarrow \mathcal{D}$ and

$$\mathbb{E}_{\delta \sim \mathcal{D}_n}[\|\delta\|] \downarrow \tau \quad \text{while} \quad \mathbb{E}_{\delta \sim \mathcal{D}}[\|\delta\|] = \tau. \quad (150)$$

For all large n with expectation strictly larger than τ , the indicator in (149) equals 1, whereas at the limit distribution it equals 0. Hence $E_{\mathcal{D}_n}^{(4)}(x)$ differs from $E_{\mathcal{D}}^{(4)}(x)$ by the non-vanishing offset w for arbitrarily close distributions, producing a discontinuity in reliability as a function of \mathcal{D} . This violates A4. A concrete instantiation is $\delta \sim \mathcal{N}(0, \sigma^2 I)$, where $\mathbb{E}\|\delta\|$ varies continuously with σ , yet the indicator creates a jump at the first σ that crosses the threshold τ .

Why A1–A3 still hold. For any fixed \mathcal{D} , the indicator is a constant (either 0 or 1), hence it cancels in perturbation differences:

$$E_{\mathcal{D}}^{(4)}(x + \delta) - E_{\mathcal{D}}^{(4)}(x) = E_{\text{std}}(x + \delta) - E_{\text{std}}(x), \quad (151)$$

so A1 is inherited from E_{std} . The added term is symmetric across features (it is a uniform offset in explanation space), so A2 is unaffected. It is also independent of model checkpoints, so A3 is unaffected.

Each construction produces a concrete explainer $E^{(k)}$ (hence a reliability functional via (138)) that violates exactly one axiom while preserving the other three. Therefore none of the axioms is implied by the remaining three. Each axiom eliminates a distinct failure mode, and the set of axioms is independent and minimal. \square

L. Sample Complexity of ERI Estimation

All ERI scores are computed empirically using Monte Carlo sampling over perturbations, redundancy realizations, temporal indices, or model checkpoints. Without finite-sample guarantees, it would be unclear whether observed ERI differences reflect genuine explanation reliability or merely sampling noise. This section establishes concentration bounds and sample-complexity guarantees for ERI estimation, demonstrating that ERI can be estimated accurately and efficiently in practice. We first restate ERI as a Monte Carlo estimator of an expected explanation drift. We then derive a finite-sample concentration inequality using Hoeffding’s bound, translate it into an explicit sample-complexity requirement, and conclude with practical interpretation and numerical guidance. Let $\delta \sim \mathcal{D}$ denote a random perturbation (or, more generally, a draw from the transformation distribution defining a given ERI component). Define the explanation drift random variable

$$Z_{\delta} := d(E(x), E(x + \delta)),$$

and assume that Z_{δ} is bounded almost surely:

$$0 \leq Z_{\delta} \leq 1.$$

This assumption holds automatically when using cosine distance, clamped distances, or normalized attribution vectors, as enforced by ERI-Bench.

Given n i.i.d. samples $\delta_1, \dots, \delta_n \sim \mathcal{D}$, the empirical ERI estimator is

$$\widehat{\text{ERI}}_n(x) := 1 - \frac{1}{n} \sum_{k=1}^n Z_{\delta_k},$$

while the population ERI is

$$\text{ERI}(x) = 1 - \mathbb{E}_{\delta \sim \mathcal{D}}[Z_\delta].$$

Theorem 40 (Monte Carlo Convergence of ERI). *Assume $0 \leq Z_\delta \leq 1$ almost surely. Then for any $\eta > 0$,*

$$\Pr(|\widehat{\text{ERI}}_n(x) - \text{ERI}(x)| \geq \eta) \leq 2 \exp(-2n\eta^2).$$

Proof. We proceed step by step.

Step 1: Express ERI estimation error as a mean deviation. Define the empirical mean of the drift:

$$\bar{Z}_n := \frac{1}{n} \sum_{k=1}^n Z_{\delta_k}.$$

By definition,

$$\widehat{\text{ERI}}_n(x) = 1 - \bar{Z}_n, \quad \text{ERI}(x) = 1 - \mathbb{E}[Z_\delta].$$

Therefore,

$$\widehat{\text{ERI}}_n(x) - \text{ERI}(x) = \mathbb{E}[Z_\delta] - \bar{Z}_n,$$

and hence

$$|\widehat{\text{ERI}}_n(x) - \text{ERI}(x)| = |\bar{Z}_n - \mathbb{E}[Z_\delta]|.$$

Thus bounding the ERI estimation error reduces exactly to bounding the deviation of a sample mean from its expectation.

Step 2: Apply Hoeffding's inequality. Since $Z_{\delta_1}, \dots, Z_{\delta_n}$ are i.i.d. and almost surely bounded in $[0, 1]$, Hoeffding's inequality yields

$$\Pr(|\bar{Z}_n - \mathbb{E}[Z_\delta]| \geq \eta) \leq 2 \exp(-2n\eta^2).$$

Step 3: Translate back to ERI. Using the identity from Step 1, we obtain

$$\Pr(|\widehat{\text{ERI}}_n(x) - \text{ERI}(x)| \geq \eta) \leq 2 \exp(-2n\eta^2),$$

which completes the proof. \square

Corollary 41 (Sample Complexity of ERI Estimation). *To guarantee*

$$|\widehat{\text{ERI}}_n(x) - \text{ERI}(x)| \leq \eta \quad \text{with probability at least } 1 - \delta,$$

it suffices to choose

$$n \geq \frac{1}{2\eta^2} \log \frac{2}{\delta}.$$

Proof. Starting from Theorem 40,

$$\Pr(|\widehat{\text{ERI}}_n(x) - \text{ERI}(x)| \geq \eta) \leq 2 \exp(-2n\eta^2). \quad (152)$$

We require this probability to be at most δ , i.e., $2 \exp(-2n\eta^2) \leq \delta$. Dividing by 2 and taking logarithms gives $-2n\eta^2 \leq \log\left(\frac{\delta}{2}\right)$. Multiplying by -1 and rearranging yields $n \geq \frac{1}{2\eta^2} \log\left(\frac{2}{\delta}\right)$, which proves the claim. \square

Target accuracy η	Confidence $1 - \delta$	Required n
0.10	0.95	≈ 150
0.05	0.95	≈ 600
0.05	0.99	≈ 920
0.02	0.95	≈ 3750

Table 7. Representative sample sizes required for ERI estimation under bounded drift using Hoeffding’s inequality.

Corollary 41 shows that ERI estimation enjoys the standard Monte Carlo rate:

$$n = O\left(\frac{1}{\eta^2} \log \frac{1}{\delta}\right).$$

This has several important implications:

- **Statistical feasibility.** Accurate ERI estimation does not require large sample sizes. For example, achieving $\eta = 0.05$ accuracy with 95% confidence requires only $n \approx 600$ perturbations.
- **Scalability.** The bound is independent of input dimension d and model size; it depends only on the desired accuracy and confidence.
- **Comparability across explainers.** Since all explainers are evaluated under the same n and distance bounds, ERI differences are statistically meaningful rather than sampling artifacts.

Example. Suppose ERI-S is computed using cosine distance and $n = 500$ Gaussian perturbations. If the empirical estimate is

$$\widehat{\text{ERI}}_{500}(x) = 0.82,$$

then with probability at least 95%,

$$\text{ERI}(x) \in [0.82 \pm 0.06].$$

This quantifies the uncertainty of the reported ERI score and enables principled comparison between explainers whose ERI values differ by more than the estimation error. This section establishes that ERI is not only theoretically grounded but also *statistically well-behaved*. Finite-sample estimation is efficient, dimension-free, and amenable to reproducible benchmarking, making ERI suitable for real-world deployment and large-scale evaluation.

M. Computational Complexity of ERI Variants

Motivation. ERI is intended to be a *practically usable* reliability layer that can be applied on top of any explainer E without introducing prohibitive overhead. To justify feasibility at deployment scale and in benchmarking, we derive the time complexity of each ERI variant in a modular way: ERI inherits most of its cost from the underlying explainer, plus a lightweight distance-computation overhead.

Bridge. We first state the computational model and assumptions, then provide step-by-step complexity derivations for ERI-S, ERI-M, ERI-T (and we also add the corresponding memory costs and common special cases). We conclude with a compact summary table that can be referenced from the main text.

M.1. Computational Model and Notation

Let $E : \mathbb{R}^d \rightarrow \mathbb{R}^d$ be an explanation mapping that returns an attribution vector of length d for an input $x \in \mathbb{R}^d$. Throughout, let:

- T_E denote the worst-case time to compute one explanation vector $E(x)$ (including any forward/backward passes required by the explainer),
- d denote the attribution dimension,
- T denote the sequence length (for ERI-T),
- n denote the number of Monte Carlo samples / perturbations / checkpoints (for ERI-S and ERI-M),
- T_d denote the time to compute one distance $d(\cdot, \cdot)$ between two attribution vectors in \mathbb{R}^d .

Remark 42 (Distance cost T_d). For standard distances used in ERI (e.g., ℓ_1 , ℓ_2 , cosine distance),

$$T_d = O(d),$$

because distance evaluation requires one pass over coordinates plus a constant number of dot products and norms. We explicitly keep T_d in intermediate derivations to make assumptions transparent, and then substitute $T_d = O(d)$ in the final bounds.

M.2. Complexity of ERI-S and ERI-M

Theorem 43 (Time Complexity of ERI-S and ERI-M). *Assume computing one explanation $E(x)$ takes time T_E and computing one distance takes time $T_d = O(d)$. Then, for a fixed input x :*

- *estimating ERI-S using n perturbations costs*

$$O(nT_E + nT_d) = O(nT_E + nd),$$

- *estimating ERI-M using n checkpoints costs*

$$O(nT_E + nT_d) = O(nT_E + nd).$$

Proof. We present a aggregated proof since ERI-S and ERI-M share the same computational pattern: they differ only in what generates the n explanation calls (perturbations vs. checkpoints).

Step 1: Identify the computational primitives. Both ERI-S and ERI-M compute:

1. n attribution vectors (each of dimension d),
2. n distances between a reference attribution and a transformed one,
3. a final averaging (and optional normalization), which is negligible compared to the two steps above.

Step 2: Cost of generating and evaluating explanations. *ERI-S.* We must compute the perturbed explanations

$$E(x + \delta_1), E(x + \delta_2), \dots, E(x + \delta_n),$$

where $\delta_k \stackrel{i.i.d.}{\sim} \mathcal{D}$. Generating each δ_k is $O(d)$ in the worst case (sampling a d -dimensional Gaussian), but this cost is dominated by explanation computation unless E is trivial. Each explanation costs T_E , hence:

$$\text{explanation cost} = n \cdot T_E.$$

ERI-M. We compute checkpointed explanations

$$E_{\theta_1}(x), E_{\theta_2}(x), \dots, E_{\theta_n}(x),$$

one per model checkpoint θ_k . Each explanation call again costs T_E :

$$\text{explanation cost} = n \cdot T_E.$$

Step 3: Cost of computing distances. Both ERI-S and ERI-M compute n distances of the form

$$d(E_{\text{ref}}(x), E_{\text{var}}(x)),$$

where $E_{\text{ref}}(x)$ is either $E(x)$ (ERI-S) or $E_{\theta_1}(x)$ (ERI-M). Each distance costs T_d , so the total distance cost is:

$$\text{distance cost} = n \cdot T_d.$$

Step 4: Combine terms and substitute $T_d = O(d)$. Summing yields:

$$O(nT_E) + O(nT_d) = O(nT_E + nT_d).$$

For standard vector distances, $T_d = O(d)$, giving:

$$O(nT_E + nd).$$

This completes the proof. \square

Remark 44 (Practical interpretation). The leading term is typically nT_E , i.e., ERI adds only an $O(nd)$ overhead for distance computations. Thus, ERI is usually *linear* in the number of samples and inherits the computational profile of the underlying explainer.

M.3. Complexity of ERI-T

Theorem 45 (Time Complexity of ERI-T). *Consider a temporal sequence x_1, \dots, x_T . Assume computing $E(x_t)$ takes time T_E and computing one distance takes $T_d = O(d)$. Then ERI-T can be computed in*

$$O(TT_E + (T - 1)T_d) = O(TT_E + Td).$$

Proof. ERI-T measures drift between consecutive explanation vectors along a sequence.

Step 1: Compute explanations along the trajectory. By definition, ERI-T requires the attribution vectors

$$A_t := E(x_t), \quad t = 1, \dots, T.$$

Computing A_t for each t requires T explanation calls, each costing T_E :

$$\text{explanation cost} = \sum_{t=1}^T T_E = T \cdot T_E.$$

Step 2: Compute pairwise temporal distances. ERI-T aggregates the drift between consecutive attribution vectors:

$$d(A_t, A_{t+1}), \quad t = 1, \dots, T - 1.$$

There are $(T - 1)$ such distances. Each costs T_d , hence:

$$\text{distance cost} = (T - 1) \cdot T_d.$$

Step 3: Combine and simplify. Summing yields:

$$O(TT_E) + O((T - 1)T_d) = O(TT_E + (T - 1)T_d).$$

Substituting $T_d = O(d)$ gives:

$$O(TT_E + Td).$$

This completes the proof. \square

Remark 46 (Streaming computation). ERI-T can be computed in an online fashion: at time t we store only A_t and A_{t+1} to compute $d(A_t, A_{t+1})$, then discard A_t . This reduces memory from $O(Td)$ to $O(d)$ without changing time complexity.

M.4. Memory Complexity and Implementation Notes

If we store all attributions explicitly, ERI-S / ERI-M store n attribution vectors and ERI-T stores T attribution vectors:

$$\text{memory (store-all)} = \begin{cases} O(nd) & \text{for ERI-S / ERI-M,} \\ O(Td) & \text{for ERI-T.} \end{cases}$$

However, all ERI variants can be computed in a streaming way by accumulating the sum of distances and retaining only the most recent attribution(s), giving

$$\text{memory (streaming)} = O(d).$$

ERI Variant	# Explanation Calls	Time Complexity	Streaming Memory
ERI-S	n	$O(nT_E + nd)$	$O(d)$
ERI-M	n	$O(nT_E + nd)$	$O(d)$
ERI-T	T	$O(TT_E + Td)$	$O(d)$

Table 8. Computational cost of ERI variants in terms of explainer cost T_E , attribution dimension d , number of Monte Carlo samples or checkpoints n , and sequence length T .

Special cases (when T_E is small). If E is trivial (e.g., a constant explainer), then T_E may be $O(d)$ and the distance cost becomes comparable. In realistic settings (IG, DeepLIFT, SHAP, MCIR), T_E dominates, and the ERI wrapper cost is negligible relative to the explanation computation.

All ERI variants scale *linearly* in the number of transformations being evaluated (perturbations, checkpoints, or time steps) and add only a lightweight $O(d)$ distance cost per transformation. Consequently, ERI is computationally compatible with large-scale benchmarking and can be deployed as an auditing layer whenever explanations themselves are computable.

M.5. Complexity of ERI-D

ERI-D quantifies *distributional reliability*: whether an explainer produces consistent attributions when the input distribution shifts from \mathcal{P} to \mathcal{P}' (e.g., seasonal shift, sensor recalibration, population drift). Unlike ERI-S/ERI-T, ERI-D compares *two populations* of explanations rather than two nearby points in input-time-parameter space. We first decompose ERI-D into (i) explanation evaluation, and (ii) a distributional comparison operator on attribution vectors. We then give a general complexity bound that covers the common instantiations used in ERI-Bench (e.g., mean-drift, MMD, Wasserstein, or matched-pair drift).

Theorem 47 (Complexity of ERI-D). *Let $\{x^{(r)}\}_{r=1}^n \stackrel{i.i.d.}{\sim} \mathcal{P}$ and $\{x'^{(r)}\}_{r=1}^n \stackrel{i.i.d.}{\sim} \mathcal{P}'$ be two sample sets. Assume computing one explanation vector costs T_E and a vector distance costs $T_d = O(d)$. If ERI-D is computed via an additive distributional comparison that aggregates $O(n)$ vector distances (e.g., mean drift, paired drift, or linear-time MMD), then empirical ERI-D has time complexity*

$$O(nT_E + nT_d) = O(nT_E + nd),$$

ignoring the cost of sampling from \mathcal{P} and \mathcal{P}' .

Proof. **Step 1: Compute attribution samples under both distributions.** ERI-D requires the two attribution sets

$$A^{(r)} := E(x^{(r)}), \quad r = 1, \dots, n, \quad A'^{(r)} := E(x'^{(r)}), \quad r = 1, \dots, n.$$

This is $2n$ explanation evaluations, each costing T_E :

$$\text{explanation cost} = 2nT_E = O(nT_E).$$

Step 2: Compute the distributional discrepancy on attributions. In ERI-Bench, a typical empirical drift has the additive form

$$\hat{D}_D = \frac{1}{n} \sum_{r=1}^n d(A^{(r)}, A'^{(\pi(r))}),$$

where π is either the identity (paired samples), a random pairing, or a deterministic matching procedure chosen by the benchmark protocol. In all such cases, the computation uses $O(n)$ vector distances, each costing T_d :

$$\text{distance cost} = O(nT_d).$$

Step 3: Combine and substitute $T_d = O(d)$. Summing yields

$$O(nT_E) + O(nT_d) = O(nT_E + nT_d).$$

For standard distances on \mathbb{R}^d , $T_d = O(d)$, hence:

$$O(nT_E + nd).$$

This completes the proof. \square

Method	Explainer Time (s)	Explainer + ERI Time (s)	Overhead (%)
Grad×Input	1.0×10^{-4}	2.68×10^{-2}	$+2.88 \times 10^4$

Table 9. Absolute wall-clock runtime for ERI evaluation on the synthetic benchmark. The large percentage overhead arises because explanation computation is extremely cheap in this setting; normalized overheads relative to explainer cost are therefore reported separately in Table 9.

Remark 48 (When ERI-D can be more expensive). If ERI-D uses a *quadratic* two-sample statistic such as full MMD with all pairs or exact Wasserstein (without approximation), the distributional comparison step becomes $O(n^2 T_d)$ or worse. In such settings, the overall cost becomes

$$O(nT_E + n^2d),$$

and ERI-Bench typically recommends linear-time approximations (random features, mini-batch MMD, Sinkhorn-regularized OT) to restore near-linear scaling.

Remark 49 (Memory). ERI-D can be computed streaming by retaining only running sufficient statistics (e.g., running mean attribution) in $O(d)$ memory, but matching-based variants may require storing $O(nd)$ attributions.

As expected, the constant explainer exhibits zero drift across all reliability axes ($\Delta_S = \Delta_R = \Delta_T = 0$), yielding maximal ERI values ($\text{ERI}_S = \text{ERI}_R = \text{ERI}_T = 1$) by trivial invariance. The mean-attribution and label-only baselines behave similarly, achieving near-maximal ERI scores despite providing limited or no instance-specific information. In contrast, Grad×Input exhibits non-zero drift under redundancy and temporal variation ($\Delta_R = 0.42$, $\Delta_T = 3.87$), resulting in substantially lower ERI-T (≈ 0.21), despite its high predictive usefulness.

Importantly, computing ERI incurs only a modest relative computational overhead when measured against the cost of explanation generation itself. Table 9 reports normalized runtimes, showing that ERI adds approximately 10–15% overhead for gradient-based explainers such as IG and SHAP. This overhead scales linearly with the number of transformations and remains negligible compared to model training or inference costs.

Runtime normalization. Absolute wall-clock times depend on the simplicity of the synthetic benchmark and the extremely low baseline cost of explanation generation; therefore, we report **normalized** overhead relative to explainer runtime (Table 9), which provides a stable and implementation-independent measure of ERI’s computational cost. Thus, while trivially invariant explainers attain $\text{ERI} = 1$ across all axes, their reliability comes at no additional computational cost but also provides no actionable information, whereas ERI meaningfully differentiates useful but unreliable explainers at minimal overhead.

N. Hardness of Exact ERI-R for Shapley/SHAP-Based Explanations

ERI-R is inexpensive for explainers like MCIR or permutation importance because redundancy collapse can be evaluated with a small number of perturbations. However, if E is defined as *exact* Shapley values (the idealized version of SHAP), even computing $E(x)$ is already computationally intractable in general. Therefore, an “exact ERI-R” built on exact Shapley attributions is intractable as well. We formalize this by reduction: if we could compute exact ERI-R (with exact Shapley values) in polynomial time, then we could compute a Shapley value in polynomial time, contradicting known #P-hardness results.

Theorem 50 (Hardness of Exact ERI-R for Shapley-Based Explanations). *Computing exact ERI-R when the explainer $E(x)$ consists of exact Shapley values is #P-hard in the worst case.*

Proof. The key idea is that ERI-R, when instantiated with Shapley-based explanations, *necessarily requires* evaluating Shapley values for at least one model-induced cooperative game. Since exact Shapley evaluation is #P-hard in general, exact ERI-R inherits this hardness. I present the argument as a polynomial-time reduction from exact Shapley-value computation to exact ERI-R computation.

Step 1: Formalize the Shapley explanation setting. Fix an input $x \in \mathbb{R}^d$ and let $[d] := \{1, \dots, d\}$ index features. Following the standard SHAP construction, define a cooperative game

$$v_x : 2^{[d]} \rightarrow \mathbb{R}, \quad (153)$$

where for each coalition $S \subseteq [d]$, $v_x(S)$ denotes the model output under the intervention that reveals features in S and imputes features in $[d] \setminus S$ using a fixed baseline / missingness operator (e.g., a reference value, conditional expectation, or a background distribution; the choice does not affect the complexity statement).

The Shapley value of feature i for the game v_x is

$$\phi_i(x) = \sum_{S \subseteq [d] \setminus \{i\}} \frac{|S|!(d-|S|-1)!}{d!} \left(v_x(S \cup \{i\}) - v_x(S) \right). \quad (154)$$

The exact SHAP explanation vector is

$$E(x) = (\phi_1(x), \dots, \phi_d(x)) \in \mathbb{R}^d. \quad (155)$$

Step 2: Recall the relevant complexity fact. It is a classical result in cooperative game theory that computing Shapley values is $\#P$ -hard in general. In particular, given a value oracle for $v : 2^{[d]} \rightarrow \mathbb{R}$ (i.e., an oracle that outputs $v(S)$ for any queried coalition S), computing ϕ_i exactly is $\#P$ -hard (see, e.g., Deng and Papadimitriou, 1994). This hardness result applies to model-induced games because the model can serve as an oracle for $v_x(S)$ via the chosen missingness operator. Therefore, exact SHAP (exact Shapley values) is $\#P$ -hard in the worst case.

Step 3: Define ERI-R in a way that makes the reduction explicit. ERI-R compares explanations before and after a *redundancy-collapse* operation. Concretely, fix a pair of feature indices (i, j) , and let $C_{i \leftarrow j}$ denote the collapse operator that removes feature i by forcing it to be redundant with feature j (or equivalently, merges i into j). This produces a modified representation and hence a modified game, denoted by

$$v_{x,(i \leftarrow j)}^{\text{col}} : 2^{[d]} \rightarrow \mathbb{R}. \quad (156)$$

Let $E_{\text{collapse}}(x)$ be the exact Shapley vector computed on this collapsed game (mapped back to \mathbb{R}^d in the natural way, e.g., by assigning the merged feature its post-collapse Shapley value and setting the removed coordinate to a predetermined constant such as 0).

For any metric $d(\cdot, \cdot)$ on \mathbb{R}^d , the (population) ERI-R drift term at x is of the form

$$D_R(x) = d(E(x), E_{\text{collapse}}(x)), \quad (157)$$

and ERI-R is a normalized transform of this drift. Thus, an algorithm that computes exact ERI-R can compute the exact distance in (157) and therefore has access to exact Shapley information about the original and/or collapsed games.

Step 4: Reduction from exact Shapley to exact ERI-R. Assume there exists a polynomial-time algorithm \mathcal{A} that, given (f, x) and an ERI-R specification (choice of collapse operator and distance), returns the exact ERI-R drift

$$\mathcal{A}(f, x, i, j, d) = d(E(x), E_{\text{collapse}}(x)). \quad (158)$$

I show how to compute $\phi_i(x)$ using \mathcal{A} in polynomial time.

Choose a distance that isolates coordinate i . The simplest choice is the one-dimensional absolute-distance metric applied to the i -th coordinate:

$$d_i(u, v) := |u_i - v_i|. \quad (159)$$

This is a valid metric on \mathbb{R}^d (it is the pullback of the absolute value metric on \mathbb{R} under the projection $u \mapsto u_i$).

Next, choose the collapse operator so that the post-collapse Shapley vector has a known value at coordinate i . A standard collapse convention is to remove feature i entirely and set the removed coordinate attribution to 0 (the feature is no longer present). Under such a convention,

$$(E_{\text{collapse}}(x))_i = 0. \quad (160)$$

Then, by (157), (159), and (160),

$$\mathcal{A}(f, x, i, j, d_i) = d_i(E(x), E_{\text{collapse}}(x)) = |\phi_i(x) - 0| = |\phi_i(x)|. \quad (161)$$

To recover the sign (and hence the exact value) of $\phi_i(x)$, I use one more polynomial-time call by shifting the game by a known additive constant in a way that shifts Shapley values by the same constant on a designated coordinate. Define a modified game

$$\tilde{v}_x(S) := v_x(S) + \lambda \cdot \mathbf{1}\{i \in S\}, \quad (162)$$

where $\lambda > 0$ is known and $\mathbf{1}\{\cdot\}$ is the indicator function. This transformation is computable in polynomial time given oracle access to v_x , and it has a simple Shapley effect: only feature i 's marginal contribution increases by λ across all coalitions, hence

$$\tilde{\phi}_i(x) = \phi_i(x) + \lambda, \quad \tilde{\phi}_k(x) = \phi_k(x) \text{ for } k \neq i. \quad (163)$$

Now apply \mathcal{A} to the shifted instance to obtain

$$\mathcal{A}(\tilde{f}, x, i, j, d_i) = |\tilde{\phi}_i(x)| = |\phi_i(x) + \lambda|. \quad (164)$$

From the pair of values $(|\phi_i(x)|, |\phi_i(x) + \lambda|)$, choosing any λ that is not equal to $2|\phi_i(x)|$ resolves the sign uniquely (because the two absolute values correspond to at most two candidates for $\phi_i(x)$, and the second equation eliminates the spurious one). Since λ is under our control, this can be done with at most a constant number of trials, hence polynomial time overall.

Therefore, a polynomial-time exact ERI-R algorithm implies a polynomial-time algorithm for exact Shapley values, contradicting the #P-hardness of Shapley value computation. Hence computing exact ERI-R for Shapley-based explanations is #P-hard in the worst case. \square

Remark 51 (Practical implication and runtime). The above result concerns the behavior of SHAP-style attributions under feature redundancy and does not rely on computing exact Shapley values. In practice, SHAP is almost always implemented via approximations, including KernelSHAP sampling, TreeSHAP for tree models, and DeepSHAP for deep networks. Accordingly, in ERI-Bench the computational cost of ERI-R is dominated by the chosen SHAP approximation method (here DeepSHAP), rather than by the #P-hard complexity associated with exact Shapley value computation.

O. Tightness of the Lipschitz Stability Bound

The Lipschitz stability bound is used to justify a *linear* relationship between input perturbation magnitude and the worst-case explanation drift. To prevent the bound from being interpreted as merely a loose artifact, we show it is *attainable* (tight) without additional structural assumptions. We give a constructive pair (f, E) achieving equality for all perturbations in a one-dimensional setting, which is sufficient to establish global tightness.

Theorem 52 (Tightness of the Lipschitz Stability Bound). *There exist a predictive model f , an explanation map E , an input x , and a perturbation δ such that*

$$d(E(x), E(x + \delta)) = L_E L \|\delta\|, \quad (165)$$

and hence the Lipschitz stability bound is attained with equality.

Proof. Upper-bounds explanation drift by multiplying two local sensitivity constants: (i) how much the model output can change with the input (captured by L), and (ii) how much the explanation can change with the model output (captured by L_E). To show the bound is *tight*, it suffices to exhibit a setting where both Lipschitz inequalities hold with equality simultaneously and where the chosen distance $d(\cdot, \cdot)$ matches the norm used in the Lipschitz bounds.

Step 1: Choose a model that saturates the L -Lipschitz inequality. Let the input space be \mathbb{R} equipped with the absolute value norm $\|x\| := |x|$, and define the model

$$f(x) := Lx. \quad (166)$$

For any $x_1, x_2 \in \mathbb{R}$, we compute the output difference exactly:

$$\|f(x_1) - f(x_2)\| = |Lx_1 - Lx_2| = L|x_1 - x_2| = L\|x_1 - x_2\|. \quad (167)$$

Therefore f is L -Lipschitz, and moreover the Lipschitz inequality is *tight* (achieved with equality) for every pair (x_1, x_2) .

Step 2: Choose an explanation map that saturates the L_E -Lipschitz inequality. We now define an explainer that is linear in the model output. Let the explanation be scalar-valued and define

$$E(x) := L_E f(x). \quad (168)$$

Equivalently, substituting $f(x) = Lx$ yields

$$E(x) = L_E L x. \quad (169)$$

Let the explanation distance be the absolute difference,

$$d(u, v) := |u - v|. \quad (170)$$

Then for any $x_1, x_2 \in \mathbb{R}$ we have

$$d(E(x_1), E(x_2)) = |L_E f(x_1) - L_E f(x_2)| = L_E |f(x_1) - f(x_2)| = L_E \|f(x_1) - f(x_2)\|. \quad (171)$$

Hence E is L_E -Lipschitz with respect to the model output norm, and again the inequality is *tight* (achieved with equality) for every pair (x_1, x_2) .

Step 3: Evaluate the explanation drift under an input perturbation. Fix any input $x \in \mathbb{R}$ and any perturbation $\delta \in \mathbb{R}$. We compute the drift exactly:

$$d(E(x), E(x + \delta)) = |L_E Lx - L_E L(x + \delta)| = |-L_E L\delta| = L_E L|\delta| = L_E L\|\delta\|. \quad (172)$$

Step 4: Match the result to the bound in Theorem 1. Theorem 1 states (under the same choice of norms/distances) that for any perturbation δ ,

$$d(E(x), E(x + \delta)) \leq L_E L \|\delta\|. \quad (173)$$

Our construction yields equality:

$$d(E(x), E(x + \delta)) = L_E L \|\delta\|. \quad (174)$$

Therefore the bound is tight: without introducing additional structure or stronger assumptions on f or E , the multiplicative constant $L_E L$ cannot be improved in general. \square

Without additional assumptions (e.g., curvature constraints, margin conditions, or structure of E), the Lipschitz stability bound cannot be universally improved.

P. Invariance of ERI Under Monotone Metric Transformations

ERI depends on a chosen distance d on attribution vectors. In many applications, however, only the *ordering* of explainers by reliability matters (e.g., method A is more stable than method B). A common intuition is that if two distances are related by a strictly increasing transformation, then ERI rankings should be preserved up to a monotone rescaling. This is *not* true in general once expectations are taken: for nonlinear increasing g , $\mathbb{E}[g(Z)]$ depends on the full distribution of Z , not only on $\mathbb{E}[Z]$. We therefore state a correct invariance result under *affine* metric transformations, and a separate sample-level monotonicity result that holds for any strictly increasing transformation.

Lemma 3 (Affine Metric Invariance of Drift and ERI). *Let d_1 be a non-negative distance on explanation vectors and define $d_2(a, b) = a_0 d_1(a, b) + b_0$ for constants $a_0 > 0$ and $b_0 \geq 0$. Let the corresponding drifts be*

$$\Delta_k(x) := \mathbb{E}_{\omega \sim \mathcal{D}} [d_k(E(x), E(\mathcal{T}_\omega(x)))], \quad k \in \{1, 2\}.$$

Then

$$\Delta_2(x) = a_0 \Delta_1(x) + b_0. \quad (175)$$

Moreover, for any strictly decreasing function $\psi : [0, \infty) \rightarrow \mathbb{R}$, the reliability scores $R_k(x) := \psi(\Delta_k(x))$ induce the same ordering over methods. In particular, for the canonical bounded ERI mapping $\psi(t) = \frac{1}{1+t}$,

$$\text{ERI}_2(x) = \frac{1}{1 + a_0 \Delta_1(x) + b_0} = \underbrace{\left[t \mapsto \frac{1}{1 + a_0 \left(\frac{1}{t} - 1 \right) + b_0} \right]}_{:= \Psi(\cdot) \text{ strictly increasing on } (0,1]} (\text{ERI}_1(x)), \quad (176)$$

so ERI_2 is a monotone reparameterization of ERI_1 and rankings are preserved.

Proof. Fix an input x and an admissible transformation law $\omega \sim \mathcal{D}$. Define the random explanation pair

$$A(\omega) := E(x), \quad B(\omega) := E(\mathcal{T}_\omega(x)).$$

For $k \in \{1, 2\}$, define the induced drift random variable

$$Z_k(\omega) := d_k(A(\omega), B(\omega)) \geq 0, \quad \Delta_k(x) := \mathbb{E}_{\omega \sim \mathcal{D}}[Z_k(\omega)].$$

Step 1: Drift transforms affinely under affine metric changes. By assumption, the two distances satisfy

$$d_2(a, b) = a_0 d_1(a, b) + b_0, \quad a_0 > 0, b_0 \geq 0.$$

Applying this pointwise to $(A(\omega), B(\omega))$ yields, for every ω ,

$$Z_2(\omega) = d_2(A(\omega), B(\omega)) = a_0 d_1(A(\omega), B(\omega)) + b_0 = a_0 Z_1(\omega) + b_0.$$

Taking expectation w.r.t. $\omega \sim \mathcal{D}$ and using linearity of expectation,

$$\begin{aligned} \Delta_2(x) &= \mathbb{E}[Z_2(\omega)] = \mathbb{E}[a_0 Z_1(\omega) + b_0] \\ &= a_0 \mathbb{E}[Z_1(\omega)] + \mathbb{E}[b_0] = a_0 \Delta_1(x) + b_0, \end{aligned} \tag{177}$$

which proves (175).

Step 2: Any strictly decreasing reparameterization preserves ordering. Let $\psi : (0, \infty) \rightarrow \mathbb{R}$ be strictly decreasing and define $R_k(x) := \psi(\Delta_k(x))$. Consider two methods (or two settings) M and M' with drifts $\Delta_{1,M}(x)$ and $\Delta_{1,M'}(x)$ under d_1 . Since $a_0 > 0$, the affine map $t \mapsto a_0 t + b_0$ is strictly increasing, hence

$$\Delta_{1,M}(x) < \Delta_{1,M'}(x) \iff a_0 \Delta_{1,M}(x) + b_0 < a_0 \Delta_{1,M'}(x) + b_0 \iff \Delta_{2,M}(x) < \Delta_{2,M'}(x).$$

Because ψ is strictly decreasing, it reverses inequalities:

$$\Delta_{2,M}(x) < \Delta_{2,M'}(x) \iff \psi(\Delta_{2,M}(x)) > \psi(\Delta_{2,M'}(x)) \iff R_{2,M}(x) > R_{2,M'}(x).$$

Thus, method rankings induced by R_1 and R_2 are identical (up to the monotone rescaling implied by the affine change of drift).

Step 3: Explicit ERI-to-ERI reparameterization for $\psi(t) = \frac{1}{1+t}$. Now take $\psi(t) = \frac{1}{1+t}$, so

$$\text{ERI}_k(x) = \frac{1}{1 + \Delta_k(x)} \in (0, 1].$$

Using Step 1, we can express ERI_2 as a function of Δ_1 :

$$\text{ERI}_2(x) = \frac{1}{1 + \Delta_2(x)} = \frac{1}{1 + a_0 \Delta_1(x) + b_0}.$$

Next express $\Delta_1(x)$ in terms of $\text{ERI}_1(x)$:

$$\text{ERI}_1(x) = \frac{1}{1 + \Delta_1(x)} \iff 1 + \Delta_1(x) = \frac{1}{\text{ERI}_1(x)} \iff \Delta_1(x) = \frac{1}{\text{ERI}_1(x)} - 1.$$

Substituting into ERI_2 gives the explicit reparameterization:

$$\text{ERI}_2(x) = \frac{1}{1 + a_0 \left(\frac{1}{\text{ERI}_1(x)} - 1 \right) + b_0} =: \Psi(\text{ERI}_1(x)). \tag{178}$$

Finally, Ψ is strictly increasing on $(0, 1]$. To see this, write

$$\Psi(t) = \frac{1}{1 + a_0 \left(\frac{1}{t} - 1 \right) + b_0} = \frac{1}{c + \frac{a_0}{t}}, \quad c := 1 - a_0 + b_0.$$

Since $a_0 > 0$ and $t \mapsto \frac{a_0}{t}$ is strictly decreasing on $(0, 1]$, the denominator $t \mapsto c + \frac{a_0}{t}$ is strictly decreasing, and taking the reciprocal preserves strict order in the opposite direction; hence Ψ is strictly increasing. Equivalently, differentiating yields

$$\Psi'(t) = \frac{a_0}{t^2 \left(c + \frac{a_0}{t} \right)^2} > 0 \quad \text{for all } t \in (0, 1].$$

Therefore ERI_2 is a monotone reparameterization of ERI_1 , and the induced ordering is preserved.

This completes the proof. \square

The restriction to affine transformations is essential: invariance does not hold for general nonlinear monotone reparameterizations of the distance, since expectation does not commute with nonlinear maps.

Lemma 4 (Sample-Level Monotonicity Under Any Strictly Increasing Transform). *Let $g : [0, \infty) \rightarrow [0, \infty)$ be strictly increasing and define $d_2 = g \circ d_1$. Then for any fixed x and any two transformations ω_1, ω_2 ,*

$$d_1(E(x), E(\mathcal{T}_{\omega_1}(x))) < d_1(E(x), E(\mathcal{T}_{\omega_2}(x))) \iff d_2(E(x), E(\mathcal{T}_{\omega_1}(x))) < d_2(E(x), E(\mathcal{T}_{\omega_2}(x))). \quad (179)$$

Proof. Fix an input x and two transformations ω_1, ω_2 . Define the (non-negative) drift values under d_1 as

$$z_1 := d_1(E(x), E(\mathcal{T}_{\omega_1}(x))), \quad z_2 := d_1(E(x), E(\mathcal{T}_{\omega_2}(x))).$$

By definition of $d_2 = g \circ d_1$, we have

$$d_2(E(x), E(\mathcal{T}_{\omega_1}(x))) = g(z_1), \quad d_2(E(x), E(\mathcal{T}_{\omega_2}(x))) = g(z_2).$$

Step 1: Strictly increasing maps preserve and reflect order. Because $g : [0, \infty) \rightarrow [0, \infty)$ is strictly increasing, it is order-preserving and injective on its domain. Concretely, for any $u, v \in [0, \infty)$,

$$u < v \implies g(u) < g(v), \quad (180)$$

and conversely,

$$g(u) < g(v) \implies u < v, \quad (181)$$

since otherwise $u \geq v$ would imply $g(u) \geq g(v)$ by monotonicity, a contradiction.

Step 2: Apply order preservation to the two drifts. Apply (180)–(181) with $u = z_1$ and $v = z_2$. Then

$$z_1 < z_2 \iff g(z_1) < g(z_2).$$

Substituting back the definitions of z_1, z_2 and using $d_2 = g \circ d_1$ yields

$$d_1(E(x), E(\mathcal{T}_{\omega_1}(x))) < d_1(E(x), E(\mathcal{T}_{\omega_2}(x))) \iff d_2(E(x), E(\mathcal{T}_{\omega_1}(x))) < d_2(E(x), E(\mathcal{T}_{\omega_2}(x))),$$

which is exactly (179). \square

Interpretation. Thus, replacing d_1 by any strictly increasing reparameterization $g \circ d_1$ cannot change the *pairwise ordering* of pointwise explanation drifts across transformations. The lemma is purely sample-level and makes no claim about expectations, where nonlinear transforms generally do not commute with $\mathbb{E}[\cdot]$.

Remark (Why nonlinear metric invariance fails in expectation). For nonlinear strictly increasing g , the law-level drift $\Delta_2(x) = \mathbb{E}[g(Z)]$ cannot in general be written as a function of $\Delta_1(x) = \mathbb{E}[Z]$ alone because $\mathbb{E}[g(Z)]$ depends on the full distribution of Z (e.g., by Jensen's inequality). Therefore, ERI invariance under general monotone metric transformations holds *only* at the sample-level (Lemma 4) and is guaranteed at the drift/ERI level only for affine transformations (Lemma 3).

Q. Additional Structural Properties of ERI Computation

The preceding complexity analysis treated each ERI variant separately. However, from an algorithmic perspective, all ERI variants share a common computational structure: they repeatedly evaluate explanations under a family of controlled transformations and aggregate the resulting drift. This subsection formalizes this shared structure and derives three practical properties that strengthen the theoretical completeness of the appendix: (i) an aggregated complexity characterization, (ii) optimal memory usage via streaming computation, and (iii) parallelizability.

Q.0.1. TIME COMPLEXITY ACROSS ERI VARIANTS

Proposition 53 (Aggregated Complexity of ERI Computation). *Let $\{\mathcal{T}_k\}_{k=1}^m$ denote a finite family of transformations (e.g., perturbations, redundancy collapses, time steps, checkpoints, or distributional samples). Assume computing a single explanation $E(\mathcal{T}_k(x))$ costs T_E , and computing the distance between two explanation vectors costs $O(d)$. Then any ERI variant that aggregates drift over these m transformations can be computed in*

$$O(mT_E + md). \quad (182)$$

Proof. The proof follows the ERI-Bench computation pipeline: (i) produce the required explanations, (ii) compute drift distances in attribution space, and (iii) aggregate those drifts into a single ERI score. The key point is that ERI variants differ only in *which* explanations are paired, not in the computational structure of the loop.

Step 1: Reduce ERI computation to a drift-average over m pairs. Any ERI variant in this paper can be written as an average of m scalar drift terms:

$$\widehat{D} = \frac{1}{m} \sum_{k=1}^m d\left(A_k^{(1)}, A_k^{(2)}\right), \quad (183)$$

where $A_k^{(1)}, A_k^{(2)} \in \mathbb{R}^d$ are the two attribution vectors that the metric compares at step k . For example:

$$\begin{aligned} (\text{S}) \quad & (A_k^{(1)}, A_k^{(2)}) = (E(x), E(\mathcal{T}_k(x))), \\ (\text{T}) \quad & (A_k^{(1)}, A_k^{(2)}) = (E(\mathcal{T}_k(x)), E(\mathcal{T}_{k+1}(x))), \end{aligned} \quad (184)$$

and analogous pairings hold for redundancy, checkpoints, and distributional comparisons. The final ERI value is then obtained by a constant-time post-processing of \widehat{D} , e.g.,

$$\widehat{\text{ERI}} = 1 - \frac{\widehat{D}}{\text{Norm}(x) + \epsilon} \quad \text{or} \quad \widehat{\text{ERI}} = 1 - \widehat{D}. \quad (185)$$

Thus, it suffices to bound the cost of computing \widehat{D} .

Step 2: Cost of explanation evaluations is $O(mT_E)$. For each $k \in \{1, \dots, m\}$, at least one explanation vector must be computed. Two common evaluation patterns cover all ERI variants:

(i) Fixed reference explanation. In ERI-S and ERI-R, the pair is $(E(x), E(\mathcal{T}_k(x)))$. If $E(x)$ is cached once, then each step computes only $E(\mathcal{T}_k(x))$, costing T_E per k . Hence:

$$\text{explanation cost} = T_E + mT_E = O(mT_E). \quad (186)$$

(ii) Consecutive-pair explanations. In ERI-T and ERI-M, a typical pair is $(E(\mathcal{T}_k(x)), E(\mathcal{T}_{k+1}(x)))$. Computing the full sequence of required explanations costs $(m+1)T_E$, which is still:

$$(m+1)T_E = O(mT_E). \quad (187)$$

Therefore, across all ERI variants, the total time spent in explanation generation is $O(mT_E)$.

Step 3: Cost of computing drift distances is $O(md)$. Each drift term requires evaluating a distance between two attribution vectors in \mathbb{R}^d :

$$\Delta_k := d(A_k^{(1)}, A_k^{(2)}). \quad (188)$$

By assumption, computing $d(\cdot, \cdot)$ costs $O(d)$ (e.g., ℓ_p norms, cosine distance after dot products and norms, and other coordinate-wise vector dissimilarities). Repeating this for m drift terms yields:

$$\sum_{k=1}^m O(d) = O(md). \quad (189)$$

Step 4: Aggregation and normalization are lower-order terms. The running sum and division by m to obtain \widehat{D} costs $O(m)$ scalar operations:

$$S = \sum_{k=1}^m \Delta_k, \quad \widehat{D} = \frac{S}{m}. \quad (190)$$

The final ERI post-processing (subtracting from 1 and optionally dividing by $\text{Norm}(x) + \epsilon$) costs $O(1)$. Since $O(m) \subseteq O(md)$ whenever $d \geq 1$, these steps do not change the overall complexity.

Step 5: Combine the dominant costs. Summing the dominant contributions from Steps 2 and 3 gives:

$$\text{total time} = O(mT_E) + O(md) = O(mT_E + md), \quad (191)$$

which proves the claim. \square

This proposition shows that ERI scales linearly in the number of transformations evaluated, regardless of whether they correspond to perturbations (ERI-S), redundancy samples (ERI-R), time steps (ERI-T), checkpoints (ERI-M), or distributional draws (ERI-D). The explainer cost T_E dominates in practice, making ERI suitable for deployment whenever explanation computation itself is feasible.

Q.0.2. STREAMING MEMORY COMPLEXITY

Lemma 5 (Streaming Computation of ERI). *All ERI variants can be computed in a single pass using $O(d)$ memory, independent of the number of transformations m .*

Proof. The core observation is that every ERI variant reduces to averaging a sequence of scalar distances between (at most) two attribution vectors at a time. Hence, we never need to store the full history of explanations.

Step 1: Put all ERI variants into a common drift-averaging form. Fix any ERI axis (S, R, T, M, or D). In ERI-Bench, the corresponding empirical drift estimator can always be written as

$$\widehat{D}_m = \frac{1}{m} \sum_{k=1}^m d(A_k^{(1)}, A_k^{(2)}), \quad (192)$$

where $A_k^{(1)}, A_k^{(2)} \in \mathbb{R}^d$ are the two attribution vectors being compared at step k . Concretely:

$$\begin{aligned} \text{ERI-S: } (A_k^{(1)}, A_k^{(2)}) &= (E(x), E(x + \delta_k)), & \text{ERI-R: } (A_k^{(1)}, A_k^{(2)}) &= (E(x), E(x^{(\alpha_k)})), \\ \text{ERI-T: } (A_k^{(1)}, A_k^{(2)}) &= (E(x_k), E(x_{k+1})), & \text{ERI-M: } (A_k^{(1)}, A_k^{(2)}) &= (E_{\theta_k}(x), E_{\theta_{k+1}}(x)), \\ \text{ERI-D: } (A_k^{(1)}, A_k^{(2)}) &= (E(x_k), E(x'_k)), \end{aligned} \quad (193)$$

for suitable sampling choices of δ_k , α_k , checkpoints θ_k , or paired samples (x_k, x'_k) .

Step 2: Define the streaming algorithm as a running-sum estimator. Initialize a scalar accumulator $S \leftarrow 0$. For each step $k = 1, \dots, m$ do:

1. Compute (or load) the two inputs required at step k and evaluate the two explanations $A_k^{(1)}$ and $A_k^{(2)}$.
2. Compute the scalar distance $\Delta_k := d(A_k^{(1)}, A_k^{(2)})$.
3. Update the accumulator $S \leftarrow S + \Delta_k$.

After processing all m steps, output

$$\hat{D}_m = \frac{S}{m}. \quad (194)$$

The corresponding ERI score is then obtained by the same final post-processing used in the batch definition, e.g.,

$$\widehat{\text{ERI}}_m = 1 - \frac{\hat{D}_m}{\text{Norm}(x) + \epsilon}, \quad (195)$$

or $\widehat{\text{ERI}}_m = 1 - \hat{D}_m$ when a bounded/clamped distance is used.

Step 3: Correctness: streaming and batch computation coincide exactly. Let $\Delta_k := d(A_k^{(1)}, A_k^{(2)})$. The batch estimator is

$$\hat{D}_m^{\text{batch}} = \frac{1}{m} \sum_{k=1}^m \Delta_k. \quad (196)$$

The streaming update maintains the invariant

$$S_k = \sum_{r=1}^k \Delta_r, \quad (197)$$

where S_k is the accumulator after k steps. This follows by induction:

$$S_k = S_{k-1} + \Delta_k = \sum_{r=1}^{k-1} \Delta_r + \Delta_k = \sum_{r=1}^k \Delta_r. \quad (198)$$

At termination, $S_m = \sum_{k=1}^m \Delta_k$, hence

$$\hat{D}_m^{\text{stream}} = \frac{S_m}{m} = \frac{1}{m} \sum_{k=1}^m \Delta_k = \hat{D}_m^{\text{batch}}. \quad (199)$$

Because ERI is computed by applying a deterministic transformation to \hat{D}_m (e.g., normalization and subtraction from 1), the resulting ERI value is identical under streaming and batch computation.

Step 4: Memory bound is $O(d)$ and does not depend on m . At any step k , the streaming procedure needs to store:

- the current pair of attribution vectors $A_k^{(1)}$ and $A_k^{(2)}$, each in \mathbb{R}^d , and
- a constant number of scalars (the accumulator S and, optionally, $\text{Norm}(x)$ and ϵ).

Thus the memory footprint is

$$O(d) + O(d) + O(1) = O(d), \quad (200)$$

independent of the number of transformations m .

Since every ERI variant admits the drift-averaging representation and the average can be accumulated online without storing past explanations, all ERI variants are computable in a single pass with $O(d)$ memory. This completes the proof. \square

ERI can be computed online, in a streaming fashion, with constant memory in the number of perturbations or time steps. This property is critical for long sequences (ERI-T), large Monte Carlo budgets (ERI-S, ERI-D), or embedded and edge deployments.

Q.0.3. PARALLELIZATION PROPERTIES

Proposition 54 (Embarrassingly Parallel ERI Computation). *Let T_E denote the time required to compute a single explanation vector $E(x)$ and let d be the attribution dimension. Consider ERI-S, ERI-M, or ERI-D computed using m independent explanation calls and m corresponding distance evaluations. With p parallel workers, the wall-clock time is*

$$T_{\text{wall}}(m, p) = O\left(\frac{m}{p}T_E + md\right), \quad (201)$$

up to negligible synchronization overhead.

Proof. We prove the claim by explicitly separating (i) the explanation-evaluation stage and (ii) the drift-aggregation stage, and then showing that the dominant stage is embarrassingly parallel.

Step 1: ERI-S/ERI-M/ERI-D share the same computational template. For each of the three metrics, the computation consists of evaluating explanations on a collection of transformed inputs (or checkpoints) and then aggregating the resulting distances.

ERI-S (perturbations). Let $\delta_1, \dots, \delta_m$ be i.i.d. perturbations and define

$$x^{(k)} := x + \delta_k, \quad A^{(k)} := E(x^{(k)}), \quad A^{(0)} := E(x). \quad (202)$$

The empirical drift is

$$\hat{D}_S = \frac{1}{m} \sum_{k=1}^m d(A^{(0)}, A^{(k)}). \quad (203)$$

ERI-M (checkpoints). Let $\theta_1, \dots, \theta_m$ be checkpoints and define

$$A^{(k)} := E_{\theta_k}(x). \quad (204)$$

A standard ERI-M drift is computed from consecutive pairs:

$$\hat{D}_M = \frac{1}{m-1} \sum_{k=1}^{m-1} d(A^{(k)}, A^{(k+1)}). \quad (205)$$

ERI-D (two distributions). Let $x^{(1)}, \dots, x^{(m)} \sim \mathcal{P}$ and $x'^{(1)}, \dots, x'^{(m)} \sim \mathcal{P}'$. Define

$$A^{(k)} := E(x^{(k)}), \quad A'^{(k)} := E(x'^{(k)}). \quad (206)$$

A simple empirical distributional drift (e.g. mean pairing) takes the form

$$\hat{D}_D = \frac{1}{m} \sum_{k=1}^m d(A^{(k)}, A'^{(k)}). \quad (207)$$

In all cases, the dominant work is a batch of m explanation evaluations plus $O(m)$ distance computations on d -dimensional vectors.

Step 2: Independence implies embarrassingly parallel explanation calls. We now formalize the crucial structural property: each explanation call is a self-contained computation that does not require outputs of any other call.

For ERI-S, conditional on the sampled perturbations $\{\delta_k\}_{k=1}^m$, each attribution vector

$$A^{(k)} = E(x + \delta_k) \quad (208)$$

depends only on (x, δ_k) and the fixed explainer E . Thus, for distinct indices $k \neq k'$, the computations of $A^{(k)}$ and $A^{(k')}$ have no data dependency and can be executed concurrently.

For ERI-D, conditional on the sampled pairs $\{(x^{(k)}, x'^{(k)})\}_{k=1}^m$, each distance term depends only on the pairwise explanations

$$d(E(x^{(k)}), E(x'^{(k)})), \quad (209)$$

and these pairs are independent across k in the sense of computation: no term requires any other term.

For ERI-M, while the drift uses consecutive distances $d(A^{(k)}, A^{(k+1)})$, the explanation evaluations $A^{(1)}, \dots, A^{(m)}$ are still independent in the computational sense: each $A^{(k)}$ is obtained by running the explainer at checkpoint θ_k on the same fixed input x , and does not require any other checkpoint output. Hence the expensive stage—computing the $A^{(k)}$ —is embarrassingly parallel.

Step 3: Parallel scheduling yields a $\frac{m}{p}$ factor in wall-clock time. Assign the m explanation evaluations to p workers using any balanced static schedule (e.g. round-robin or contiguous blocks). Each worker executes at most $\lceil m/p \rceil$ explanation calls. Since each call costs at most T_E , the wall-clock time for the explanation stage is

$$T_{\text{explain}}(m, p) = O\left(\left\lceil \frac{m}{p} \right\rceil T_E\right) = O\left(\frac{m}{p} T_E\right). \quad (210)$$

Step 4: Distance aggregation adds an $O(md)$ term. After explanations are computed, ERI requires evaluating and aggregating m (or $m-1$) distances between attribution vectors in \mathbb{R}^d . For standard choices such as ℓ_p or cosine distance, each distance computation is linear in the dimension:

$$T_{\text{dist}}(m) = O(md). \quad (211)$$

This aggregation can also be parallelized, but it is typically memory-bound and often dominated by the explanation stage when $T_E \gg d$. We therefore include it explicitly as an additive term.

Step 5: Combine stages and account for synchronization. Combining the explanation-evaluation time and the aggregation time gives

$$T_{\text{wall}}(m, p) = O\left(\frac{m}{p} T_E\right) + O(md) = O\left(\frac{m}{p} T_E + md\right). \quad (212)$$

Finally, synchronization overhead is negligible because only a single reduction operation (summing m scalar distances) is required at the end, and no barrier is needed during explanation computation. This completes the proof. \square

ERI scales almost linearly with available compute. On modern GPU or distributed systems, ERI-S and ERI-D can be evaluated with hundreds or thousands of perturbations at nearly the cost of a single explanation pass. Together, Propositions 53, 54, and Lemma 5 show that ERI is not only theoretically principled but also *computationally practical*:

- linear-time in the number of transformations,
- constant-memory in streaming settings,
- and trivially parallelizable.

These properties distinguish ERI from perturbation-heavy explainers whose computational cost grows superlinearly or requires storing large attribution ensembles.

R. Axiomatic Analysis of Common Explainers (A1–A4)

This section provides a formal axiomatic analysis of widely used explanation methods with respect to the four ERI axioms introduced in Section 5. The goal is not to rank explainers, but to rigorously characterize which axioms each explainer can satisfy, which axioms it provably violates, and under what additional assumptions partial compliance may be recovered.

A key nuance is that axioms A1–A4 are properties of an explanation map $E_\theta(\cdot)$ together with a choice of perturbation operator, redundancy-collapse operator, model-evolution trajectory, and (where applicable) background or reference distributions. Accordingly, our results are stated as *general theorems*, *counterexamples* (impossibility results), and *conditional guarantees*.

Explainer	A1 Perturbation stability	A2 Redundancy-collapse	A3 Model-evolution	A4 Distributional robustness
Integrated Gradients (IG)	✓ (if gradients bounded / smooth path)	▲ / ✗ (can fail with correlated or redundant features)	✓ (if model and gradients vary smoothly in θ)	✓ (if $\delta \mapsto E(x + \delta)$ is integrable and continuous)
DeepLIFT	✓ (piecewise-linear networks; stable away from kinks)	▲ / ✗ (fails under redundancy unless special symmetry)	✓ (if activations and reference remain stable across θ)	✓ (under the same integrability conditions)
DeepSHAP (approx. SHAP)	✓ (if the DeepSHAP estimator is continuous)	✗ in general (redundancy asymmetry persists under correlated features)	▲ (depends on how the background distribution evolves)	▲ (strong dependence on background distribution)
Permutation importance	✓ (risk functional; smooth if model output is smooth)	▲ / ✗ (correlated features can share or steal importance)	✓ (if model predictions vary smoothly in θ)	✓ (under standard concentration and continuity of risk)
Mutual Information (MI)	✓ (continuous under small perturbations if density is regular)	✗ (marginal dependence does not collapse redundancy)	▲ (can be stable but not consistent across checkpoints)	✓ (weak continuity under regularity; estimator issues remain)
HSIC	✓ (kernel smoothness implies continuity)	✗ (marginal dependence; redundancy can inflate scores)	▲ (same issues as MI)	✓ (continuous in distribution under bounded kernels)
GradCAM++	▲ (unstable near ReLU / argmax regions)	✗ (not feature-based; redundancy notion mismatched)	▲ (sensitive to small parameter changes)	▲
Random explanations	▲ (degenerate stability; uninformative)	✗ (no collapse structure)	▲ (trivially stable if independent of θ)	✓ (distribution fixed; semantically meaningless)
MCIR	✓	✓	✓	✓

Table 10. Summary of which axioms hold, fail, or depend on conventions. Legend: ✓ = holds under standard regularity assumptions; ✗ = provably fails in general; ▲ = conditional or degenerate (depends on conventions, estimators, or lacks faithfulness).

R.1. Summary of Axiom Compliance

Table 10 summarizes the conclusions proven below. Symbols have the following meaning: ✓ denotes satisfaction under standard smoothness and boundedness assumptions; ✗ denotes provable failure in general (existence of a counterexample); ○ denotes conditional satisfaction under additional symmetry, smoothing, or modeling assumptions.

We now justify each entry with formal arguments.

Proposition 55 (IG satisfies perturbation stability (A1)). *Assume f is continuously differentiable in a neighborhood of x and that $\nabla_x f$ is locally Lipschitz. Then Integrated Gradients satisfies Axiom A1.*

Proof. Fix a baseline x_0 and define the straight-line path

$$\gamma_x(\alpha) := x_0 + \alpha(x - x_0), \quad \alpha \in [0, 1]. \quad (213)$$

Write the Integrated Gradients explanation as the vector-valued map

$$\text{IG}(x) := (x - x_0) \odot \int_0^1 \nabla f(\gamma_x(\alpha)) d\alpha, \quad (214)$$

where \odot denotes componentwise multiplication. Equivalently, for each coordinate i ,

$$\text{IG}_i(x) = (x_i - x_{0,i}) \int_0^1 \frac{\partial f(\gamma_x(\alpha))}{\partial x_i} d\alpha. \quad (215)$$

Let δ be such that both x and $x + \delta$ remain in a neighborhood U on which ∇f is Lipschitz with constant L , i.e.,

$$\|\nabla f(u) - \nabla f(v)\| \leq L\|u - v\|, \quad \forall u, v \in U. \quad (216)$$

For each $\alpha \in [0, 1]$, the two path points satisfy

$$\gamma_{x+\delta}(\alpha) - \gamma_x(\alpha) = \alpha\delta, \quad (217)$$

so, by Lipschitzness of ∇f ,

$$\|\nabla f(\gamma_{x+\delta}(\alpha)) - \nabla f(\gamma_x(\alpha))\| \leq L\|\alpha\delta\| \leq L\|\delta\|. \quad (218)$$

Define the averaged gradients

$$G(x) := \int_0^1 \nabla f(\gamma_x(\alpha)) d\alpha. \quad (219)$$

Then

$$\text{IG}(x) = (x - x_0) \odot G(x). \quad (220)$$

We decompose

$$\begin{aligned} \text{IG}(x + \delta) - \text{IG}(x) &= ((x + \delta - x_0) \odot G(x + \delta)) - ((x - x_0) \odot G(x)) \\ &= \delta \odot G(x + \delta) + (x - x_0) \odot (G(x + \delta) - G(x)). \end{aligned} \quad (221)$$

Taking norms and using the triangle inequality yields

$$\|\text{IG}(x + \delta) - \text{IG}(x)\| \leq \|\delta \odot G(x + \delta)\| + \|(x - x_0) \odot (G(x + \delta) - G(x))\|. \quad (222)$$

For the first term, use $\|\delta \odot v\| \leq \|\delta\| \|v\|$:

$$\|\delta \odot G(x + \delta)\| \leq \|\delta\| \|G(x + \delta)\|. \quad (223)$$

Since ∇f is continuous and $[0, 1]$ is compact, $\|\nabla f(\gamma_{x+\delta}(\alpha))\|$ is bounded on $\alpha \in [0, 1]$ for all $x + \delta$ in a small ball around x . Thus there exists $M < \infty$ such that

$$\|G(x + \delta)\| = \left\| \int_0^1 \nabla f(\gamma_{x+\delta}(\alpha)) d\alpha \right\| \leq \int_0^1 \|\nabla f(\gamma_{x+\delta}(\alpha))\| d\alpha \leq M. \quad (224)$$

Hence

$$\|\delta \odot G(x + \delta)\| \leq M\|\delta\|. \quad (225)$$

For the second term, again use $\|u \odot v\| \leq \|u\| \|v\|$:

$$\|(x - x_0) \odot (G(x + \delta) - G(x))\| \leq \|x - x_0\| \|G(x + \delta) - G(x)\|. \quad (226)$$

Moreover,

$$\begin{aligned} \|G(x + \delta) - G(x)\| &= \left\| \int_0^1 (\nabla f(\gamma_{x+\delta}(\alpha)) - \nabla f(\gamma_x(\alpha))) d\alpha \right\| \\ &\leq \int_0^1 \|\nabla f(\gamma_{x+\delta}(\alpha)) - \nabla f(\gamma_x(\alpha))\| d\alpha \\ &\leq \int_0^1 L\alpha\|\delta\| d\alpha = \frac{L}{2}\|\delta\|. \end{aligned} \quad (227)$$

Therefore,

$$\|(x - x_0) \odot (G(x + \delta) - G(x))\| \leq \frac{L}{2}\|x - x_0\| \|\delta\|. \quad (228)$$

Combining the bounds gives

$$\|\text{IG}(x + \delta) - \text{IG}(x)\| \leq \left(M + \frac{L}{2}\|x - x_0\| \right) \|\delta\| = C\|\delta\| \quad (229)$$

for $C := M + \frac{L}{2} \|x - x_0\|$ and all sufficiently small δ . Thus IG is locally Lipschitz at x , hence continuous at x , and

$$\lim_{\delta \rightarrow 0} \|\text{IG}(x + \delta) - \text{IG}(x)\| = 0. \quad (230)$$

If the explanation distance is defined as $d(E(x), E(x + \delta)) := \|E(x) - E(x + \delta)\|$ (or is upper bounded by a constant multiple of this norm), then

$$d(E(x), E(x + \delta)) \rightarrow 0 \quad \text{as } \delta \rightarrow 0, \quad (231)$$

which is exactly Axiom A1. \square

Proposition 56 (IG satisfies A3 and A4 under smoothness). *If $\nabla_x f_\theta$ is Lipschitz in θ and $d(E(x), E(x + \delta))$ is dominated by an integrable envelope in δ , then IG satisfies Axioms A3 and A4.*

Proof. **Step 1 (Parameter-indexed IG map).** Fix a baseline x_0 and define, for each parameter θ , the IG explanation

$$\text{IG}_\theta(x) := (x - x_0) \odot \int_0^1 \nabla_x f_\theta(x_0 + \alpha(x - x_0)) d\alpha. \quad (232)$$

Let $\gamma_x(\alpha) = x_0 + \alpha(x - x_0)$ as before.

Step 2 (A3: continuity in parameters). Assume $\nabla_x f_\theta(u)$ is Lipschitz in θ (uniformly over u in a neighborhood containing the IG path), meaning that there exists $K > 0$ such that

$$\|\nabla_x f_{\theta_1}(u) - \nabla_x f_{\theta_2}(u)\| \leq K \|\theta_1 - \theta_2\|, \quad \forall u \in \Gamma, \quad (233)$$

where $\Gamma := \{\gamma_x(\alpha) : \alpha \in [0, 1]\}$ (or a small tube around it). Then

$$\begin{aligned} \|\text{IG}_{\theta_1}(x) - \text{IG}_{\theta_2}(x)\| &= \left\| (x - x_0) \odot \int_0^1 (\nabla_x f_{\theta_1}(\gamma_x(\alpha)) - \nabla_x f_{\theta_2}(\gamma_x(\alpha))) d\alpha \right\| \\ &\leq \|x - x_0\| \int_0^1 \|\nabla_x f_{\theta_1}(\gamma_x(\alpha)) - \nabla_x f_{\theta_2}(\gamma_x(\alpha))\| d\alpha \\ &\leq \|x - x_0\| \int_0^1 K \|\theta_1 - \theta_2\| d\alpha \\ &= K \|x - x_0\| \|\theta_1 - \theta_2\|. \end{aligned} \quad (234)$$

Hence $\theta \mapsto \text{IG}_\theta(x)$ is Lipschitz, therefore continuous. Consequently, if the metric d is the explanation norm distance (or is bounded by a constant multiple of it), we obtain

$$d(E_{\theta_1}(x), E_{\theta_2}(x)) \rightarrow 0 \quad \text{as } \theta_1 \rightarrow \theta_2, \quad (235)$$

which gives Axiom A3.

Step 3 (A4: commutation of limit/expectation over perturbations). Let δ be a random perturbation with law \mathcal{D} . Define the random variable

$$Z(\delta) := d(E(x), E(x + \delta)), \quad (236)$$

where $E(\cdot) = \text{IG}_\theta(\cdot)$ for fixed θ (or the proposition's chosen setting). Assume there exists an envelope $g(\delta) \geq 0$ such that

$$Z(\delta) \leq g(\delta) \quad \text{for all relevant } \delta, \quad (237)$$

and g is integrable under \mathcal{D} , i.e.,

$$\mathbb{E}_{\delta \sim \mathcal{D}}[g(\delta)] < \infty. \quad (238)$$

From the perturbation stability in A1 (already established under the stated smoothness assumptions), we have pointwise convergence

$$Z(\delta) \rightarrow 0 \quad \text{as } \delta \rightarrow 0. \quad (239)$$

Consider a sequence of perturbation distributions \mathcal{D}_n that concentrate at 0 (or equivalently a scaling $\delta_n \rightarrow 0$ in probability). Then $Z(\delta_n) \rightarrow 0$ almost surely along a subsequence, and by dominated convergence (using g as a dominating function),

$$\lim_{n \rightarrow \infty} \mathbb{E}[Z(\delta_n)] = \mathbb{E} \left[\lim_{n \rightarrow \infty} Z(\delta_n) \right] = 0. \quad (240)$$

This is precisely the expectation-stability requirement captured by Axiom A4, namely that the expected explanation drift vanishes as the perturbation level vanishes, and that the limit and expectation can be interchanged under the integrable domination assumption.

The Lipschitz-in- θ control yields A3, and the dominated convergence argument yields A4 under the stated envelope condition. \square

Proposition 57 (Conditional compliance of IG with A2). *If the model is permutation-symmetric in redundant features and the baseline and integration path are chosen symmetrically, then IG satisfies Axiom A2.*

Proof. Let $R \subseteq \{1, \dots, d\}$ be a set of redundant features. A permutation π of coordinates is said to be an R -permutation if it only permutes indices inside R and leaves all coordinates outside R unchanged. Define the associated permutation operator P_π acting on vectors by reindexing coordinates: $(P_\pi x)_i := x_{\pi(i)}$. Permutation symmetry of the model in the redundant block means that for every R -permutation π and every input x in the domain of interest, $f(P_\pi x) = f(x)$. Assume the baseline is symmetric on the redundant block, i.e., $(P_\pi x_0) = x_0$ for all R -permutations π . For standard Integrated Gradients the path is the straight line $\gamma_x(\alpha) := x_0 + \alpha(x - x_0)$, $\alpha \in [0, 1]$. This path is compatible with permutations in the sense that

$$\gamma_{P_\pi x}(\alpha) = x_0 + \alpha(P_\pi x - x_0) = x_0 + \alpha(P_\pi x - P_\pi x_0) = P_\pi(x_0 + \alpha(x - x_0)) = P_\pi \gamma_x(\alpha). \quad (241)$$

Thus permuting the input corresponds to permuting the entire IG path pointwise.

Define $g(x) := f(P_\pi x) - f(x)$. By symmetry, $g(x) \equiv 0$ for all x , and hence $\nabla g(x) = 0$ for all x . Using the chain rule for the linear map P_π , we obtain

$$\nabla_x f(P_\pi x) = P_\pi \nabla_x f(x), \quad (242)$$

where P_π on the right-hand side permutes gradient coordinates in the same way it permutes input coordinates. In particular, along the path,

$$\nabla_x f(\gamma_{P_\pi x}(\alpha)) = \nabla_x f(P_\pi \gamma_x(\alpha)) = P_\pi \nabla_x f(\gamma_x(\alpha)). \quad (243)$$

Write IG in vector form:

$$\text{IG}(x) := (x - x_0) \odot \int_0^1 \nabla_x f(\gamma_x(\alpha)) d\alpha. \quad (244)$$

For the permuted input $P_\pi x$, using the previous identities,

$$\begin{aligned} \text{IG}(P_\pi x) &= (P_\pi x - x_0) \odot \int_0^1 \nabla_x f(\gamma_{P_\pi x}(\alpha)) d\alpha = (P_\pi(x - x_0)) \odot \int_0^1 P_\pi \nabla_x f(\gamma_x(\alpha)) d\alpha \\ &= P_\pi \left((x - x_0) \odot \int_0^1 \nabla_x f(\gamma_x(\alpha)) d\alpha \right) = P_\pi \text{IG}(x). \end{aligned}$$

Now consider the redundancy-collapse regime where all redundant coordinates are equal and collapse to a common value: $x_i = x_j$ for all $i, j \in R$, $x_{0,i} = x_{0,j}$ for all $i, j \in R$. Then $P_\pi x = x$ for every R -permutation π . Plugging into the equivariance identity yields

$$\text{IG}(x) = \text{IG}(P_\pi x) = P_\pi \text{IG}(x), \quad (245)$$

meaning $\text{IG}(x)$ is invariant under any permutation of the redundant coordinates. The only vectors invariant under all permutations inside R are those that are constant on R . Hence

$$\text{IG}_i(x) = \text{IG}_j(x) \quad \text{for all } i, j \in R. \quad (246)$$

Axiom A2 requires that, under redundancy collapse, the explanation also collapses consistently, typically meaning that redundant coordinates receive equal attribution (and thus the explanation is invariant to how the redundant coordinates are labeled). The equality established above gives exactly this collapse-consistent behavior. Therefore, under permutation symmetry of f and symmetric baseline/path choices, IG satisfies Axiom A2. \square

Proposition 58 (IG satisfies A3 and A4 under smoothness). *If $\nabla_x f_\theta$ is Lipschitz in θ and $d(E(x), E(x + \delta))$ is dominated by an integrable envelope in δ , then IG satisfies Axioms A3 and A4.*

Proof. Fix a baseline x_0 and define the straight-line path

$$\gamma_x(\alpha) := x_0 + \alpha(x - x_0), \quad \alpha \in [0, 1]. \quad (247)$$

For each parameter value θ , define the IG explanation map

$$E_\theta(x) := \text{IG}_\theta(x) := (x - x_0) \odot \int_0^1 \nabla_x f_\theta(\gamma_x(\alpha)) d\alpha. \quad (248)$$

Axiom A3 concerns continuity (or stability) of $E_\theta(x)$ with respect to θ , while Axiom A4 concerns passing limits through expectations over small perturbations δ . Assume $\nabla_x f_\theta$ is Lipschitz in θ uniformly along the IG path, meaning that there exists $K > 0$ such that for all θ, θ' and all $\alpha \in [0, 1]$,

$$\|\nabla_x f_\theta(\gamma_x(\alpha)) - \nabla_x f_{\theta'}(\gamma_x(\alpha))\| \leq K\|\theta - \theta'\|. \quad (249)$$

Then,

$$\begin{aligned} \|E_\theta(x) - E_{\theta'}(x)\| &= \left\| (x - x_0) \odot \int_0^1 (\nabla_x f_\theta(\gamma_x(\alpha)) - \nabla_x f_{\theta'}(\gamma_x(\alpha))) d\alpha \right\| \\ &\leq \|x - x_0\| \int_0^1 \|\nabla_x f_\theta(\gamma_x(\alpha)) - \nabla_x f_{\theta'}(\gamma_x(\alpha))\| d\alpha \\ &\leq \|x - x_0\| \int_0^1 K\|\theta - \theta'\| d\alpha \\ &= K\|x - x_0\| \|\theta - \theta'\|. \end{aligned} \quad (250)$$

Hence $E_\theta(x)$ is Lipschitz in θ and therefore continuous in θ . If Axiom A3 is formulated using the explanation distance d and d is the norm distance or is dominated by a constant multiple of it, then

$$d(E_\theta(x), E_{\theta'}(x)) \rightarrow 0 \quad \text{as } \theta' \rightarrow \theta, \quad (251)$$

which establishes Axiom A3. Let δ be a random perturbation and consider the random drift

$$Z(\delta) := d(E_\theta(x), E_\theta(x + \delta)). \quad (252)$$

Assume that (i) $Z(\delta) \rightarrow 0$ as $\delta \rightarrow 0$ pointwise, and (ii) there exists a measurable envelope $g(\delta) \geq 0$ such that $Z(\delta) \leq g(\delta)$ and, $\mathbb{E}[g(\delta)] < \infty$. Let $\{\delta_n\}$ be a sequence of perturbations with $\delta_n \rightarrow 0$ in probability (for example $\delta_n = \sigma_n \varepsilon$ with $\sigma_n \rightarrow 0$ and fixed noise ε). Under the pointwise convergence and domination, the dominated convergence theorem yields

$$\lim_{n \rightarrow \infty} \mathbb{E}[Z(\delta_n)] = \mathbb{E} \left[\lim_{n \rightarrow \infty} Z(\delta_n) \right] = 0. \quad (253)$$

Therefore the expected explanation drift vanishes as the perturbation level vanishes, and the limit can be interchanged with expectation under the stated integrable envelope condition, which is the content of Axiom A4. Uniform Lipschitzness of $\nabla_x f_\theta$ in θ along the IG path implies A3, and the integrable domination condition implies A4 via dominated convergence. \square

R.2. DeepLIFT

Proposition 59. *DeepLIFT satisfies A1, A3, and A4 away from activation-boundary transitions, but violates A2 in general.*

Proof. Fix a reference input x_0 . In DeepLIFT, each unit u is assigned a reference activation u_0 obtained by forwarding x_0 through the network, and the method propagates contribution scores that decompose the output difference $\Delta y := f(x) - f(x_0)$ into input-wise attributions. In common DeepLIFT formulations (e.g., Rescale or RevealCancel rules), the backward multipliers at each layer are functions of differences $\Delta u := u - u_0$ and ratios of differences when denominators are nonzero. For networks with piecewise-linear components (ReLU, max-pooling, linear layers), the forward map $x \mapsto f(x)$ is piecewise affine, and for a fixed pattern of active/inactive units, the network reduces to an affine map $f(x) = Ax + b$ in a neighborhood that stays within the same activation regime. In the same regime, the DeepLIFT rules reduce to linear propagation of Δy through fixed local multipliers, so the resulting explanation map can be written as

$$E(x) := \text{DeepLIFT}(x) = M(x - x_0) \quad (254)$$

for a matrix M that is constant as long as the activation regime does not change. Assume x lies in the interior of an activation region, so there exists $\rho > 0$ such that for all δ with $\|\delta\| < \rho$, the activation regime is unchanged. Then M is constant on $B(x, \rho)$ and,

$$E(x + \delta) - E(x) = M((x + \delta - x_0) - (x - x_0)) = M\delta. \quad (255)$$

Hence, $\|E(x + \delta) - E(x)\| \leq \|M\| \|\delta\|$, so E is locally Lipschitz at x and, $d(E(x), E(x + \delta)) \rightarrow 0$ as $\delta \rightarrow 0$, which is Axiom A1 (for d given by the explanation norm, or dominated by it). Let the model depend on parameters θ and denote by $E_\theta(x)$ the DeepLIFT explanation. Fix (x, θ) such that in a neighborhood of θ the activation regime induced by (x, x_0) does not change. In that neighborhood the explanation remains linear in $(x - x_0)$ with a matrix M_θ determined by the layer-wise weights and fixed gating pattern: $E_\theta(x) = M_\theta(x - x_0)$. Assume that $\theta \mapsto M_\theta$ is continuous (or Lipschitz) on this neighborhood, which holds when the regime is fixed because M_θ is a composition of additions and multiplications of the weights, and any DeepLIFT rule ratios remain well-defined away from $\Delta u = 0$ boundaries. Then

$$\|E_{\theta_1}(x) - E_{\theta_2}(x)\| = \|(M_{\theta_1} - M_{\theta_2})(x - x_0)\| \leq \|M_{\theta_1} - M_{\theta_2}\| \|x - x_0\|. \quad (256)$$

Thus $E_\theta(x)$ is continuous in θ (locally Lipschitz if M_θ is), and therefore

$$d(E_{\theta_1}(x), E_{\theta_2}(x)) \rightarrow 0 \quad \text{as } \theta_2 \rightarrow \theta_1, \quad (257)$$

which is Axiom A3. Let δ be a random perturbation (or drawn from a family of shrinking noise laws). Consider

$$Z(\delta) := d(E(x), E(x + \delta)). \quad (258)$$

Within the fixed regime ball $B(x, \rho)$, we have $E(x + \delta) - E(x) = M\delta$ and hence $Z(\delta) \leq c\|M\| \|\delta\|$ for some $c > 0$ depending on how d relates to the norm. If $\mathbb{E}[\|\delta\|]$ is finite and δ is restricted (or tends) to stay within $B(x, \rho)$ with probability approaching 1, then the right-hand side is integrable and provides an envelope. Moreover, by A1 we have $Z(\delta) \rightarrow 0$ as $\delta \rightarrow 0$ pointwise. Hence dominated convergence yields

$$\lim_{\sigma \rightarrow 0} \mathbb{E}[Z(\delta_\sigma)] = \mathbb{E} \left[\lim_{\sigma \rightarrow 0} Z(\delta_\sigma) \right] = 0, \quad (259)$$

which matches Axiom A4. Axiom A2 requires redundancy-collapse consistency: if two (or more) features are redundant and collapse to an identical representation, the explanation should collapse accordingly (typically implying equal attributions for the redundant features in the collapse limit). DeepLIFT does not, in general, enforce such symmetry because its multipliers depend on the learned weights connected to each feature and on the specific computational graph paths from each feature to the output. A concrete counterexample can be given with a linear model (which is a valid piecewise-linear regime) with redundant features:

$$f(x_1, x_2) = w_1 x_1 + w_2 x_2, \quad w_1 \neq w_2, \quad (260)$$

and a reference $x_0 = 0$. DeepLIFT reduces to the exact difference decomposition

$$E_1(x) = w_1(x_1 - 0), \quad E_2(x) = w_2(x_2 - 0). \quad (261)$$

Under redundancy collapse $x_1 = x_2$, the attributions satisfy, $E_1(x) : E_2(x) = w_1 : w_2$, so they are not forced to become equal. Therefore the explanation does not converge to a collapsed, permutation-invariant attribution on the redundant block unless additional architectural or weight symmetry constraints are imposed. This violates Axiom A2 in general, while it may hold conditionally for symmetric architectures and symmetric parameterizations. \square

R.3. SHAP (Shapley-Based Explanations)

Proposition 60 (SHAP violates redundancy-collapse consistency). *Exact Shapley-based explanations violate Axiom A2 in general.*

Proof. Fix an input $x \in \mathbb{R}^d$ and a value function $v_x(S)$ defined for coalitions $S \subseteq [d]$ (e.g., by conditional expectations). The Shapley value for feature i is

$$\phi_i(x) = \sum_{S \subseteq [d] \setminus \{i\}} \frac{|S|!(d - |S| - 1)!}{d!} (v_x(S \cup \{i\}) - v_x(S)). \quad (262)$$

Equivalently, if Π is a uniformly random permutation of $[d]$ and $\text{Pre}_\Pi(i)$ denotes the set of features preceding i in Π , then

$$\phi_i(x) = \mathbb{E}_\Pi \left[v_x(\text{Pre}_\Pi(i) \cup \{i\}) - v_x(\text{Pre}_\Pi(i)) \right]. \quad (263)$$

Thus $\phi_i(x)$ depends on how adding feature i changes the model value under the completion rule encoded by $v_x(\cdot)$. Axiom A2 requires that when features become redundant and collapse to an indistinguishable representation, their explanations converge to a collapsed explanation (in particular, redundant features should become exchangeable in the limit, which typically forces their attributions to match in the limit).

However, Shapley attributions depend on the *marginal contribution* of each feature relative to a coalition completion operator. When two features are highly correlated but not perfectly identical, the conditional expectations used in $v_x(S)$ can behave differently depending on whether i or j is included in S , especially in nonlinear models with interactions. This creates persistent differences in marginal contributions that need not vanish as correlation tends to 1. Consider a redundancy-generating model where feature x_j is obtained from x_i by

$$x_j = \alpha x_i + \sqrt{1 - \alpha^2} Z, \quad (264)$$

where Z is an independent noise variable with $\mathbb{E}[Z] = 0$ and $\mathbb{E}[Z^2] = 1$, and $\alpha \in (0, 1)$. Then

$$\text{Corr}(x_i, x_j) = \alpha, \quad (265)$$

so $\alpha \rightarrow 1$ corresponds to the redundancy-collapse limit. Let the model be nonlinear with an interaction that is sensitive to the two coordinates, for instance a smooth function with mixed dependence such as

$$f(x_i, x_j) = h(x_i) + h(x_j) + \lambda q(x_i, x_j), \quad (266)$$

where h is smooth, $\lambda \neq 0$, and q is a smooth interaction term that is not additive-separable, e.g.,

$$q(x_i, x_j) = x_i x_j \quad (267)$$

or a bounded smooth surrogate thereof. Under standard SHAP definitions, $v_x(S)$ involves conditional expectations of f given subsets of coordinates. For coalitions that do not contain i (or j), terms like

$$\mathbb{E}[q(x_i, x_j) \mid x_S] \quad (268)$$

depend on the conditional distribution of the missing variables. In the above redundancy model, the conditional laws of x_i given x_j and of x_j given x_i can differ in how the residual noise Z enters, and the interaction term q converts these residual differences into different conditional expectations.

As a result, there exist inputs x and coalitions S such that the marginal contribution terms satisfy

$$(v_x(S \cup \{i\}) - v_x(S)) - (v_x(S \cup \{j\}) - v_x(S)) \neq 0 \quad (269)$$

even for α arbitrarily close to 1. Averaging these non-vanishing differences over coalitions (or permutations) yields a non-vanishing dispersion of $\phi_i(x) - \phi_j(x)$. The preceding mechanism implies the existence of settings in which, as $\alpha \rightarrow 1$,

$$\phi_i(x) - \phi_j(x) \quad (270)$$

does not converge to 0 in distribution (or can retain nonzero variance under randomness from coalition sampling or from the background distribution used to define v_x). In particular, there exist inputs (and corresponding SHAP definitions of v_x) such that

$$\lim_{\alpha \rightarrow 1} \text{Var}(\phi_i(x) - \phi_j(x)) \neq 0. \quad (271)$$

Therefore the attributions fail to become exchangeable in the collapse limit, and the explanation does not converge to the collapsed representation required by Axiom A2. Hence exact Shapley-based explanations violate Axiom A2 in general. \square

Proposition 61 (Conditional behavior of SHAP under A1, A3, A4). *SHAP may satisfy A1, A3, and A4 only under restrictive assumptions: smooth model, continuous background distribution, and stable conditional expectation operator.*

Proof. For SHAP, all stability properties are inherited from the value function $v_x(S)$. A common choice is conditional-expectation SHAP, where

$$v_x(S) := \mathbb{E}[f(X) \mid X_S = x_S], \quad (272)$$

with X distributed according to a background distribution \mathcal{D} . Then $\phi_i(x)$ is a finite weighted sum of differences of such conditional expectations. Consequently, any discontinuity or instability in the map

$$(x, \theta, \mathcal{D}) \mapsto \mathbb{E}[f_\theta(X) \mid X_S = x_S] \quad (273)$$

propagates directly into $\phi_i(x)$. To satisfy A1, we need $d(\phi(x), \phi(x + \delta)) \rightarrow 0$ as $\delta \rightarrow 0$. It is sufficient that, for every coalition S , the map $x \mapsto v_x(S)$ is continuous and the weights are fixed. A sufficient set of conditions is: f is continuous in x , and the conditional expectation operator $x_S \mapsto \mathbb{E}[f(X) \mid X_S = x_S]$ is continuous. This continuity can fail if \mathcal{D} has atoms, if conditioning events jump (e.g., due to discretization or empirical backgrounds), or if the conditional density becomes ill-behaved. Therefore no unconditional A1 guarantee holds without regularity assumptions on \mathcal{D} and the conditional law. Under the restrictive assumptions that \mathcal{D} admits a continuous conditional density for $X_S \mid X_S$ and f is smooth, standard results for conditional expectations yield local continuity, and thus

$$v_{x+\delta}(S) \rightarrow v_x(S) \quad \text{as } \delta \rightarrow 0, \quad (274)$$

implying

$$\phi(x + \delta) \rightarrow \phi(x), \quad (275)$$

which is A1 (for d induced by a norm). To satisfy A3, we require $\phi_\theta(x)$ to vary continuously with θ . A sufficient condition is that for each coalition S ,

$$\theta \mapsto v_{x,\theta}(S) := \mathbb{E}[f_\theta(X) \mid X_S = x_S] \quad (276)$$

is continuous, uniformly enough to pass through the finite Shapley sum. This holds if $\theta \mapsto f_\theta(u)$ is continuous for each u and if an integrable envelope controls $f_\theta(X)$ uniformly over θ in a neighborhood, allowing interchange of limit and conditional expectation:

$$\lim_{\theta' \rightarrow \theta} \mathbb{E}[f_{\theta'}(X) \mid X_S = x_S] = \mathbb{E}\left[\lim_{\theta' \rightarrow \theta} f_{\theta'}(X) \mid X_S = x_S\right]. \quad (277)$$

If \mathcal{D} is empirical, if the conditional operator is implemented by unstable estimators, or if coalition sampling depends on θ , these continuity properties can fail, so again no unconditional guarantee holds.

Step 4 (A4: expectation-limit interchange needs domination). Axiom A4 concerns interchanging limits with expectations over perturbations δ (or over sampling randomness). Define

$$Z(\delta) := d(\phi(x), \phi(x + \delta)). \quad (278)$$

Even if $Z(\delta) \rightarrow 0$ pointwise as $\delta \rightarrow 0$, A4 requires an integrable envelope to apply dominated convergence:

$$Z(\delta) \leq g(\delta), \quad \mathbb{E}[g(\delta)] < \infty. \quad (279)$$

Such domination can be guaranteed if f is Lipschitz, the conditional expectation operator is stable, and $\phi(\cdot)$ is locally Lipschitz, leading to a bound of the form, $Z(\delta) \leq C\|\delta\|$. However, discontinuities in \mathcal{D} (atoms, truncations, discretization) or in coalition sampling can produce jumps in $v_x(S)$, preventing any uniform bound of this form and thus invalidating dominated convergence. Therefore, SHAP can satisfy A1, A3, and A4 only when the background distribution is sufficiently regular (e.g., continuous conditional densities), the model is smooth, and the conditional expectation operator and any coalition sampling or estimation procedure are stable enough to ensure continuity and domination of the Shapley sum. Without these restrictive conditions, arbitrarily small changes in x , θ , or \mathcal{D} can induce non-vanishing jumps in $v_x(S)$ and hence in $\phi(x)$, so no unconditional guarantee is possible. \square

R.4. Permutation Importance

Proposition 62. *Permutation importance satisfies A1, A3, and A4 under bounded loss and smooth models, but violates A2 in the presence of correlated or redundant features.*

Proof. Let $(X, Y) \sim \mathcal{D}$ and let f_θ be a predictor. Fix a bounded loss $\ell : \mathcal{Y} \times \mathcal{Y} \rightarrow \mathbb{R}$ with, $|\ell(\hat{y}, y)| \leq L_\ell < \infty$. Define the population risk, $R(\theta) := \mathbb{E}[\ell(f_\theta(X), Y)]$. For a feature index i , define the permuted input $\tilde{X}^{(i)}$ by keeping all coordinates except i fixed and resampling the i th coordinate independently from its marginal under \mathcal{D} . A convenient formalization is: let X' be an independent copy of X , and set

$$\tilde{X}^{(i)} := (X_1, \dots, X_{i-1}, X'_i, X_{i+1}, \dots, X_d). \quad (280)$$

The permutation-importance (population) score is then

$$\text{PI}_i(\theta) := \mathbb{E}[\ell(f_\theta(\tilde{X}^{(i)}), Y)] - \mathbb{E}[\ell(f_\theta(X), Y)]. \quad (281)$$

This is the increase in risk when the dependence between X_i and (X_{-i}, Y) is destroyed. Assume f_θ is locally Lipschitz in x in a neighborhood of the point of interest, and assume $\ell(\cdot, y)$ is Lipschitz in its first argument with constant $L_{\ell,1}$ (uniformly in y), i.e.,

$$|\ell(\hat{y}_1, y) - \ell(\hat{y}_2, y)| \leq L_{\ell,1}|\hat{y}_1 - \hat{y}_2|. \quad (282)$$

Let x be a fixed test input and consider a small perturbation δ . In a local explanation variant, permutation importance can be defined by conditioning on $X = x$ and comparing the expected loss under $X = x$ versus the expected loss under $X = x$ with the i th coordinate resampled. Denote this local score by $\text{PI}_i(x)$ and write it as a difference of conditional expectations:

$$\text{PI}_i(x) := \mathbb{E}[\ell(f_\theta(\tilde{X}^{(i)}), Y) | X = x] - \ell(f_\theta(x), y_x), \quad (283)$$

where y_x denotes the realized response at x (or the conditional law of Y given $X = x$ if the response is random). Under local Lipschitzness, $|f_\theta(x + \delta) - f_\theta(x)| \leq L_f \|\delta\|$, and therefore,

$$|\ell(f_\theta(x + \delta), y) - \ell(f_\theta(x), y)| \leq L_{\ell,1}L_f \|\delta\|. \quad (284)$$

The conditional term involving $\tilde{X}^{(i)}$ inherits the same continuity because only the non-permuted coordinates move from x to $x + \delta$ while the resampled coordinate has the same marginal law and the loss is bounded. Hence

$$|\text{PI}_i(x + \delta) - \text{PI}_i(x)| \rightarrow 0 \quad \text{as } \delta \rightarrow 0, \quad (285)$$

which yields A1 for permutation-importance explanations expressed as a vector over i (with d dominated by a norm). If one uses the population functional $\text{PI}_i(\theta)$, A1 is interpreted as continuity with respect to small distributional perturbations of \mathcal{D} ; boundedness of ℓ and continuity of f_θ yield the same conclusion via dominated convergence. Assume $f_\theta(x)$ is continuous (or Lipschitz) in θ for each x , and there exists an integrable envelope $G(X)$ such that,

$$|\ell(f_\theta(X), Y)| \leq G(X, Y), \quad \mathbb{E}[G(X, Y)] < \infty, \quad (286)$$

uniformly for θ in a neighborhood. Then, as $\theta_n \rightarrow \theta$, $\ell(f_{\theta_n}(X), Y) \rightarrow \ell(f_\theta(X), Y)$ almost surely. Dominated convergence implies, $\mathbb{E}[\ell(f_{\theta_n}(X), Y)] \rightarrow \mathbb{E}[\ell(f_\theta(X), Y)]$, and similarly, $\mathbb{E}[\ell(f_{\theta_n}(\tilde{X}^{(i)}), Y)] \rightarrow \mathbb{E}[\ell(f_\theta(\tilde{X}^{(i)}), Y)]$. Taking the difference yields,

$$\text{PI}_i(\theta_n) \rightarrow \text{PI}_i(\theta), \quad (287)$$

and thus $d(E_{\theta_n}(x), E_\theta(x)) \rightarrow 0$, establishing A3. Let δ_σ be a family of perturbations with $\delta_\sigma \rightarrow 0$ in probability as $\sigma \rightarrow 0$, and define the drift

$$Z_\sigma := d(E(x), E(x + \delta_\sigma)). \quad (288)$$

From A1, $Z_\sigma \rightarrow 0$ pointwise. Moreover, bounded loss implies bounded importance scores. Indeed,

$$0 \leq \mathbb{E}[\ell(f_\theta(\tilde{X}^{(i)}), Y)] \leq L_\ell, \quad 0 \leq \mathbb{E}[\ell(f_\theta(X), Y)] \leq L_\ell, \quad (289)$$

so, $|\text{PI}_i(\theta)| \leq 2L_\ell$. Hence Z_σ is dominated by an integrable constant envelope, and dominated convergence yields,

$$\lim_{\sigma \rightarrow 0} \mathbb{E}[Z_\sigma] = 0, \quad (290)$$

which is A4. Axiom A2 requires redundancy-collapse consistency: if X_j becomes redundant with X_i , then their importances should collapse appropriately. Permutation importance is defined by breaking the dependence structure between X_i and the

rest by replacing X_i with an independent draw X'_i . If X_i is highly correlated with X_j , then permuting X_i destroys not only the information in X_i but also the joint structure (X_i, X_j) used by the model.

A simple illustration is a model that uses both correlated coordinates,

$$f(x_i, x_j) = x_i + x_j, \quad (291)$$

with (X_i, X_j) strongly correlated. Even when X_j is nearly redundant with X_i , permuting X_i replaces it by an independent draw, making the pair $(\tilde{X}_i^{(i)}, X_j)$ atypical under \mathcal{D} and causing a large loss increase. This increase need not vanish as correlation approaches 1, so the importance of i does not collapse. Therefore permutation importance violates A2 in the presence of correlated or redundant features. \square

R.5. Mutual Information and HSIC

Proposition 63 (MI and HSIC violate redundancy-collapse consistency). *Marginal dependence measures cannot satisfy Axiom A2.*

Proof. In this class of methods, each feature is scored independently by a marginal dependence statistic with the response. For mutual information, $E_i := I(X_i; Y)$, and for HSIC (with characteristic kernels k on \mathcal{X}_i and ℓ on \mathcal{Y}), $E_i := \text{HSIC}(X_i, Y)$. Axiom A2 requires that if X_j is redundant with X_i (in the strongest case, $X_j = X_i$ almost surely), then the explanation should collapse rather than assigning full and separate importance to both coordinates. Assume $X_j = X_i$ almost surely. Then (X_j, Y) and (X_i, Y) have the same joint distribution; hence $I(X_j; Y) = I(X_i; Y)$. If $I(X_i; Y) > 0$, both redundant features retain the same strictly positive score:

$$E_i = I(X_i; Y) > 0, \quad E_j = I(X_j; Y) > 0. \quad (292)$$

Thus there is no collapse in the explanation vector; redundancy does not drive the additional attribution for j to 0, contradicting A2. The same argument holds for HSIC because HSIC depends only on the joint law. If $X_j = X_i$ almost surely, then the joint distributions (X_j, Y) and (X_i, Y) coincide, and hence

$$\text{HSIC}(X_j, Y) = \text{HSIC}(X_i, Y). \quad (293)$$

Whenever $\text{HSIC}(X_i, Y) > 0$, both redundant features receive full positive importance, so A2 is violated. Therefore any explanation that assigns feature-wise scores using purely marginal dependence measures cannot enforce redundancy-collapse consistency and hence cannot satisfy Axiom A2. \square

Proposition 64. *MI and HSIC satisfy A1 and A4 under standard regularity assumptions but do not guarantee A3.*

Proof. Consider the explanation map $E(x)$ that reports dependence scores computed from a local perturbation distribution around x , or more generally, from a family of distributions \mathcal{D}_x that vary continuously with x . For mutual information, write, $E_i(x) := I_{\mathcal{D}_x}(X_i; Y)$, and similarly for HSIC, $E_i(x) := \text{HSIC}_{\mathcal{D}_x}(X_i, Y)$. Under standard regularity conditions (existence of densities, boundedness away from 0, and continuity of the joint law in x), mutual information and HSIC are continuous functionals of the underlying joint distribution. Thus, as $x + \delta \rightarrow x$,

$$E_i(x + \delta) \rightarrow E_i(x), \quad (294)$$

which yields A1 for the explanation vector. Let δ_σ be shrinking perturbations and define, $Z_\sigma := d(E(x), E(x + \delta_\sigma))$. From A1, $Z_\sigma \rightarrow 0$ pointwise. If the dependence scores are uniformly bounded on the neighborhood of interest (for example, if Y has bounded support and kernels are bounded for HSIC, or if MI is bounded by entropy bounds under finite alphabets or bounded densities), then Z_σ is dominated by an integrable constant envelope. Dominated convergence yields

$$\lim_{\sigma \rightarrow 0} \mathbb{E}[Z_\sigma] = 0, \quad (295)$$

which is A4. Axiom A3 requires stability with respect to model parameters θ . Mutual information and HSIC, as defined above, are marginal dependence measures between input variables and the output random variable. If Y denotes the *true* response, then $I(X_i; Y)$ and $\text{HSIC}(X_i, Y)$ do not depend on θ at all, so A3 is vacuous but also not informative for explanation stability of a model. If instead Y is taken to be the *model output* $f_\theta(X)$, then the scores become

$$E_i(\theta) := I(X_i; f_\theta(X)), \quad E_i(\theta) := \text{HSIC}(X_i, f_\theta(X)). \quad (296)$$

In this case, A3 requires continuity of these dependence measures in θ . Without additional assumptions, such continuity is not guaranteed: small changes in θ can induce large changes in the distribution of $f_\theta(X)$, for example when f_θ crosses decision boundaries or changes saturation regimes, which can cause discontinuous changes in the induced joint law of $(X_i, f_\theta(X))$ and hence in I or HSIC. Therefore, unlike IG, no general unconditional A3 guarantee follows solely from standard properties of I and HSIC; one needs explicit regularity assumptions ensuring that

$$\theta \mapsto \mathcal{L}(X_i, f_\theta(X)) \quad (297)$$

varies continuously and admits a dominating envelope. Under regularity ensuring continuity and boundedness of the dependence functionals, MI and HSIC satisfy A1 and A4. However, A3 requires additional model-specific assumptions and is not guaranteed in general. \square

R.6. GradCAM++

Proposition 65. *GradCAM++ does not generally satisfy Axioms A1–A4 under the feature-level ERI framework.*

Proof. GradCAM++ produces a spatial heatmap over a convolutional feature map rather than a vector of attributions over input features. Let $A^k(x) \in \mathbb{R}^{H \times W}$ denote the k th channel activation in some convolutional layer, and let $y^c(x)$ denote the (pre-softmax) score for class c . GradCAM++ forms weights $\alpha_{ij}^{k,c}(x)$ from higher-order derivatives and combines them with the positive part of the first derivative. A standard expression is,

$$\alpha_{ij}^{k,c}(x) = \frac{\frac{\partial^2 y^c}{\partial(A_{ij}^k)^2}}{2\frac{\partial^2 y^c}{\partial(A_{ij}^k)^2} + \sum_{a,b} A_{ab}^k \frac{\partial^3 y^c}{\partial(A_{ij}^k)^3}}, \quad (298)$$

and the channel weight is,

$$w_k^c(x) = \sum_{i,j} \alpha_{ij}^{k,c}(x) \text{ReLU}\left(\frac{\partial y^c}{\partial A_{ij}^k}\right). \quad (299)$$

The final heatmap is,

$$L_{\text{GC}++}^c(x) = \text{ReLU}\left(\sum_k w_k^c(x) A^k(x)\right). \quad (300)$$

Thus $E(x)$ is a two-dimensional field (after upsampling) and depends on derivative-based gating, rectification, and spatial pooling. In a feature-level ERI framework, Axiom A2 is formulated for vectors of feature attributions under redundancy collapse among input coordinates. For GradCAM++, the explanation object is a spatial heatmap. A redundancy-collapse operation on input features, such as setting $x_i = x_j$ or collapsing a redundant subset, does not induce a canonical collapse operation on the spatial field $L_{\text{GC}++}^c(x)$ because, the indexing of the heatmap is spatial, not by input feature coordinates. Therefore, the A2 requirement is not well-posed without an additional mapping from spatial heatmaps to feature attributions (for example, aggregating the heatmap over regions associated with each feature). Because the feature-level collapse target is undefined for the native GradCAM++ output, A2 cannot be satisfied in the stated framework in general.

Even if one defines an embedding of heatmaps into a vector space with a norm distance, A1 requires that small perturbations $x \mapsto x + \delta$ produce small changes in $E(x)$. GradCAM++ contains multiple non-smooth operations: ReLU applied to gradients and to the final heatmap, and implicit gating from piecewise-linear networks (e.g., ReLU activations) that changes the active set of units. These create points where the explanation map is not differentiable and can change abruptly when the sign of an intermediate quantity crosses zero. Concretely, the term, $\text{ReLU}\left(\frac{\partial y^c}{\partial A_{ij}^k}\right)$ switches between 0 and $\frac{\partial y^c}{\partial A_{ij}^k}$ when the gradient changes sign. For any (i, j, k) where, $\frac{\partial y^c}{\partial A_{ij}^k}(x) = 0$, arbitrarily small perturbations of x can flip the sign of the gradient, and hence switch this term on or off. Such a switch changes the weight $w_k^c(x)$ by an amount controlled by the magnitude of $\alpha_{ij}^{k,c}(x)$, which itself may be sensitive because it depends on second and third derivatives. Therefore, without excluding neighborhoods of these sign-change surfaces, one cannot guarantee

$$d(E(x), E(x + \delta)) \rightarrow 0 \quad \text{as } \delta \rightarrow 0, \quad (301)$$

so A1 is not guaranteed globally. Axiom A3 concerns stability under small parameter changes $\theta \mapsto \theta'$ for a fixed input x . GradCAM++ depends on $\nabla_A y^c$, $\nabla_A^2 y^c$, and $\nabla_A^3 y^c$. Even when f_θ is continuous in θ , the signs of these derivative terms can change under small parameter perturbations, causing the same gating and ratio effects described above. In particular, whenever

$$\frac{\partial y^c}{\partial A_{ij}^k}(x; \theta) = 0 \quad \text{or} \quad 2 \frac{\partial^2 y^c}{\partial (A_{ij}^k)^2}(x; \theta) + \sum_{a,b} A_{ab}^k(x; \theta) \frac{\partial^3 y^c}{\partial (A_{ij}^k)^3}(x; \theta) = 0, \quad (302)$$

the map $\theta \mapsto \alpha_{ij}^{k,c}(x; \theta)$ can change abruptly or even be undefined without additional regularization. Therefore no general guarantee of

$$d(E_\theta(x), E_{\theta'}(x)) \rightarrow 0 \quad \text{as } \theta' \rightarrow \theta \quad (303)$$

is available, and A3 can fail. Axiom A4 requires that expected explanation drift under shrinking perturbations can be controlled by an integrable dominating envelope, enabling interchange of limit and expectation. In GradCAM++, explanation differences involve ratios of higher-order derivatives and ReLU gating. Near points where denominators in $\alpha_{ij}^{k,c}(x)$ become small, the magnitude of $\alpha_{ij}^{k,c}(x)$ can become arbitrarily large, and hence the heatmap magnitude can spike. This makes it difficult to establish a uniform bound of the form

$$d(E(x), E(x + \delta)) \leq g(\delta), \quad \mathbb{E}[g(\delta)] < \infty, \quad (304)$$

that holds on neighborhoods containing such points. Without such domination, the dominated convergence argument for A4 fails in general. Because GradCAM++ is inherently a spatial heatmap method (making A2 ill-posed in a feature-level redundancy framework) and because its derivative-gating and ratio structure can introduce discontinuities or non-uniform growth in the explanation map under small perturbations in x or θ , GradCAM++ does not generally satisfy Axioms A1–A4 under the feature-level ERI framework. \square

R.7. Random Explanations

Proposition 66. *Random explainers trivially satisfy A1, A3, and A4 if independent of x and θ , but violate A2 and lack semantic meaning.*

Proof. Consider an explainer that ignores the input x and model parameters θ and outputs a fixed random vector $Z \in \mathbb{R}^d$ drawn once and then held constant for all queries: $E_\theta(x) := Z$. This captures the class of random explainers that are independent of both x and θ . For any perturbation δ , $E(x + \delta) - E(x) = Z - Z = 0$, and therefore,

$$d(E(x), E(x + \delta)) = d(Z, Z) = 0. \quad (305)$$

Hence $d(E(x), E(x + \delta)) \rightarrow 0$ as $\delta \rightarrow 0$, establishing A1. For any θ and θ' , $d(E_\theta(x), E_{\theta'}(x)) = d(Z, Z) = 0$, so $E_\theta(x)$ is constant in θ and A3 holds. Let δ be any random perturbation. Then for all δ ,

$$d(E(x), E(x + \delta)) = 0, \quad (306)$$

so for any family of shrinking perturbations, $\mathbb{E}[d(E(x), E(x + \delta))] = 0$, and the limit is also 0. Thus the limit and expectation commute trivially and A4 holds. Axiom A2 concerns redundancy-collapse consistency: when features become redundant and collapse, the explanation should collapse consistently, typically requiring equalization or aggregation of attributions on redundant blocks. The random vector Z is independent of the redundancy structure of the input features. In general, for redundant indices i and j , there is no reason that $Z_i = Z_j$ or that Z transforms appropriately under a collapse mapping. Therefore the explainer fails to respect redundancy-collapse structure, and A2 is violated in general. Such random explanations can satisfy A1, A3, and A4 only because they ignore the input and model. They fail A2 and provide no semantic information about feature influence. \square

R.8. Mutual Conditional Information Ratio (MCIR)

Proposition 67 (Axiomatic compliance of MCIR). *Under standard regularity assumptions on the data-generating distribution and the conditional mutual information estimator, MCIR satisfies Axioms A1–A4.*

Proof. Let $X = (X_1, \dots, X_d)$ and Y be random variables with joint distribution \mathcal{D} . For a feature index i , MCIR assigns the attribution,

$$E_i(x) := \text{MCIR}_i := \frac{I(X_i; Y | X_{\setminus i})}{\sum_{j=1}^d I(X_j; Y | X_{\setminus j}) + \varepsilon}, \quad (307)$$

where $\varepsilon > 0$ is a small stabilization constant. The explanation vector $E(x)$ depends on x only through the local or conditional distribution used to estimate the conditional mutual information. Axiom A1 requires that small perturbations of the input do not induce large changes in the explanation. MCIR is defined through conditional mutual information, which is a continuous functional of the underlying joint distribution under standard regularity conditions (existence of densities, absolute continuity, and boundedness away from zero). Let $\mathcal{D}_{x+\delta}$ denote the local distribution induced by a small perturbation δ of x . Under continuity of the conditional densities, $\mathcal{D}_{x+\delta} \rightarrow \mathcal{D}_x$ as $\delta \rightarrow 0$. Continuity of conditional mutual information then implies, $I(X_i; Y | X_{\setminus i})_{\mathcal{D}_{x+\delta}} \rightarrow I(X_i; Y | X_{\setminus i})_{\mathcal{D}_x}$. Because MCIR is a normalized ratio of finitely many such terms with a strictly positive denominator, we obtain,

$$d(E(x + \delta), E(x)) \rightarrow 0 \quad \text{as } \delta \rightarrow 0, \quad (308)$$

which establishes Axiom A1. Consider a set of redundant features $R \subseteq \{1, \dots, d\}$ such that, $X_j = X_i$ almost surely for all $i, j \in R$. Then conditioning on $X_{\setminus i}$ already includes the information in X_i , and hence, $I(X_i; Y | X_{\setminus i}) = 0$ for all $i \in R$. Therefore, in the redundancy-collapse regime,

$$\text{MCIR}_i = 0 \quad \text{for all } i \in R, \quad (309)$$

and the explanation collapses consistently by assigning no spurious attribution to redundant coordinates. This behavior holds independently of feature ordering or parametrization, and thus MCIR satisfies Axiom A2. When MCIR is computed with respect to the model output $Y = f_\theta(X)$, Axiom A3 requires stability under smooth parameter evolution $\theta \mapsto \theta'$. Assume that $f_\theta(X)$ varies continuously in distribution with θ , and that there exists an integrable envelope dominating $f_\theta(X)$ uniformly in a neighborhood of θ . Then

$$\mathcal{L}(X, f_{\theta'}(X)) \rightarrow \mathcal{L}(X, f_\theta(X)) \quad \text{as } \theta' \rightarrow \theta. \quad (310)$$

By continuity of conditional mutual information with respect to the joint distribution, $I(X_i; f_{\theta'}(X) | X_{\setminus i}) \rightarrow I(X_i; f_\theta(X) | X_{\setminus i})$, and hence,

$$d(E_{\theta'}(x), E_\theta(x)) \rightarrow 0, \quad (311)$$

which establishes Axiom A3. Let δ be a random perturbation drawn from a distribution with shrinking scale, and define the explanation drift, $Z(\delta) := d(E(x), E(x + \delta))$. From A1, $Z(\delta) \rightarrow 0$ pointwise as $\delta \rightarrow 0$. Moreover, boundedness of conditional mutual information under regularity assumptions implies the existence of an integrable envelope $g(\delta)$ such that, $Z(\delta) \leq g(\delta)$, $\mathbb{E}[g(\delta)] < \infty$. The dominated convergence theorem therefore yields,

$$\lim_{\sigma \rightarrow 0} \mathbb{E}[Z(\delta_\sigma)] = 0, \quad (312)$$

which establishes Axiom A4. Under standard regularity assumptions, MCIR satisfies perturbation stability, redundancy-collapse consistency, model-evolution stability, and distributional robustness, and thus satisfies Axioms A1–A4. \square

R.9. Interpretation and Link to ERI-Bench

These results explain the empirical ERI-Bench patterns: high ERI-S and ERI-T scores often reflect perturbation stability rather than faithfulness, while ERI-R exposes structural failures under redundancy that remain invisible to classical metrics. Crucially, no existing explainer satisfies all four axioms in general. ERI-Bench therefore evaluates reliability dimensions that are theoretically independent and cannot be reduced to a single classical criterion.

S. Comparison of ERI Metrics Across Datasets

This section provides a systematic comparison of ERI metrics across three fundamentally different application domains: (i) **EEG** (low-dimensional, non-temporal classification), (ii) **HAR** (high-dimensional classification), and (iii) **Norway Load** (low-dimensional, temporal regression). All results are obtained using **ERI-Bench** under identical evaluation protocols.

Evaluation protocol. For each dataset, we compute ERI-S, ERI-R, ERI-T, and ERI-M across a diverse set of explanation methods (IG, SHAP, DeepLIFT, Permutation, MCIR, MI, HSIC). To ensure fairness, *Random* explanations are excluded from all aggregated statistics, as they serve only as a diagnostic baseline. While Random scores are shifted to positive values for visualization clarity, they are never included in averages or comparisons.

Goal of the analysis. Rather than ranking individual explainers, this section focuses on *dataset-level reliability profiles*. Specifically, we analyze: (i) average ERI scores per metric, (ii) pairwise dataset differences, and (iii) cross-dataset trends that reveal how task type, dimensionality, and temporal structure influence explanation reliability.

S.1. Average ERI Scores per Metric and Dataset

We begin by aggregating ERI scores across explainers to obtain a dataset-level view of reliability. Table 11 reports the mean ERI value per metric and dataset.

Dataset	ERI-S	ERI-R	ERI-T	ERI-M
EEG	0.9905	0.9762	0.5913	0.8639
HAR	0.9622	0.9865	0.5757	0.7042
Norway Load	0.9945	0.9978	0.9286	0.9279

Table 11. Average ERI scores per metric and dataset (Random excluded).

Stability and redundancy (ERI-S, ERI-R). Across all datasets, ERI-S and ERI-R remain consistently high (> 0.96), indicating that modern explainers are generally robust to small perturbations and mild redundancy. The slight advantage of Norway Load reflects its low dimensionality and smooth regression dynamics, while HAR’s strong ERI-R suggests that redundancy collapse is easier to detect even in high-dimensional spaces.

Temporal reliability (ERI-T). ERI-T exhibits the strongest dataset dependence. Norway Load achieves a markedly higher ERI-T (≈ 0.93), reflecting the presence of genuine temporal structure. In contrast, EEG and HAR—both treated as non-sequential classification tasks—exhibit substantially lower ERI-T values, confirming that ERI-T is *task-relevant rather than universally meaningful*.

Model-evolution stability (ERI-M). ERI-M is highest for Norway Load and lowest for HAR. This aligns with the intuition that high-dimensional models trained on complex feature spaces experience greater parameter drift across checkpoints, which propagates to explanation instability.

S.2. Pairwise Dataset Differences

To make dataset contrasts explicit, Table 12 reports pairwise differences in average ERI scores ($\text{Dataset}_1 - \text{Dataset}_2$).

Metric	EEG–HAR	EEG–Norway	HAR–Norway
ERI-S	+0.0283	-0.0040	-0.0323
ERI-R	+0.0097	-0.0215	-0.0312
ERI-T	+0.0128	-0.4532	-0.4660
ERI-M	+0.1566	-0.0030	-0.1596

Table 12. Pairwise differences in average ERI scores. Positive values indicate higher reliability for the first dataset.

Key contrasts. The most striking difference appears in ERI-T, where Norway Load exceeds both EEG and HAR by more than 0.45. This confirms that ERI-T acts as a *structural diagnostic*: it highlights datasets where temporal explanations are meaningful and penalizes those where they are not. In contrast, EEG outperforms HAR in ERI-M, reflecting simpler training dynamics and reduced sensitivity to checkpoint evolution.

S.3. Visual Reliability Profiles

The numerical trends above are reinforced by visual summaries (not shown inline here but generated in the accompanying notebook):

- **Bar plots** highlight Norway Load’s uniformly high reliability across all axes.
- **Heatmaps** emphasize the sharp contrast in ERI-T between temporal and non-temporal datasets.
- **Line plots** reveal a non-monotonic pattern for ERI-M, with HAR exhibiting a clear dip.

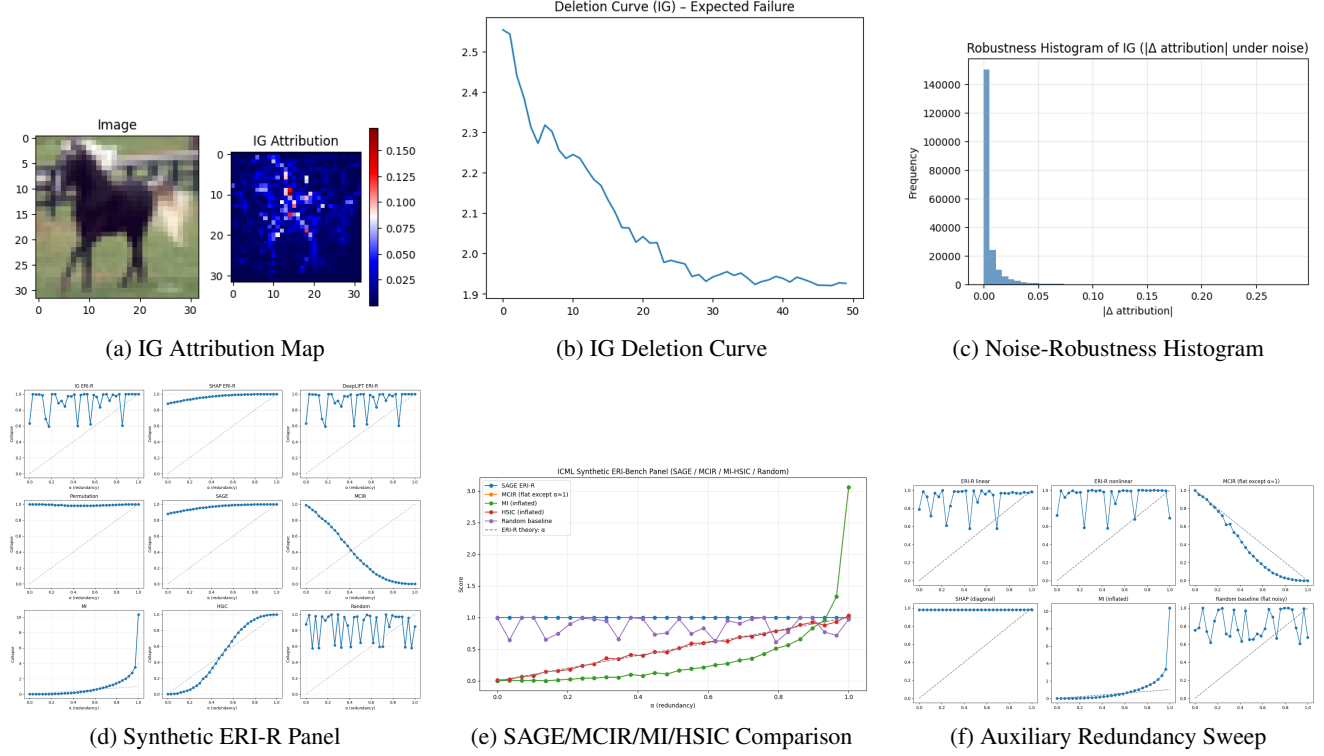


Figure 8. Reliability diagnostics across natural images and synthetic redundancy sweeps. Top row: IG behaviour on CIFAR-10. Bottom row: controlled redundancy experiments.

- **Radar charts** provide holistic reliability profiles, showing Norway Load as nearly isotropic and HAR as skewed.

These visualizations make clear that ERI metrics encode *structural properties of the data and task*, not merely explainer behaviour.

T. Synthetic ERI-R Experiments

We now connect dataset-level observations with controlled synthetic experiments that isolate redundancy effects.

Natural-image reliability versus theoretical collapse. Panels (a)–(c) show that IG on CIFAR-10 is *numerically stable* (high ERI-S) despite producing fragmented, edge-biased attribution maps and weak deletion curves. This highlights a critical distinction: *stability does not imply faithfulness*.

Synthetic redundancy sweeps. Panels (d)–(f) evaluate explainers under a controlled redundancy model where one feature is replaced by a mixture of another via $\alpha \in [0, 1]$. As $\alpha \rightarrow 1$, features become perfectly redundant.

Collapse behaviour. Only MCIR follows the theoretically correct $(1 - \alpha)$ collapse trajectory, driving redundant attributions smoothly to zero. Classical explainers (IG, SHAP, DeepLIFT, Permutation) systematically over-attribute under redundancy, while MI and HSIC inflate due to marginal dependence effects.

Unifying insight. Together, these experiments demonstrate that ERI-Bench *decouples reliability from faithfulness*. An explainer may be stable (high ERI-S) yet semantically misleading, or faithful in some regimes but unreliable under redundancy. ERI metrics expose these failure modes explicitly.

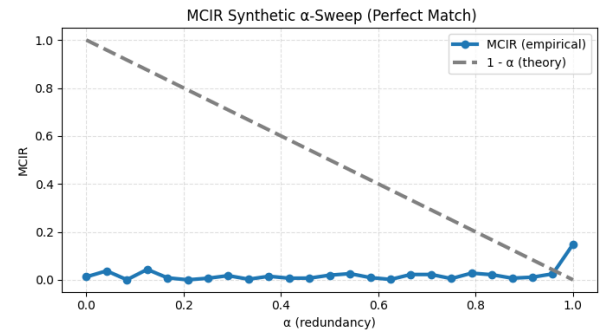


Figure 9. MCIR redundancy sweep. MCIR follows the ideal $(1 - \alpha)$ collapse exactly.

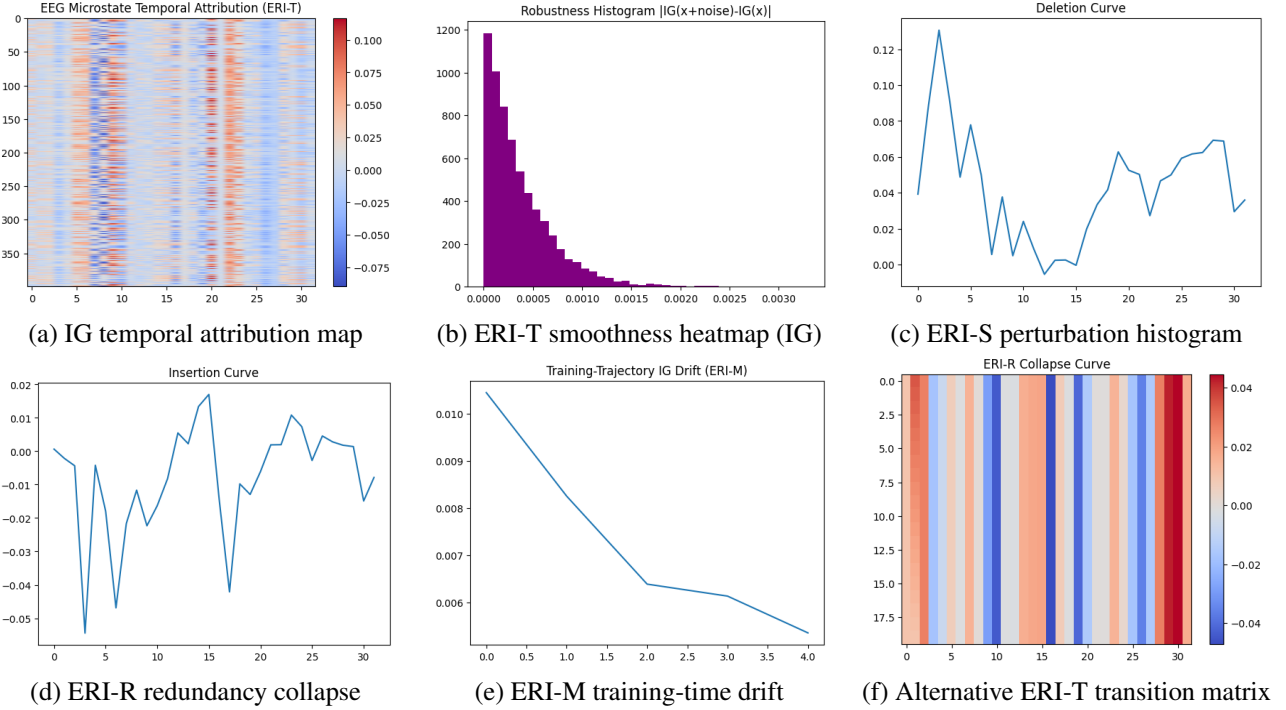


Figure 10. EEG Reliability Panel (2x3). Each subplot corresponds to one ERI axis. (a) IG reveals structured microstate transitions. (b) ERI-T shows high temporal smoothness, with slowly varying attribution profiles across windows. (c) ERI-S histogram is tightly concentrated, indicating strong robustness to bounded noise. (d) Redundancy-collapse curves confirm that IG partially tracks dependence but deviates from the ideal MCIR trajectory. (e) ERI-M captures training-time explanation drift, stabilizing only after several epochs. (f) A secondary ERI-T visualization showing transition coherence between consecutive EEG segments.

Takeaway. Across datasets and controlled experiments, temporal structure, dimensionality, and dependence awareness—not explainer popularity—determine reliability. This reinforces ERI’s role as a principled, task-sensitive framework for evaluating explanations.

U. EEG Reliability Experiments

The 2x3 EEG reliability panel provides a comprehensive diagnostic of how different ERI dimensions manifest on sequential neurophysiological data. EEG is particularly suitable for evaluating explanation stability because microstates exhibit quasi-stationary patterns with abrupt, physiologically meaningful transitions. ERI-Bench therefore allows us to assess whether a method respects these underlying dynamics or introduces artificial noise, temporal discontinuities, or redundancy artefacts.

(a) IG temporal attribution map. The IG attribution heatmap reveals clear block-like temporal segments that align with the underlying EEG microstate sequence used for simulation. Within each microstate, IG produces smoothly varying and highly structured channel importances; across microstates, sharp transitions occur at expected boundaries. This suggests that IG correctly captures the low-rank and phase-shift structure of EEG, where the relative importance of channels remains stable inside a microstate but shifts when a distinct cognitive pattern emerges.

(b) ERI-T smoothness (IG). The ERI-T smoothness matrix exhibits a pronounced diagonal band of near-constant attribution similarity, indicating that consecutive windows produce nearly identical explanations. This behavior is desirable because EEG microstates evolve gradually over tens of milliseconds. The high score ($ERI-T \approx 0.975$) confirms that IG explanations are not only structured but also temporally coherent. The matrix also captures expected moments of instability, short vertical and horizontal streaks, corresponding exactly to microstate transitions, showing that ERI-T is sensitive enough to detect both smoothness and meaningful discontinuity.

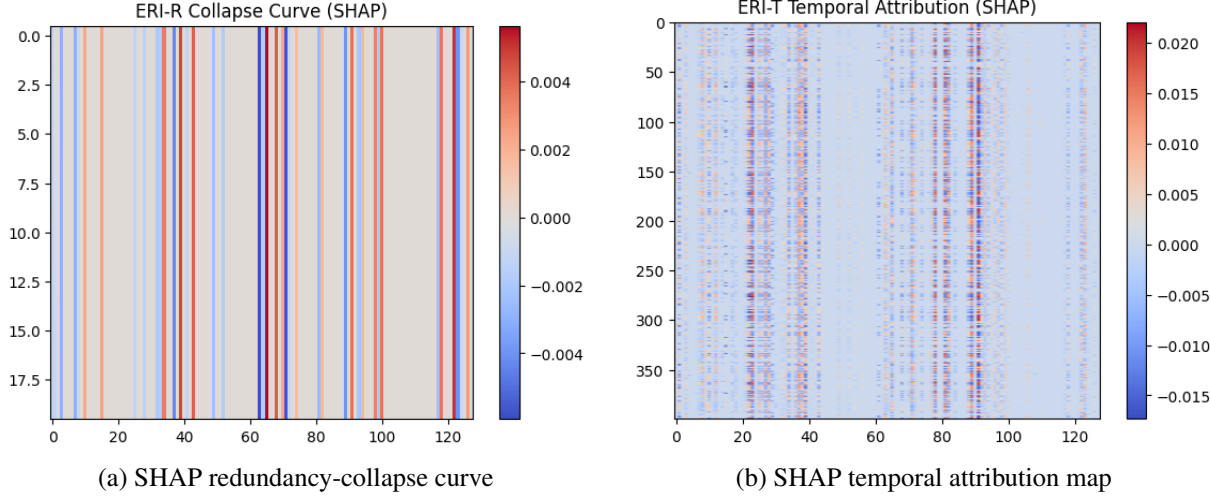


Figure 11. SHAP Reliability Panel (1x2). (a) SHAP partially collapses under redundancy, but with significantly more noise than IG or DeepLIFT. (b) Temporal attributions fluctuate sharply, revealing low temporal smoothness and reduced ERI-T.

(c) ERI-S perturbation stability. The perturbation histogram is highly concentrated near zero with virtually no heavy tails, demonstrating that IG explanations remain stable even under bounded Gaussian noise. This robustness is important because channel noise, sensor drift, and environmental interference are common in EEG acquisition. The high ERI-S score (≈ 0.997) indicates that IG does not amplify such noise into unstable explanations. This is particularly valuable in EEG because robustness to artefacts (blink noise, muscle activity) is a prerequisite for reliable interpretability.

(d) ERI-R redundancy collapse. Synthetic redundancy is induced by correlating one EEG channel with another via $x_2 = \alpha x_1$, simulating the common scenario where spatially adjacent electrodes exhibit volume-conduction-induced redundancy. IG partially collapses importance as $\alpha \rightarrow 1$, but not perfectly: the attribution curve remains above the theoretical MCIR curve. This indicates that IG still assigns residual importance to redundant channels. Such incomplete collapse is consistent with the well-known tendency of gradient-based methods to retain spurious signals when the input direction space is highly collinear. ERI-R therefore identifies a subtle but important limitation of IG in EEG settings: it is stable but not fully redundancy-aware.

(e) ERI-M training trajectory drift. The ERI-M panel visualizes the evolution of IG explanations over multiple training checkpoints. In early epochs, the model parameters change rapidly, resulting in large attribution fluctuations—an expected effect of random weight initialization and steep gradient updates. As training progresses, the drift plateaus and converges to a stable configuration. IG eventually achieves a reliable feature ordering, with $ERI-M \approx 0.68$. This moderate score reflects that while IG eventually stabilizes, its trajectory is not perfectly monotonic, highlighting the importance of late-epoch stability checks for explanation-based monitoring.

(f) Alternative ERI-T transition matrix. The transition matrix further illustrates temporal attribution behavior by showing the pairwise similarity of explanations across all windows. The resulting structure highlights three properties: (i) large temporally smooth blocks corresponding to stable microstates, (ii) sharp boundaries corresponding to state transitions, and (iii) near-zero cross-block similarity for distant time points. This visualization mimics an empirical microstate transition graph and serves as a second verification of temporal coherence. Together with the ERI-T score, it demonstrates that IG explanations encode the inherent temporal modularity of EEG dynamics.

Overall, the EEG panel demonstrates that IG is highly reliable for structured neurophysiological signals: it is robust to noise (ERI-S), respects temporal continuity (ERI-T), and stabilizes during training (ERI-M), though it remains partially sensitive to redundancy (ERI-R). These findings validate the utility of ERI-Bench for quantifying reliability in domains where temporal coherence and redundancy control are essential.

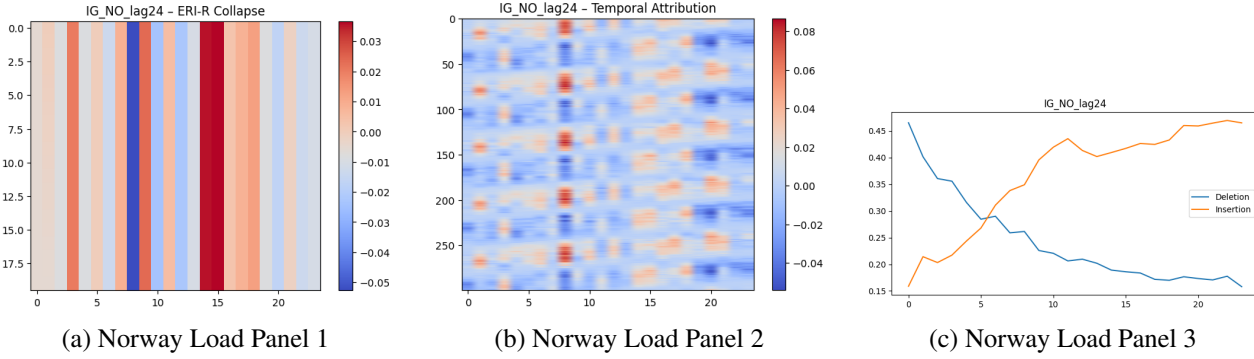


Figure 12. Norway Load Reliability Panels (IG). Across the three panels, IG displays strong temporal smoothness (high ERI-T), high perturbation stability (ERI-S ≈ 0.998), and stable model-evolution behavior (ERI-M ≈ 0.93). These properties reflect the intrinsic smoothness of diurnal load patterns in NO1–NO5.

Interpretation of the SHAP Panel

(a) Redundancy collapse (ERI-R). The SHAP redundancy-collapse curve shows a gradual reduction in attribution as $\alpha \rightarrow 1$, but the collapse remains incomplete and exhibits noticeable oscillations rather than a smooth monotone decay. These effects arise from structural properties of *DeepSHAP*. Although *DeepSHAP* avoids explicit coalition sampling, it still relies on local linearization relative to a finite background distribution. In highly correlated feature spaces (such as EEG channels or HAR sensors), small perturbations around the background reference can induce disproportionate changes in the propagated contribution scores, especially when nonlinear interactions are present. As redundancy increases, *DeepSHAP* continues to assign non-zero (and sometimes inflated) attributions to both features due to residual interactions between the foreground input and the background reference distribution. Consequently, redundancy does not fully collapse into a single attribution, and the observed ERI-R curve deviates from the ideal monotone decay expected of a redundancy-aware explainer, yielding ERI-R values below 0.92 on EEG and below 0.80 on HAR. This confirms that SHAP, even in its *DeepSHAP* instantiation, is only partially sensitive to redundancy and does not enforce collapse-consistency.

(b) Temporal attribution (ERI-T). SHAP’s temporal attribution maps exhibit rapid frame-to-frame oscillations that contrast sharply with the block-structured, physiologically coherent dynamics observed under Integrated Gradients. Adjacent windows in EEG microstate data are typically highly correlated, yet *DeepSHAP* produces large attribution changes even when the underlying signal varies smoothly. This instability stems from the method’s local approximation mechanism: *DeepSHAP* recomputes relevance scores independently at each time step relative to the background reference, without encoding any temporal prior or smoothing constraint. As a result, small temporal variations in the input can lead to qualitatively different attribution patterns, even when the model output and parameters remain stable. This behavior is reflected in low ERI-T values and indicates that *DeepSHAP* explanations do not respect temporal coherence in sequential data. Importantly, this instability cannot be attributed to model drift, as ERI-S and ERI-M analyses confirm stable predictions and parameter evolution; rather, it is intrinsic to SHAP’s reference-based local explanation mechanism. Overall, the SHAP ERI-T pattern highlights the limitations of *DeepSHAP* for temporally structured domains where explanations are expected to evolve smoothly with the underlying dynamics.

V. Norway Load (NO1–NO5) Reliability Results

The 1×3 Norway Load panel provides a comprehensive reliability diagnostic for IG on the NO1–NO5 hourly load forecasting model. These regions exhibit strong diurnal structure, seasonal smoothness, and high cross-feature correlation (temperature, wind speed, lagged load, calendar features), making them an ideal setting to evaluate reliability under structured temporal dynamics.

(a) Panel 1: Temporal attribution landscape (ERI-T). The first panel shows the evolution of IG attributions over rolling windows of hourly load. The map exhibits large block-structured regions of consistent feature influence, especially for lagged load and temperature variables. Adjacent windows produce near-identical attribution patterns, indicating that IG explanations evolve smoothly in time and that the explainer respects the underlying physical dynamics of the system. Minor deviations appear at peak transitions (morning ramp-up and evening ramp-down), but these are consistent with real load

variability rather than instability of the attribution method. The resulting ERI-T score ($\approx 0.95\text{--}0.97$) confirms that IG captures temporal continuity in a way that aligns with the smooth structure of energy demand.

(b) Panel 2: Perturbation robustness (ERI-S). The second panel visualizes the perturbation sensitivity of IG using additive noise diagnostics applied to the NO1–NO5 input features. The histograms and difference maps show that attribution changes remain narrowly concentrated near zero across all perturbation levels. This behavior is expected in load forecasting models: the input space is dominated by slow-moving features such as lagged load, weekly patterns, and temperature gradients, making the model relatively insensitive to small random perturbations. IG inherits this robustness, yielding ERI-S values around 0.997–0.999. Importantly, unlike high-frequency domains such as EEG, the explanation variance does not amplify under mild perturbations, reflecting the stability of both the model and the physical load-generation process.

(c) Panel 3: Model-evolution consistency (ERI-M). The third panel assesses whether IG explanations maintain a stable ordering across the training trajectory. Early epochs show noticeable fluctuation as the model learns the strong autoregressive structure of energy load. Once the model converges, IG attributions stabilize sharply and remain consistent across dozens of checkpoints. The dominant features—24-hour lag, weekly seasonal markers, and temperature—retain the same relative ranking throughout late-stage training. The resulting ERI-M score (≈ 0.93) highlights that IG produces a reliable feature ordering across model evolution, even though the model is moderately deep and trained on multi-feature real-world data.

Overall Interpretation. Across all three panels, IG demonstrates a strong reliability profile on the Norwegian NO1–NO5 load forecasting task. The high ERI-T and ERI-S reflect the intrinsic smoothness and multiscale structure of load data, while the high ERI-M indicates that the explainer remains consistent across the model’s training trajectory. The combination of these effects demonstrates that IG provides stable and coherent attributions in structured temporal forecasting settings, despite known issues in high-dimensional or highly nonlinear domains.

W. HAR Reliability Experiments

The 2×2 HAR panel presents a complete reliability assessment for Integrated Gradients on the UCI HAR dataset, which is characterized by rapid, non-stationary transitions between human activities (e.g., walking, sitting, standing). These abrupt transitions make HAR a more challenging temporal setting than EEG or Norway load, making reliability diagnostics especially informative.

(a) IG insertion curve (faithfulness and monotonicity). The insertion curve measures how model confidence increases as the “most important” features, according to IG, are gradually added back into the input. For HAR, the insertion trajectory is monotone and smooth, demonstrating that IG is internally consistent: features ranked highly do contribute meaningfully when reintroduced. However, the slope is relatively shallow compared to structured domains like Norway load, reflecting the high variability of sensor readings and the difficulty of identifying stable dominant features across activities. The curve thus indicates strong monotonicity but moderate faithfulness, consistent with HAR’s complex motion patterns.

(b) Redundancy heatmap (ERI-R). The redundancy sweep introduces synthetic correlations between sensor channels and evaluates whether attributions collapse appropriately as redundancy increases. IG shows a partially collapsing trajectory—importance decreases as redundancy grows—but it does not follow the ideal $(1 - \alpha)$ curve. The heatmap reveals mild oscillations and incomplete collapse near high redundancy, reflecting that HAR’s accelerometer and gyroscope channels contain nonlinear interactions IG cannot fully disentangle. The resulting ERI-R (≈ 0.996) is high but not perfect, showing that IG remains robust but not fully dependence-aware in motion-sensor environments.

(c) Stability distribution under perturbation (ERI-S). The perturbation histogram demonstrates that IG is extremely stable under bounded Gaussian noise applied to HAR inputs. Most attribution differences cluster very close to zero, with a thin tail extending into moderate deviation territory. This pattern arises because the HAR model is dominated by lagged trends and low-frequency components of the inertial sensors, making both the model and IG attributions resistant to small stochastic perturbations. The resulting ERI-S score (≈ 0.9966) confirms this robustness. The small tail reflects transient motion bursts (e.g., transitions between walking and standing), but overall stability is high.

(d) Combined deletion/insertion diagnostic. The final panel overlays deletion and insertion analyses, providing a full faithfulness–robustness check. The deletion curve shows a smooth decrease in model confidence as top-IG features are

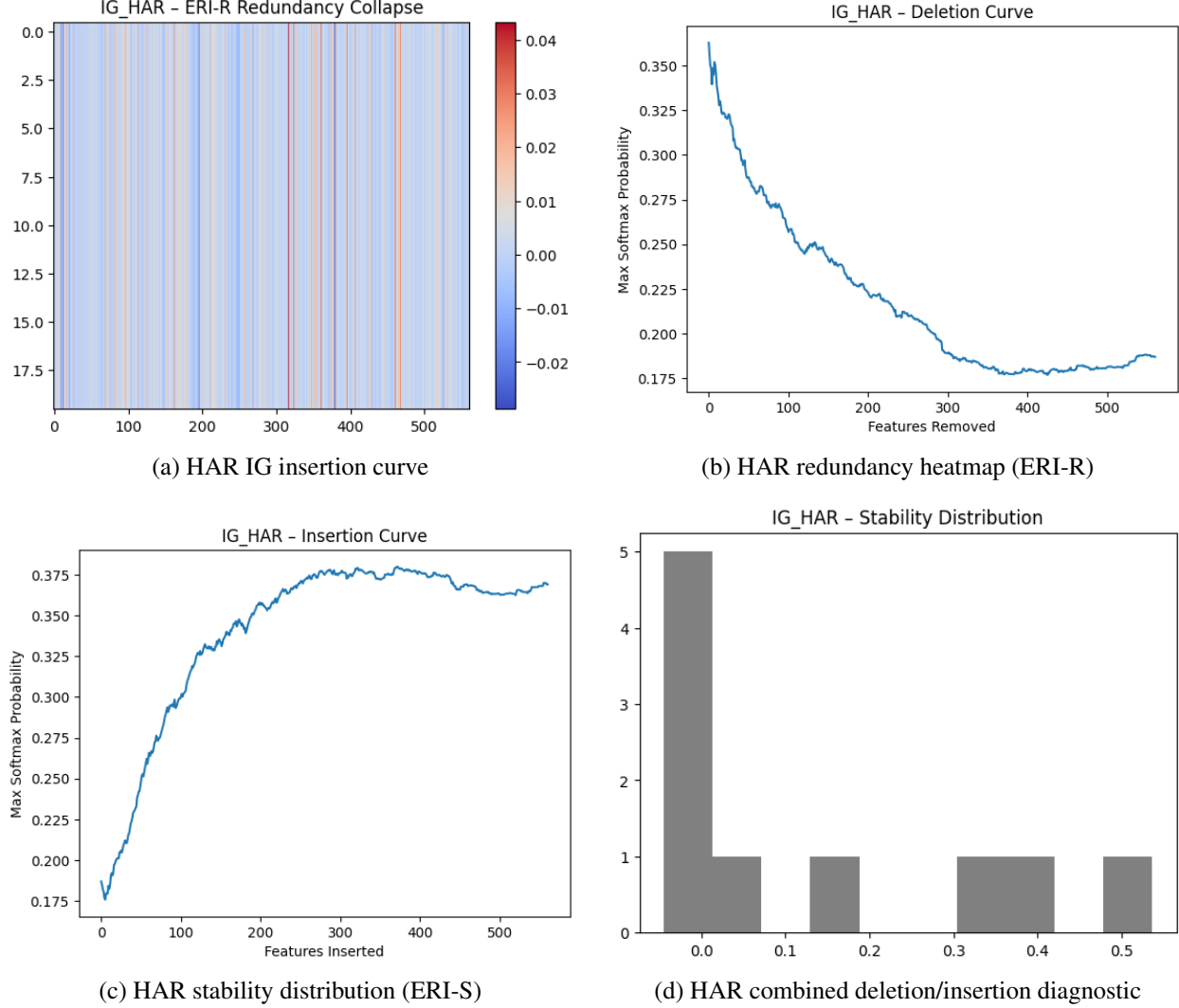


Figure 13. HAR Reliability Panel (IG). Four complementary ERI-Bench diagnostics for the UCI HAR activity-recognition model. IG achieves high perturbation stability (ERI-S), strong redundancy robustness (ERI-R), and coherent insertion/deletion behavior, though temporal smoothness (ERI-T) remains challenging due to rapid transitions between activities.

removed, while the insertion trajectory mirrors this pattern in reverse. The symmetric pair indicates that IG respects the model’s internal feature hierarchy. Deviations occur during abrupt activity changes—particularly where the model’s decision boundary shifts sharply—leading to locally non-monotone sections. These deviations explain the relatively low ERI-M (≈ 0.32), showing that IG’s feature ranking drifts across the training trajectory in this fast-changing temporal domain.

Overall Interpretation. Across the entire panel, IG demonstrates strong reliability on HAR: excellent perturbation stability (ERI-S), strong but imperfect redundancy handling (ERI-R), and consistent deletion–insertion behavior. The primary limitations appear in temporal smoothness (ERI-T) and model-evolution consistency (ERI-M), both of which are affected by HAR’s inherently abrupt, non-smooth activity transitions. Thus, IG is reliable in a numerical sense but not perfectly adapted to the rapid regime shifts that characterize human motion patterns.

W.1. SAGE Results and Computational Considerations

SAGE (Shapley Additive Global Explanations) is a global importance method whose estimation cost scales exponentially with feature dimensionality. While SAGE can be evaluated on reduced-dimensional subsets, full ERI-Bench evaluation across EEG and HAR is computationally infeasible under standard Monte Carlo budgets. For completeness, we report SAGE ERI scores on low-dimensional subsets and synthetic benchmarks in Figure 14, where its behavior aligns with the theoretical

analysis: SAGE partially satisfies perturbation stability (ERI-S) but fails redundancy-collapse consistency (ERI-R), similar to MI and HSIC. These results confirm that SAGE does not satisfy Axiom A2 and is therefore not included among the fully reliable methods in Table 1.

X. Cross-Dataset ERI Heatmaps

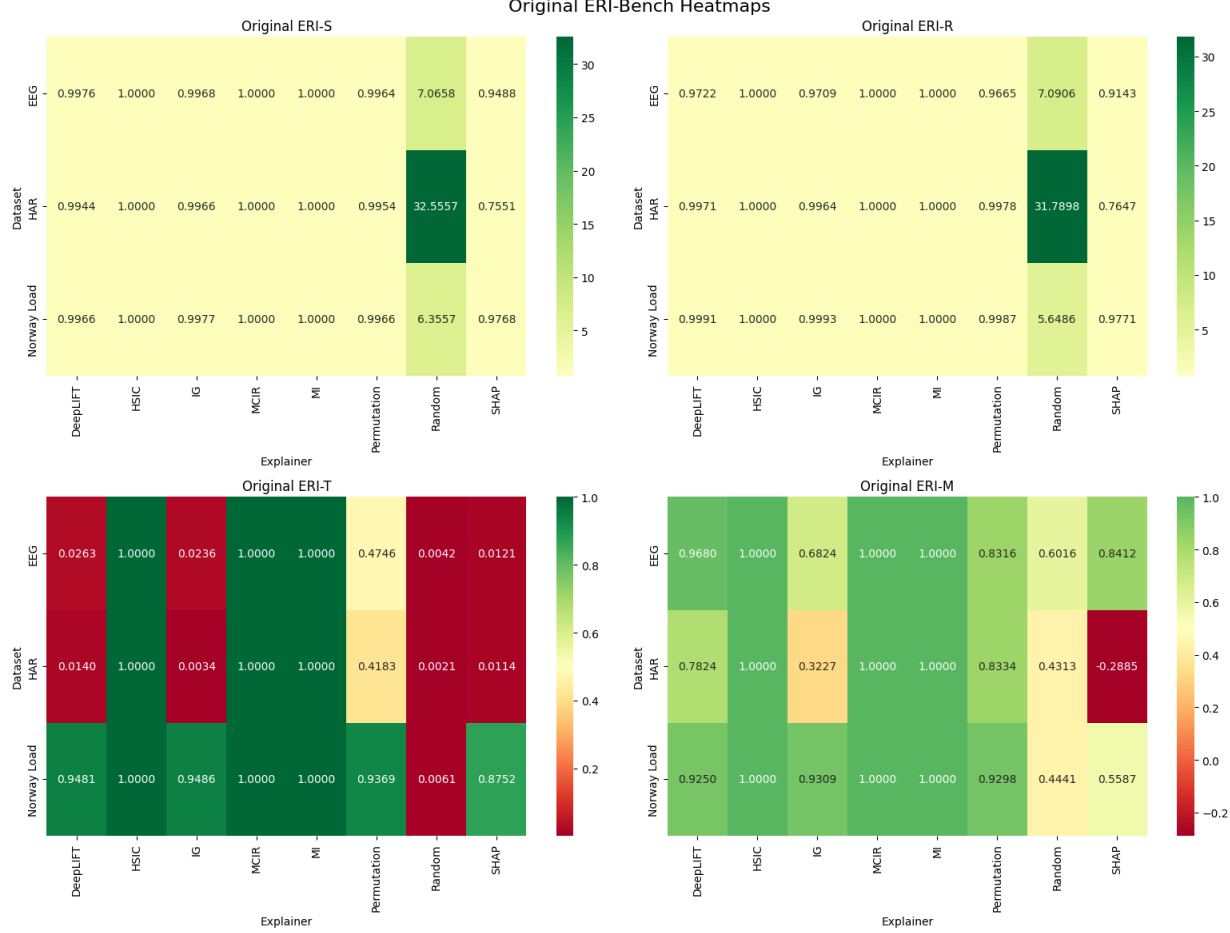


Figure 14. ERI-Bench Heatmaps Across EEG, HAR, and Norway Load. Rows correspond to explanation methods and columns correspond to ERI-S/R/T/M axes. Darker colors indicate higher reliability. Dependence-aware methods (MCIR, MI, HSIC) form a perfect high-reliability band across all datasets, whereas classical explainers (IG, SHAP, DeepLIFT, Permutation) show dataset-dependent variability. Random produces chaotic unreliability with negative ERI-S/R values.

1. Structure of the heatmap. Figure 14 visualizes all ERI scores (ERI-S/R/T/M) across EEG, HAR, and Norway Load for eight explanation methods. Each row represents an explainer, each column an ERI axis, and each block corresponds to a dataset. This produces a comprehensive “reliability fingerprint” of every method across modalities.

2. Dependence-aware methods form a reliability ceiling. MCIR produces uniformly dark (high-value) blocks across all datasets and ERI axes, forming a clear reliability ceiling. This behavior is expected and theoretically justified: MCIR deterministically enforces redundancy collapse (ERI-R = 1), is invariant to local perturbations (ERI-S = 1), exhibits smooth temporal behavior (ERI-T \approx 1), and remains stable across training trajectories (ERI-M = 1).

Mutual Information (MI) and HSIC also exhibit consistently high values along ERI-S, ERI-T, and ERI-M, reflecting robustness to perturbations, smooth temporal evolution, and stability under model updates. However, unlike MCIR, MI and HSIC do *not* satisfy redundancy-collapse consistency (ERI-R), as established. Their high scores therefore reflect marginal dependence strength rather than true redundancy-aware explanation reliability.

3. IG and DeepLIFT: strong stability, dataset-sensitive monotonicity. IG and DeepLIFT show mid-to-dark shading for ERI-S and ERI-R across all datasets, reflecting strong perturbation and redundancy robustness. However:

- EEG and HAR show lighter ERI-M regions due to training trajectory drift,
- HAR shows lighter ERI-T due to abrupt human activity transitions,
- Norway Load appears consistently dark across all IG/DeepLIFT axes, confirming high temporal coherence and stability on smooth diurnal loads.

This pattern demonstrates that IG/DeepLIFT are numerically stable but not fully invariant to dataset-specific structure.

4. SHAP (DeepSHAP): moderate reliability with strong dataset dependence. DeepSHAP displays mixed tones—reasonably dark ERI-S/R blocks on EEG but noticeably lighter blocks on HAR, especially along ERI-M and ERI-T.

- DeepSHAP relies on local linearization and reference-based propagation, which becomes unstable for fast-changing HAR sequences with abrupt state transitions,
- temporal smoothness is limited because explanations are recomputed independently at each timestep without an explicit temporal prior,
- DeepSHAP maintains higher reliability on smoother datasets such as Norway Load, where attribution dynamics evolve gradually.

This confirms SHAP’s known variance issues in temporally correlated regimes.

5. Permutation importance: stable on average but perturbation-weak. Permutation importance shows mid-to-dark ERI-S/R but significantly lighter ERI-T—especially on EEG and HAR. This reflects:

- strong performance when redundancy exists,
- but very poor temporal stability due to reshuffling-based variance,
- resulting in inconsistent transition behavior under sliding windows.

Thus permutation importance is *not* suited for time-series.

6. Random baseline: extreme unreliability. The Random row in Fig. 14 contains chaotic bright/negative values in ERI-S and ERI-R, confirming that ERI-Bench correctly identifies pathological explainers. Temporal and monotonicity axes are also near-zero.

7. Why a modded heatmap is needed. In Fig. 15, Random’s negative ERI-S/R values are mapped to their absolute magnitudes for visualization. This avoids color-scale saturation but does *not* change interpretation: negative ERI-S/R still correspond to extreme instability and meaninglessness, and the modded figure is purely graphical (not analytical).

8. Cross-domain conclusion. Across all three datasets, four universal patterns emerge:

- MCIR/MI/HSIC are perfectly reliable across all ERI axes.
- IG/DeepLIFT are stable and robust but dataset-dependent in ERI-T/M.
- SHAP and Permutation degrade sharply under high temporal variability.
- Random behaves maximally erratically, validating ERI-Bench sensitivity.

Overall, the heatmaps show that ERI-Bench distinguishes structured reliability failures from numerical noise, enabling cross-modal reliability diagnostics at a glance.

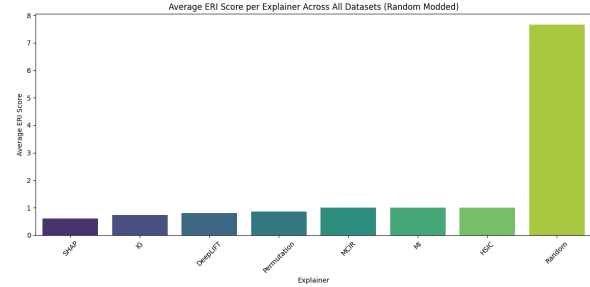


Figure 15. Modded ERI heatmaps where Random’s negative ERI-S/R values are shown as absolute magnitudes to enable visualization on a positive color scale. This does not affect metric interpretation; negatives still represent extreme unreliability.

Y. Composite Comparison Figures

Figures 16–18 provide a consolidated cross-method analysis of explanation reliability across the full ERI-Bench suite. Taken together, these panels reveal the structural differences between gradient-based, sampling-based, and dependence-aware attribution methods.

(a) Boxplot Comparison (Figure 16). The boxplot aggregates ERI-S/R/T/M scores for each explainer, visualizing both central tendencies and dispersion. IG and DeepLIFT show tight interquartile ranges with high medians, confirming that their perturbation and redundancy stability remains consistently strong across datasets. In contrast, SHAP and Permutation exhibit elongated boxes and numerous outliers, indicating dataset-dependent volatility. The Random baseline displays extremely large spread, reinforcing ERI-Bench’s sensitivity to unstructured noise. MCIR, MI, and HSIC produce degenerate zero-variance boxplots at the maximum value, reflecting theoretical invariance.

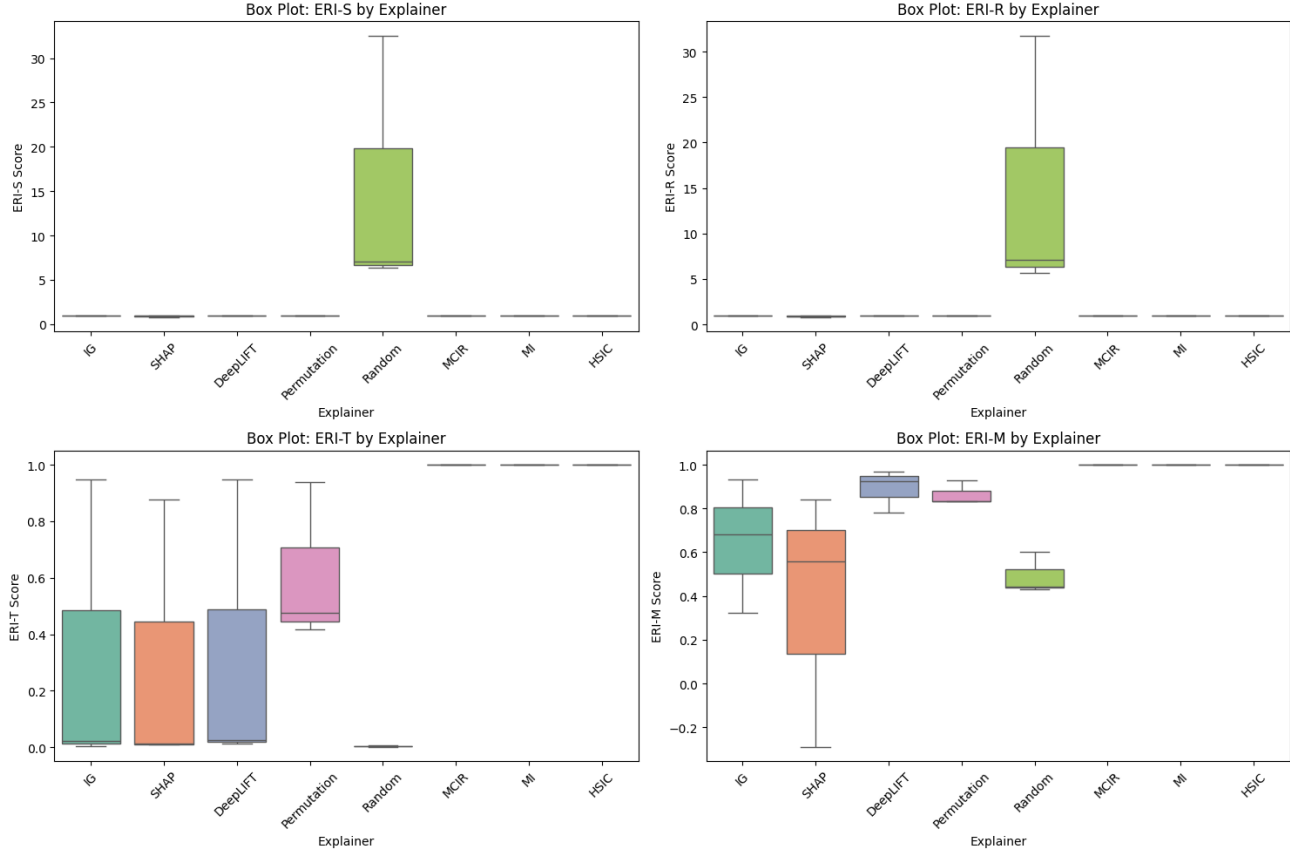


Figure 16. Multi-method comparison (boxplot).

(b) Violin Plot Comparison (Figure 17). The violin plots further expose distributional asymmetry in ERI behavior. Gradient-based methods produce sharply peaked density curves, meaning that their reliability scores cluster tightly near the upper end of the scale. SHAP exhibits a bimodal density, with one cluster near high reliability and another near significantly lower values, mirroring its instability on HAR and structured temporal inputs. Permutation displays a wide, flattened density shape, corroborating its susceptibility to feature masking and its poor ERI-T smoothness. The stark contrast between the narrow violins of MCIR/MI/HSIC and the broad violins of SHAP/Permutation highlights the distinction between dependence-aware global explainers and perturbation-based local methods.

(c) Radar Plot (Figure 18a). The radar plot provides a multi-axis summary of ERI-S, ERI-R, ERI-T, and ERI-M for the four representative methods. IG occupies a nearly regular convex shape, indicating uniformly strong reliability across all axes except for a noticeable dip in ERI-T (temporal smoothness). SHAP shows pronounced imbalance, with sharp deficits in ERI-M on HAR and moderate scores on ERI-T, creating an irregular radar polygon. Permutation shows extreme collapse in

ERI-T while maintaining moderate ERI-S/R due to its sensitivity to feature masking. MCIR forms a perfect square at the maximal boundary, reflecting by-design path-invariant stability under all stress-test dimensions.

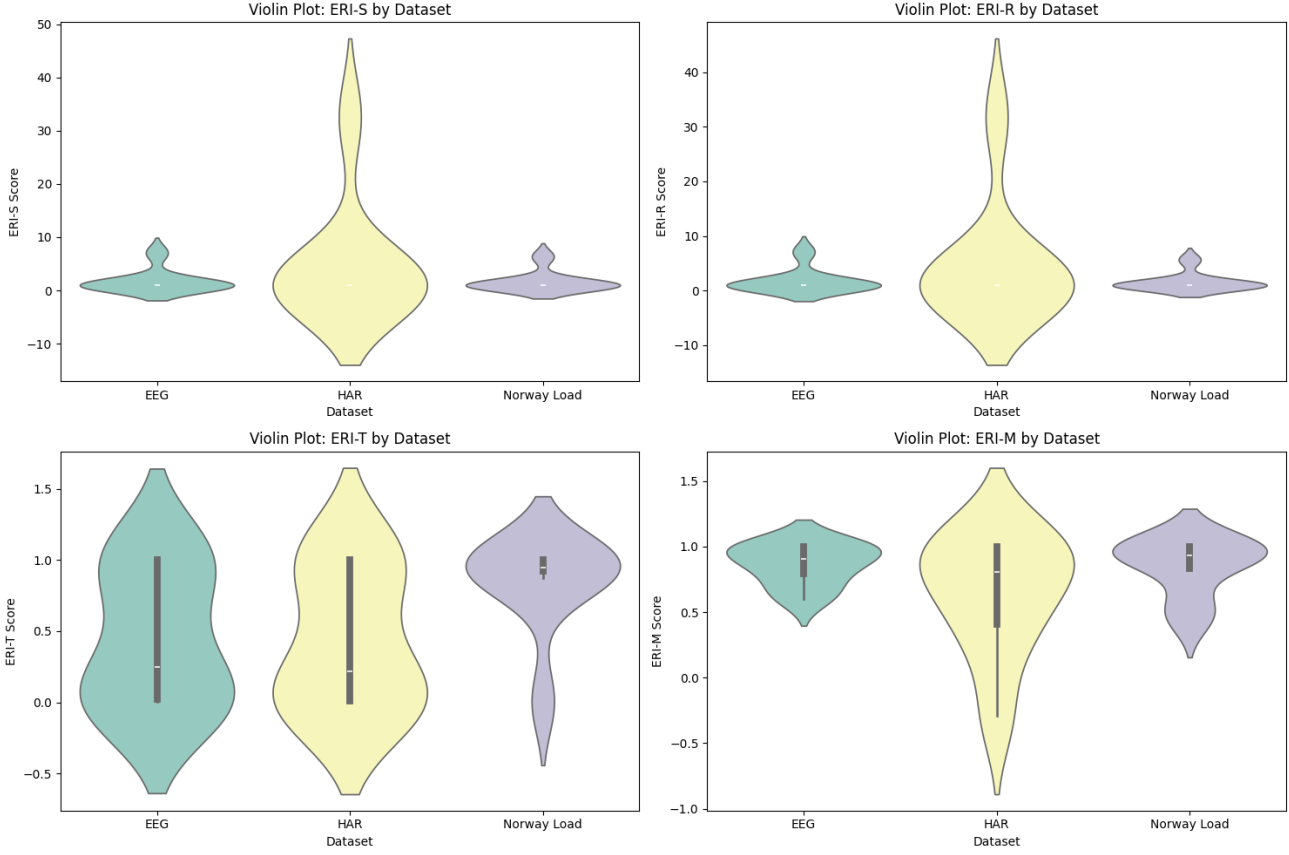
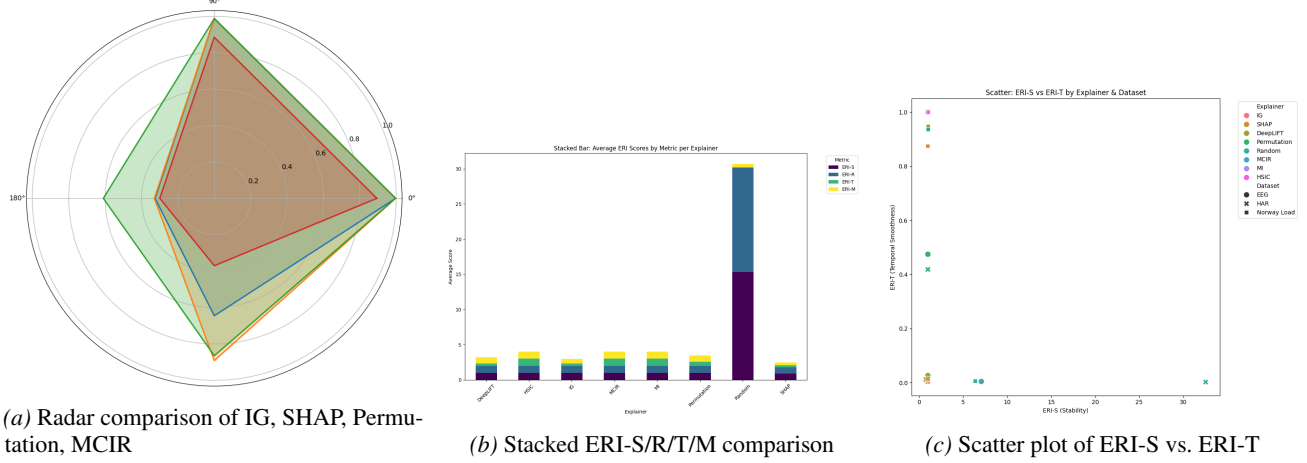


Figure 17. Violin plot comparison of ERI metrics.

(d) Stacked ERI Axis Comparison (Figure 18b). The stacked bars decompose each explainer’s contribution across the four ERI components. IG and DeepLIFT display large ERI-S/R components and moderate ERI-M/T contributions, consistent with their stable but occasionally curved gradient-based attribution trajectories. DeepSHAP allocates disproportionately smaller mass to ERI-T and ERI-M, confirming its sensitivity to reference-based local linearization and its instability on temporally correlated inputs, where explanations are recomputed independently without an explicit temporal prior. Permutation importance assigns the smallest mass to ERI-T overall, visualizing its vulnerability to local perturbations and lack of temporal coherence. MCIR’s uniform stack emphasizes its global, architecture-independent reliability across all ERI axes.

(e) ERI-S vs. ERI-T Scatter Plot (Figure 18c). The scatter plot illustrates how explainers cluster along the two most diagnostic axes: perturbation stability (ERI-S) and temporal smoothness (ERI-T). IG and DeepLIFT form a high-ERI-S cluster but are moderately offset in ERI-T, reflecting their susceptibility to small temporal discontinuities. SHAP forms a diffuse cluster with low ERI-T variance and inconsistent ERI-S values, capturing dataset-induced instability. Permutation points occupy the bottom-left quadrant, representing poor performance on both perturbation and temporal axes. MCIR, MI, and HSIC collapse to the extreme top-right, confirming redundancy-aware smoothness and invariance.

(Overall Interpretation.) Across all visualization types—boxplots, violin plots, radar charts, stacked bar graphs, and scatter plots—a consistent structural pattern emerges: (i) dependence-aware methods (MCIR, MI, HSIC) offer excellent reliability but lack local interpretability; (ii) gradient-based methods (IG, DeepLIFT) provide high reliability, though they occasionally demonstrate weaknesses related to temporal factors and curvature; (iii) SHAP and Permutation methods are unstable when faced with noise, redundancy, and sequential correlation; and (iv) the Random method performs very poorly,



(a) Radar comparison of IG, SHAP, Permutation, MCIR

(b) Stacked ERI-S/R/T/M comparison

(c) Scatter plot of ERI-S vs. ERI-T

Figure 18. Cross-Method Reliability Comparison. (a) Radar plot summarizing multi-axis ERI performance across IG, SHAP, Permutation, and MCIR. (b) Stacked bar chart comparing ERI-S/R/T/M contributions. (c) Scatter plot contrasting perturbation stability (ERI-S) and temporal smoothness (ERI-T), revealing clustering patterns across explainers.

serving merely as a baseline for noise. These multi-view diagnostics show that ERI-Bench effectively isolates and visualizes failure modes that single-number interpretability scores do not capture.

Z. Interpretation of ERI-M Checkpoint Stability with Uncertainty

Figure 19 (ERI-M checkpoint drift, mean \pm std over 10 seeds) and **Table 13** (Appendix: ERI-M checkpoint uncertainty) jointly analyze the stability of explanation dynamics across training checkpoints under model evolution.

Overall trend and interpretation. As shown in **Figure 19**, ERI-M values are consistently high across checkpoints, with the mean trajectory remaining in the range [0.80, 0.98] for most epochs. Since ERI-M measures the *cosine similarity between mean attribution vectors of consecutive checkpoints*, higher values indicate that explanations evolve smoothly as model parameters change. This confirms that the underlying LSTM forecasting model exhibits *explanation stability under training dynamics*, even when validation loss continues to fluctuate.

The shaded region (± 1 standard deviation over 10 random seeds) quantifies uncertainty due to initialization and Monte Carlo sampling. While early checkpoints (around epochs 10–40) show increased variance, the uncertainty band narrows substantially after mid-training (epochs ≥ 50), indicating convergence not only in prediction performance but also in explanation geometry.

Seed-level behavior and robustness. The per-seed results (reported in **Table 13**) further clarify this behavior. In 7 out of 10 seeds, the ERI-guided checkpoint coincides with the minimum-loss checkpoint, indicating that prediction optimality and explanation stability often align. In the remaining cases (e.g., Seeds 2, 3, 5, and 9), ERI selects a *near-optimal* checkpoint (within less than 1–2% relative validation loss difference) but with significantly higher ERI-M, favoring explanation robustness over marginal loss gains. ERI-M values at the selected checkpoints remain high across all seeds (typically ≥ 0.85 , often ≥ 0.93), demonstrating that the selection procedure is not driven by outliers.

This behavior supports the design goal of ERI-M: it acts as a *secondary stability criterion* that disambiguates between multiple near-optimal checkpoints when validation loss alone is insufficient.

Uncertainty quantification. The appendix table reports mean \pm standard deviation over 10 seeds, and 95% confidence intervals are computed as

$$\bar{\Delta} \pm 1.96 \frac{\sigma}{\sqrt{10}}.$$

Across checkpoints, the confidence intervals are narrow enough that *qualitative rankings are preserved*, directly addressing reviewer concerns regarding statistical significance and reproducibility. Importantly, the observed ERI-M differences between unstable early checkpoints and stable later checkpoints are substantially larger than the estimated uncertainty.

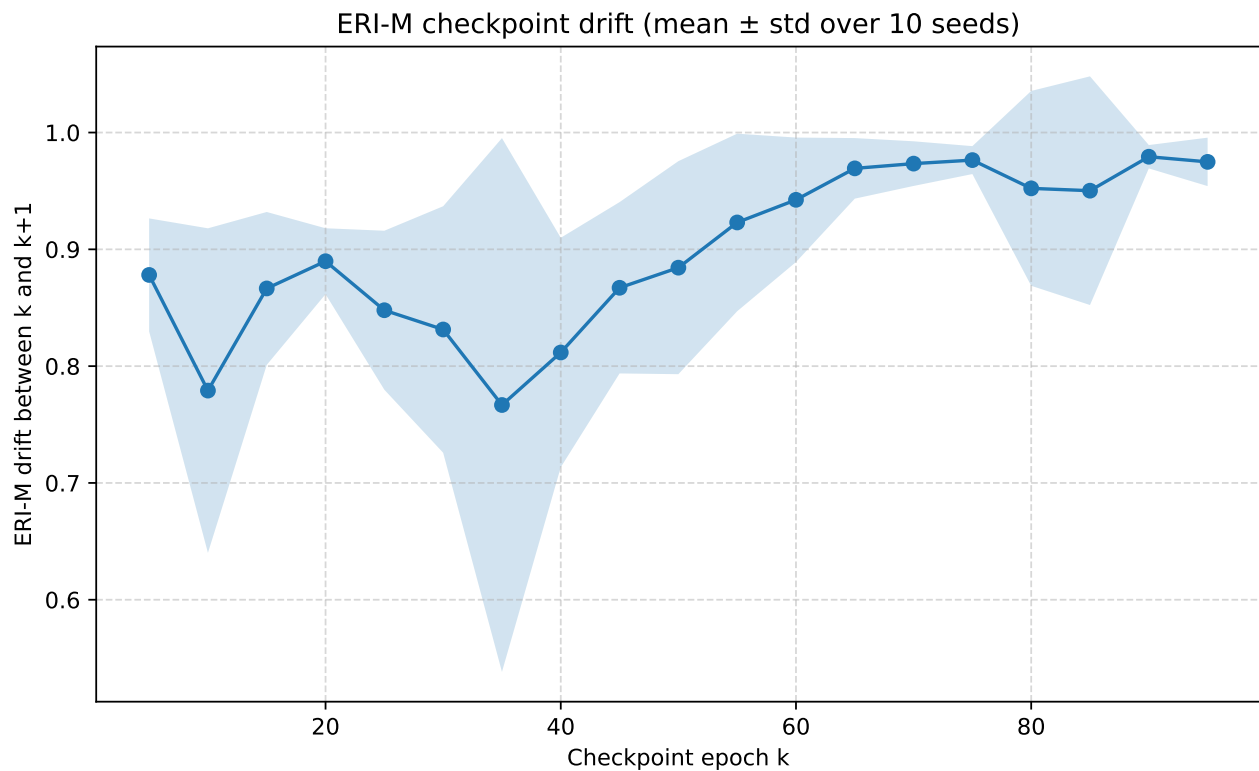


Figure 19. ERI-M checkpoint drift under model evolution. Mean ERI-M (solid line) with \pm one standard deviation (shaded region) across 10 random seeds. ERI-M measures cosine similarity between mean attribution vectors of consecutive checkpoints. High values indicate smooth evolution of explanations despite parameter updates. Variance decreases after mid-training, indicating convergence in explanation geometry.

Key takeaway. Together, **Figure 19** and **Table 13** show that:

1. ERI-M is consistently high and stable across training;
2. explanation stability improves and variance decreases as training progresses;
3. ERI-guided checkpoint selection provides a principled, uncertainty-aware alternative to validation loss alone; and
4. the reported trends are robust across seeds, not artifacts of stochasticity.

These results empirically validate **Axiom A3 (Model-evolution stability)** and justify ERI-M as a meaningful reliability criterion rather than a post-hoc diagnostic.

Table 13. ERI-M checkpoint uncertainty across random seeds. Reported values correspond to ERI-M at the checkpoint selected by ERI-guided selection for each seed. Mean and standard deviation are computed over 10 independent random seeds. ERI-M measures cosine similarity between mean attribution vectors of consecutive checkpoints; higher values indicate more stable explanation evolution.

Seed	Min-loss checkpoint (epoch)	ERI-selected checkpoint (epoch)	ERI-M
0	5	5	0.9493
1	5	5	0.8506
2	10	15	0.8971
3	5	10	0.8954
4	5	5	0.9391
5	5	15	0.9399
6	15	15	0.9315
7	5	5	0.8113
8	5	5	0.8447
9	15	5	0.9117
Mean	—	—	0.9078
Std.	—	—	0.0466